INAUGURAL - DISSERTATION

zur

Erlangung der Doktorwürde

der

Gesamtfakultät für Mathematik,

Ingenieur- und Naturwissenschaften

der

Ruprecht-Karls-Universität

Heidelberg

vorgelegt von

Felix Weißenfeld

geboren in Remscheid, Deutschland

Tag der mündlichen Prüfung: 26. April 2024

Modulation of Wetting and Mechanical Properties of Model Cell Membranes Caused by Changes on Molecular Levels

Gutachter: Prof. Dr. Motomu Tanaka

Prof. (apl.) Dr. Reiner Dahint

Modulation des Benetzungsverhaltens und mechanischen Eigenschaften von Modellzellmembranen durch Veränderungen auf molekularer Ebene

Benetzung ist ein allgegenwärtiges Phänomen, das nicht nur in der Natur und der Biologie vorkommt, sondern auch in Industrie und Medizin Anwendungen findet. In biologischen Systemen kann die Zelladhäsion im Rahmen der Benetzung komplexer, nicht Newtonscher Flüssigkeiten aufgefasst werden. In den letzten Jahrzehnten hat sich die physikalische Chemie der Benetzung und die physikalische Chemie biologischer Grenzflächen mit Hilfe neuer experimenteller und analytischer Instrumente weiterentwickelt.

Das Hauptziel dieser Arbeit ist die Untersuchung der Benetzung von Modellzellmembranen durch die Kombination verschiedener physikalisch-chemischer Techniken. In Kapitel 4 wird die Benetzung (Adhäsion) von bioinspirierten, Funktionspolymerbürsten mit einfachen Zellmodellen untersucht. Zunächst wurde die Änderung der Polymerbürstenkonformation mit Hilfe hochenergetischer Röntgenreflektivität gezeigt. Anschließend wurde die Form von Riesenvesikeln für die jeweiligen Polymer Konformationen durch konfokale Fluoreszenzmikroskopie beobachtet. Da die Form der Vesikel nicht durch die Oberflächenspannung bestimmt wird (wie bei einer Newtonschen Flüssigkeit), sondern durch die Elastizität der Membran in der Nähe der Oberfläche, wurde das Höhenprofil der Vesikel in der Nähe der Oberfläche, mittels Mikrointerferometrie analysiert. Dies ermöglicht die quantitative Berechnung der freien Adhäsionsenergie. Die Mikrointerferometrie befähigt dazu Höhenfluktuationen mit nm Genauigkeit zu bestimmen, wodurch das Grenzflächenpotential zwischen den Polymerbürsten und den Riesenvesikeln quantifiziert werden konnnte. Diese Experimente wurden in Kapitel 5 erweitert, indem die dynamischen Änderungen der Interaktion zwischen Vesikel und Polymerbürsten beobachtet wurde. Der Übergang vom nicht benetzten Zustand zur Benetzung und umgekehrt wurde in Echtzeit mit einer zeitlichen Auflösung von 30 ms beobachtet. Es ist bekannt, dass die mechanischen Eigenschaften von Membranen nicht nur durch Adhäsion, sondern auch durch Bindung von Proteinen an diese beeinflusst werden können. In Kapitel 6 wurde unter Verwendung der gleichen Zellmembranmodelle (Riesenvesikel) der Einfluss kleinster Veränderungen der molekularen Struktur der Protein-Membran Interaktion untersucht . Als biologisch relevantes Modell wurde die Modulation der Membranmechanik durch die Bindung von C-reaktivem Protein (CRP) an die Vesikel, die oxidierte Lipide enthalten, untersucht. Zunächst wurde die Rolle der durch elektrostatische Wechselwirkungen getriebenen Bindung von CRP an oxidierte Lipide durch Zeta Potential Messungen bestätigt. Danach wurde der Einfluss von CRP auf die mechanischen Eigenschaften der Membran untersucht und mittels Fourier Analyse der Membranfluktuationen berechnet, wobei oxidierte Lipide eine deutliche Änderung gegenüber nicht oxidierten Lipiden zeigten. Die erhaltenen Ergebnisse zeigen klar wie kleine Änderungen auf molekularer Ebene, wie z.B. die Kompak-

tierung von Polymerbürsten oder die Oxidation von Lipiden, Unterschiede hinsichtlich Benetzung und mechanischer Eigenschaften bewirken können.

Modulation of Wetting and Mechanical Properties of Model Cell Membranes Caused by Changes on Molecular Levels

Wetting is an ubiquitous phenomenon not only present in nature and biology but also of key importance in industry and medical applications. In biological systems, cell adhesion can also be understood within the framework of wetting of complex, non-Newtonian fluids. During the past several decades, physical chemistry of wetting and interfacial interactions of biological interfaces has been developed with aid of new experimental and analytical tools. The primary aim of this thesis is to study the wetting of model cell membranes by using the combination of various physicochemical techniques. In section 4 the wetting (adhesion) of bio-inspired, stimulus responsive polymer brushes with simple model cells, giant vesicles,were studied. First, the switching of polymer brush conformation was monitored by using high energy specular X-ray reflectivity. Then, the global shape of giant vesicles at relaxed and compacted states were monitored by confocal fluorescence microscopy. As the shape of vesicles is not determined by the surface tension (like the case of Newtonian fluid), the shape (height profile) of vesicle near the surface, dominated by the membrane elasticity, was analyzed by microinterferometry. This enables the quantitative calculation of the adhesion free energy of vesicles. Moreover, owing to the capability of the microinterferometry to determine the height fluctuation in nm accuracy, the interfacial potential between the polymer brush and the giant vesicle could be calculated quantitatively. This line of study was further extended in section 5, where the dynamic switching of the vesicle-brush interaction was monitored. The transition between from non-wetting (off) to wetting (on), and *vice versa*, was was monitored in real time by the combination of microfluidics and microinterferometry with the time resolution of 30 ms. It is well known that not only the adhesion but also the binding of proteins changes the mechanical properties of lipid membranes. In section 6, the influence of subtle changes in molecular structures on the protein-membrane interaction and hence the membrane mechanics was investigated using the same membrane model (giant vesicles). As a biologically relevant model, the modulation of the membrane mechanics by the binding of the acute phase inflammatory C-reactive protein (CRP) to the vesicles containing oxidized lipids was investigated. First, the potential role of electrostatic interaction was studied by measuring the zeta potential of lipid vesicles, suggesting that CRP binds to the vesicles containing lipids with a higher oxidative level. In the next step, the influence of CRP binding on the mechanical properties of the membranes was calculated from the Fourier analysis of the membrane fluctuation, indicating that the binding of CRP to highly oxidized lipids caused the most prominent change in the bending rigidity of the membrane. The

obtained results demonstrated how the subtle changes on the molecular level, such as the compaction of polymer brushes and the oxidation of lipids, significantly modulates the wetting and mechanical properties of lipid membranes.

The biggest enemy of quality is hurry.
Henry Ford

Contents

CONTENTS

Abbreviations

CONTENTS

1 Introduction

1.1 Biophysical chemistry of lipid membranes

Cell membranes define the boundary between the cytoplasm (inside) and extracellular space (outside) of biological cells. An increasing number of studies has shown that cell membranes act as a smart filter to exchange necessary and non-necessary molecules between the inside and outside as well as the reaction hubs for many biochemical reactions, such as signaling.[1] In figure 1.1 a schematic illustration of a cell membrane is shown. The outer surface of the cell membrane displays carbohydrate chains (glycocalyx), and the inner leaflet is coupled to the cytoskeleton. The core structure consists of a variety of lipids, such as glycerophospholipids, sphingolipids and cholesterols.[2] The cell membrane also contains various membrane-associated proteins, which can be classified as peripheral proteins and integral proteins. Lipid membranes and their associated proteins can be described as an quasi two-dimensional structure that allows self-assembly and lateral diffusion, which was described by Singer and Nicholson as the "fluid mosaic" model.[3]

extracellular space
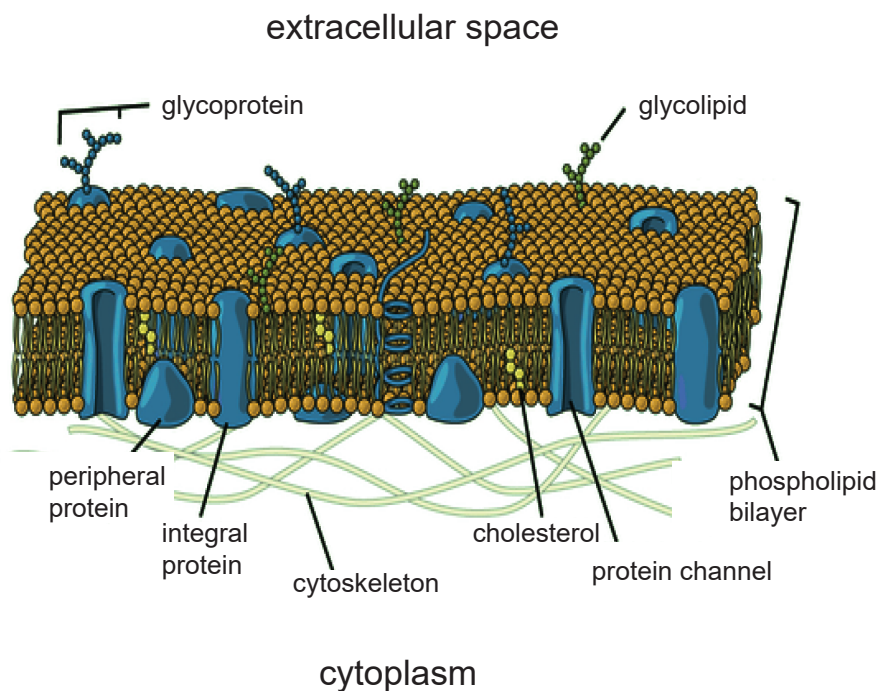
Figure 1.1. Structure of an eukaryotic cell membrane with its associated components (adapted from[2])

1.1.1 Thermodynamic principle of membrane formation

One of the major constituents of cell membranes are phospholipids, which are am-phiphilic molecules consisting of apolar (and hence hydrophobic) hydrocarbon chains and hydrophilic head groups (figure 1.2).
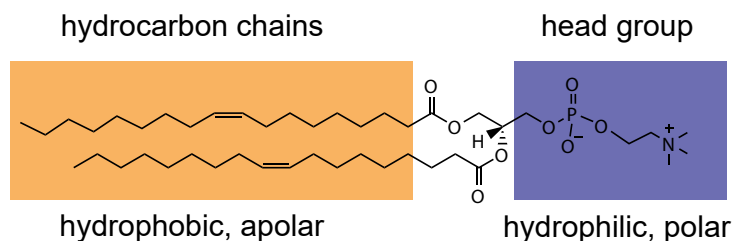
Figure 1.2. Molecular structure of a lipid showing its amphiphilic character.

Like other surfactant molecules, phospholipids in water can form a variety of super-structures including planar bilayers, vesicles and inverted micelles illustrated in figure 1.3.[4]
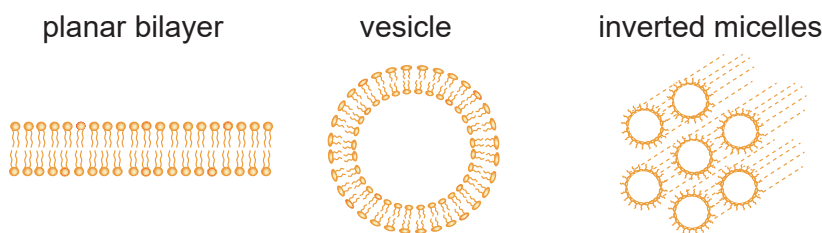
Figure 1.3. Superstructures of lipids in water.

When lipids and surfactants are dissolved in water, they adsorb to the water surface and reduce the surface tension of the air/water interface, given by a slight modification of the standard Gibbs equation (1.1).[5][6]

$$\frac{\mathsf{d}\gamma}{\mathsf{dlog}(c)} = -\frac{2.3RT}{AN_{\mathsf{A}}} \tag{1.1}$$

Here $\mathsf{d}\gamma$ denotes the change in surface tension [N m^{-1}], c the concentration [mol m^{-3}], A the area per molecule [m²], N_{A} = 6.022 × 10^{23} [mol^{-1}] the Avogadro constant, R = 8.314 [J mol^{-1}K^{-1}] is the ideal gas constant and T the temperature. Once the water surface is saturated with lipid/surfactant molecules, they start to form aggregates in order to gain free energy by reducing the contact of hydrophobic moieties to water, which is called as the hydrophobic effect.[7][8]

The critical concentration $c^\star$ at which the surfactants-lipids start to form aggregates is called as the critical aggregate concentration (cac), which is defined according to equation (1.2).[9]

$$c^* = c_0 \exp\left(-\frac{\Delta\mu}{k_B T}\right) \qquad (1.2)$$

Here, c_0 is the molar fraction in the lipid phase, $\Delta\mu$ is the difference in chemical potentials of lipids in the vicinity of other lipids (μ_{ref}) and lipids in water ($\mu_{\text{H}_2\text{O}}$), $\Delta\mu = \mu_{\text{ref}} - \mu_{\text{H}_2\text{O}}$ and K_B = 1.381 $\times$ 10^{-23} J K^{-1} is the Boltzmann constant. It is notable that the hydrophobic effect is not only the key thermodynamic principle of the aggregate formation by lipids and surfactants but also the principle governing various phenomena, including folding of proteins and incorporation of transmembrane proteins.[10] Whether lipids form inverted micelles, planar bilayers, or other superstructures depends on their molecular geometry. This can be predicted by the ratio of the molecular volume V and the product of the head group area A and the length of the molecule l, so called packing parameter p shown in equation (1.3).

$$p = \frac{V}{Al} \qquad (1.3)$$

If $p > 1$, inverted micelles are formed, which take tubular shapes forming hexagonal superstructures (H_{ll}). In this study, phospholipids with p $\approx$ 1 that tend to form bilayers were used.[4][11]

1.1.2 Thermotropic polymorphism

The molecular structure of lipid bilayers depends on the temperature, such as fluid (L_α) phase, ripple ($P_{\beta'}$) phase, and gel ($L_{\beta'}$) phase shown in figure 1.4. The nomenclature originates from the definition of liquid crystals. For example, L_α phase is analogous to smectic A phase of liquid crystals.[12] In this phase, the molecules take a long-range order but no short-range order. In case of phospholipid membranes, the long-range order coincides with the finite membrane thickness. In contrast, the hydrocarbon chains freely undergo a gausche rotation and therefore the chains are disordered.[13] L_β phase is analogous to smectic B phase, where the molecules also possess a short-range order.[14][15] The superscript ' means the tilt of the molecule with respect to the direction perpendicular to the local plane of the membrane (indicated by the broken line in Figure 1.4). In this study, the membranes in the fluid (L_α) phase were used.
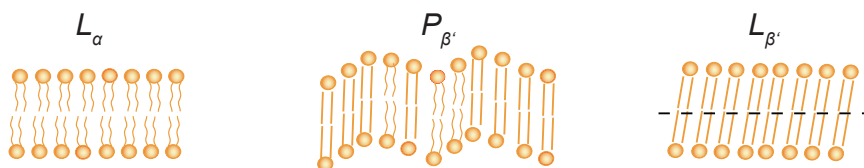
Figure 1.4. Thermotropic molecular structures of lipid bilayers. (L_α) phase (left), b) ripple ($P_{\beta'}$) phase (middle), c) gel ($L_{\beta'}$) phase (right).

1.1.3 Mechanical properties

Lipid membranes are also known for their unique mechanical properties described in detail in section 3.2, which make them distinct from classical Newtonian fluids (like liquid water).[9] Compared to liquid droplets where the shape is determined by the surface tensions, the shape of a lipid vesicle is dominated by the membrane elasticity. There are three principal parameters that define the elasticity of the membranes, the lateral expansion coefficient, shear modulus, and bending rigidity. If one assumes a lipid membrane as a quadratic object, three modes of elastic deformation can be considered. As schematically illustrated in Figure 1.5, the elastic deformation energy can be represented within the frame work of Hookian energy representation.[16] In figure 1.5 a) a schematic illustration of the lateral expansion of an quadratic membrane patch is shown, where the lateral expansion energy G_e is presented in equation (1.4)
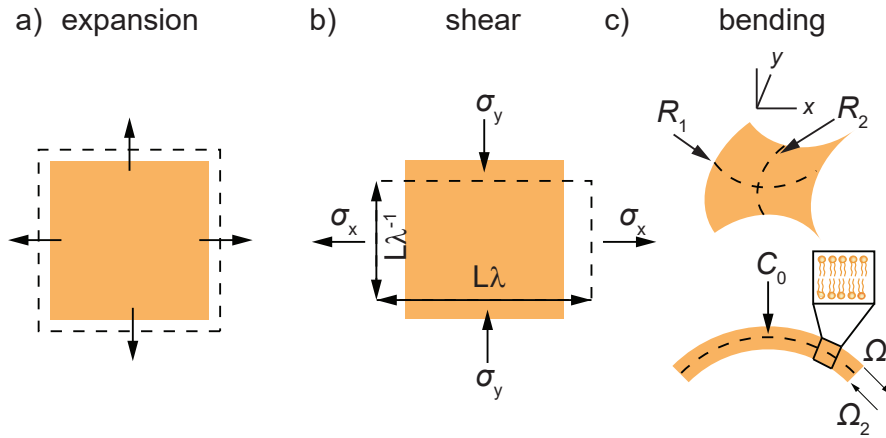
Figure 1.5. Elastic deformations of a quadratic membrane patch.

$$G_\text{e} \;=\; \frac{1}{2}\tau\left(\frac{dA}{A}\right)^2 \tag{1.4}$$

The area compressibility modulus is denoted by τ and the area of the patch by A. The lateral membrane tension σ can be obtained as $\sigma = \tau\frac{\partial A}{A}$. The elastic shear energy G_s is defined as the lateral stress, where the Area A of the patch stays constant (figure 1.5 b) presented in equation (1.5), where μ is the shear modulus.

$$G_\text{s} = \frac{1}{2}\mu\left(\lambda - \frac{1}{\lambda}\right)^2 \tag{1.5}$$

Assuming a lipid membrane patch with a thickness much lower than the membrane area, bending the patch yields two different curvature radii R_1 and R_2 in the x,y-plane as illustrated in figure 1.5 c) (upper panel). Thus, $C_m = \frac{1}{2}\left[(R_1^{-1}) + (R_2^{-1})\right]$ is the mean curvature. According to the Hookian energy representation the elastic energy

is proportional to the quadratic deformation yielding equation (1.6), where κ is the bending rigidity.

$$G_{\mathsf{b}} = \frac{1}{2}\kappa 2 C_m^2 \tag{1.6}$$

Assuming two tensions, acting on the upper respectively lower part of the membrane Ω_1 and Ω_2, where Ω_1 stretches the upper part of the membrane and Ω_2 compresses it, the patch bends resulting in a spontaneous curvature C_0 as presented in figure 1.5 c) (lower panel). The bending energy G_{b} can be expressed as shown in equation (1.7), indicating that the spontaneous curvature C_0 can reduce the elastic bending energy.[17]

$$G_{\mathsf{b}} = \frac{1}{2}\kappa (2C_m - C_0)^2 \tag{1.7}$$

Seifert and Lipowsky[18] extended the theory of Helfrich[17] to vesicles. Minimizing the free energy functional yielded the boundary condition for adhered vesicles presented in equation (1.8) (details see in section 3.4). Here, $C_{1\text{max}}$ is the principal curvature at the contact along the vesicle contour and $\Delta\gamma_{\mathsf{W}}$ is the adhesion free energy.

$$\Delta\gamma_{\mathsf{W}} = \frac{1}{2}\kappa C_{1\text{max}}^2 \tag{1.8}$$

Compared to a plastic foil with a similar thickness (5 nm), lipid membranes are known for the remarkably low shear modulus and bending rigidity. For example, the shear modulus μ and the bending rigidity κ of a red blood cell membrane is $\approx$ 5 orders and 2 orders of magnitude lower compared to those of a polyethylene film, respectively as presented in table 1.1.

Table 1.1. Elastic parameters of a red blood cell and a polyethylene sheet, where both materials have a thickness of around 5 nm.[9]

material	μ [mN m^{-1}]	κ [J]	τ [mN m^{-1}]
red blood cell	0.006	0.5–5 $\times$ 10^{-19}	1 $\times$ 10^3
polyethylene	300	2 $\times$ 10^{-17}	5 $\times$ 10^3

This makes it possible for the red blood cells to resist high shear stresses and prominent bending deformation while traveling through narrow capillary. In contrast, the expansion/compression modulus τ of a red blood cell membrane is comparable to that of plastic, which enables the cell to keep a finite area.[9] In this study, two types of model membranes were used. Cell-sized giant unilamellar vesicles (GUVs) were used as the simplest model of cells in contact to the extracellular polymers. Lipid membranes deposited on planar substrates, called supported membranes, were used for the grafting of bio-inspired polymer brushes at a well-defined surface density.

1.2 Modelling adhesion/wetting of switchable surfaces with lipid membranes

1.2.1 Cell adhesion as wetting of complex fluids

Cell adhesion, either to the extracellular matrix or to neighboring cells, is one of the key biological processes. Cell-matrix adhesion is important for the activation of mechano-sensory signaling pathways.[19][20] On the other hand, cell-cell adhesion is crucial for the formation of multicellular systems.[21] Although the "real" cell adhesions in biological systems are mediated via interplay of various ligand-receptor interactions, the adhesion of simple GUVs can reproduce the deformation caused by adhesion. As described by Bell et al., the adhesion of cells and vesicles can be described within the framework of wetting physics.[22] In fact, the adhered cell on the surface shares similar features as a liquid droplet on a substrate presented in figure 1.6.
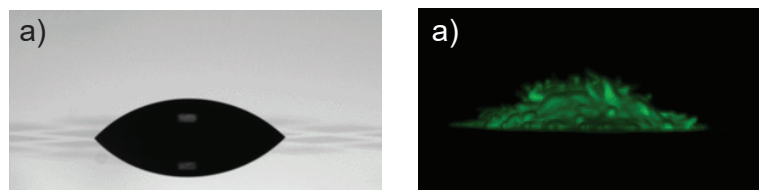
Figure 1.6. a) A liquid droplet (ethanol) on a solid surface (Si wafer). b) A mouse myoblast cell on a gelatin hydrogel substrate (adapted from[23])

To date, there have been a number of reports on the vesicle adhesion via receptor-ligand pairs[24,25,26] as well as on the vesicle adhesion via electrostatic interactions.[27] From the biophysical viewpoint, the most prominent difference between adhesion of complex fluids (including cells/vesicles) and wetting by droplets of classical Newtonian fluids (like water) is that the lipid membranes deform not only by tension but also by elastic deformation, which is characterized by the bending rigidity κ.[17] As a consequence the shape of an adhered vesicle is dominated by the balance between adhesion-induced tension and bending-force, which is in contrast to the shape of a liquid droplet that can be calculated from the balance of interfacial tensions by the Young's equation (see section 3.4).[28]

1.2.2 Models of dynamic switching of adhesion/wetting

In biological systems, cell biology can be highly dynamic. For example, the white blood cells in the blood stream are recruited to the surface of the endothelium, slow down the translational velocity by "rolling" on the surface until they establish a firm adhesion to the point of inflammation.[29] In artificial model sysytems, a number of stimulus responsive

polymers that can change the material properties have been designed in order to dynamically switch the adhesion of cells and vesicles. In response to the external stimuli such as temperature[30], pH-value[31], ionic strength[32] or light[33], the polymer brushes or gels change the surface free energy (hydrophilicity/hydrophobicity), surface charge density, Young's modulus, and polymer chain conformation.

In this study, the polymer brushes (pAA-Cys5-biotin) that can switch the conformation in the presence and absence of a small amount of Cd^{2+} ions were used to switch the adhesion/wetting by giant lipid vesicles. The molecular design of pAA-Cys5 was inspired by naturally occurring plant protein (phytochelatin), which selectively captures Cd^{2+} ions at a high affinity ($K_D \approx 10^{-9}$ M) even in physiological electrolytes containing [NaCl] = 100 mM, pH 7.4.[34] In section 4, the wetting of pAA-Cys5 brushes with giant lipid vesicles was studied. Inspired by the previous reports suggesting the compaction of pAA-Cys5 in the presence of Cd^{2+}[35], pAA-Cys5 brushes were used to switch the interfacial potentials. To precisely control the surface density of pAA-Cys5-biotin, supported membranes doped with biotinylated lipids were used for the coating of the glass substrates. With aid of neutravidin crosslinkers with a high affinity ($K_D \approx 10^{-15}$ M), the average distance between pAA-Cys5 on the surface $\langle d \rangle$ can be controlled by the molar ratio of the biotinylated lipids χ, $\langle d \rangle = (A/\chi_{biotin})^{0.5}$, where A_{lipid} is the area per lipid in the L_α phase[36][37] In the first step, the structural parameters of the brushes in the absence and presence of Cd^{2+} ions were investigated by high energy specular X-ray reflectivity (XRR). Next, the global shape of vesicles in contact with the brush surface was monitored by confocal fluorescence microscopy at the respective [Cd^{2+}] presented in figure 1.7a). As the shape of vesicles near the surface is determined by the membrane elasticity, microinterferometry was used to reconstruct the detailed height profiles shown in figure 1.7b). This enabled to calculate the adhesion free energy,$\Delta\gamma_W$ following the theoretical framework written by Bruinsma.[38]
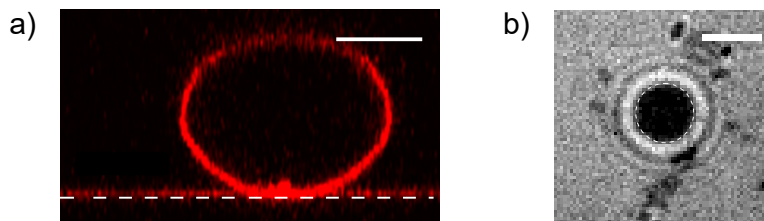
Figure 1.7. a) Confocal side view image (Scale bar is 5 µm) and b) microinterferometry image (Scale bar is 2 µm) of a vesicle.

Moreover, the interfacial potential $V(z)$ could be quantitatively estimated by monitoring membrane height fluctuations from adhered membrane patches. In section 5 the dynamic switching of the vesicle brush interaction was monitored with a time resolution of 30 ms by microinterferometry. With aid of an microfluidic chamber the concentration of

Cd^{2+} ions was modulated and the vesicle was monitored which enables to reconstruct the vesicle shape in the vicinity of the contact.

1.3 Modulation of membrane mechanics by lipid oxidation and protein binding

1.3.1 Oxidation of phospholipids and acute phase inflammation

In section 6, the influence of lipid oxidation on binding acute inflammatory proteins and the mechanical properties of giant lipid vesicles were investigated. Acute-phase inflammatory C-reactive protein (CRP) is a highly conserved protein that plays key roles in the acute phase immune response, named after its reaction with the capsular polysaccharid of Pneumococcus.[39,40] CRP forms a pentameric structure consisting of subunits with a molecular mass of $\approx$ 23 kDa resulting in a thickness of $\approx$ 3 nm and a diameter of $\approx$ 9 nm shown in figure 1.8a).[41] Thompson *et al.* found that the homopentameric CRP specifically binds to phospholipids, lipoproteins and polysaccharides containing phosphatidylcholine (PC) in the presence of Ca^{2+} presented in figure 1.8b). Remarkably, Chang *et al.* found that CRP binds to oxidized low density lipoprotein (LDL) and oxidized PC by utilizing a competitive immunoassay, but does not bind to native, non-oxidized LDL nor to non-oxidized PC.[42] This seems consistent with the report by Kushner and Kaplan, reporting that CRP is associated with the membrane of dying cells, but not with the membrane of healthy ones.[43]

a) b)
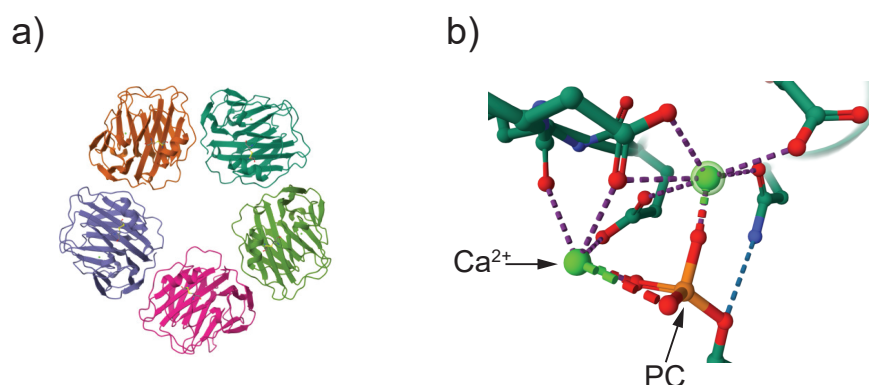
Figure 1.8. Ribbon diagram of CRP pentameric structure (a). Binding of PC moieties to CRP mediated by Calcium. The blue dotted line represents a hydrogen bond between the positively charged nitrogen of the PC moiety and glutamic acid from the CRP side chain; the violette dotted line shows the coordination between CRP side chains (dark green rods, red spheres representing the terminal amino acids) and Ca^{2+} ions (light green spheres). spheres).[41]

1.3.2   Effects of lipid oxidation on structures and mechanical properties of membranes

A previous XRR study showed a distinct thinning of lipid bilayers containing 20 mol% of oxidized lipids suggesting an increase in permeability and a decrease in bending rigidity. Corresponding quartz crystal microbalance with dissipation (QCM-D) data indicate that the bilayer formation occurs more favorable for oxidized lipids compared to non-oxidized ones, which also suggests a decrease in bending rigidity.[44] Grazing incidence X-ray fluorescence measurements exhibit a significant condensation of Ca^{2+} ions in the vicinity of a lipid monolayer containing 10 mol% carboxylated 1-palmitoyl-2-azelaoyl-sn-glycero-3- phosphatidylcholine (PazePC) compared to 1-palmitoyl-2-(9'-oxo-nonanoyl)-sn-glycero-3- phosphatidylcholine (PoxnoPC).[45] Since the binding of CRP is modulated via Ca^{2+} ions, studies were carried out regarding the influence of the degree of lipid oxidation on the interaction with CRP. Korytowski monitored the binding capacity of CRP to PC bilayers due to the vesicle size over time via dynamic light scattering (DLS) and the binding affinity with aid of isothermal titration calorimetry (ITC) measurements, resulting in the highest binding affinity to more oxidized PazePC.[46] In section 6.2, the effect of the degree of phospholipid oxidation on the CRP binding was monitored by zeta potential measurements, where the change in the surface potentials of lipid vesicles were monitored in the presence and absence of oxidized lipids (PoxnoPC and PazePC). Finally, the impact of lipid oxidation and protein binding on the mechanical properties of GUVs was quantitatively studied by Fourier analysis of the membrane fluctuation, called flicker spectroscopy[47][48][49] The shape fluctuation of the GUV was monitored over 15 s with a time resolution of 50 ms per frame using phase contrast imaging. To sharply define the position of contour below the pixel resolution, gradient images were used as shown in figure 3.3. The bending rigidity of the membrane could be calculated from the Fourier transform of the mean square amplitude of membrane fluctuation $\langle u(q)^2 \rangle$ (1.9). The experimental data could be fitted by the theoretical framework written by Gov and Safran[50], yielding the bending rigidity values, explained in detail in section 3.3.

$$\langle u(q)^2 \rangle = \left\langle \left| \frac{2}{N} \sum_{n=0}^{N-1} R_{rim}(n\Delta\Theta, t) e^{\frac{2\pi i \langle r \rangle q n}{N}} \right|^2 \right\rangle \tag{1.9}$$

The experimental data could be fitted by the theoretical framework written by Gov and Safran[50], yielding the bending rigidity values, explained in detail in section 3.3.
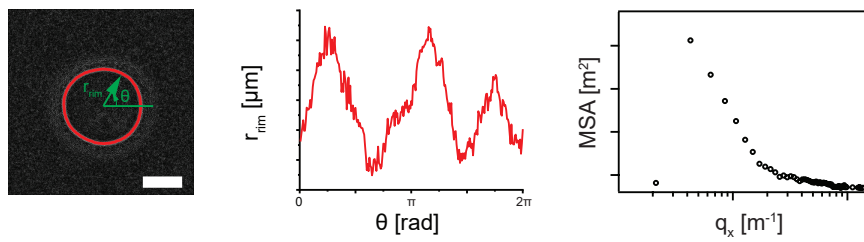
Figure 1.9. Flicker spectroscopy. Vesicle contour (red) obtained from radial intensity profile with azimuth angle Θ and the origin being the center of mass at each frame. The scale bar is 5 µm. (left). Obtained radius r_{rim} plotted versus Θ ($0 \leq \Theta \geq 2\pi$) (middle). Mean squared amplitude $\langle u(q)^2 \rangle$ plotted versus wave number q (right).

2 Materials and Methods

2.1 Materials

2.1.1 Substrates

In this study Si-wafers with native oxide (SiMat, Germany) and glass slides (Epredia, Germany) were used. Prior to the sample preparation the slides were cleaned by an adapted RCA cleaning procedure. The slides were cleaned in an ultra sonication bath first with aceton, followed by ethanol and water for 10 min each. The slides were sonicated in a mixture of Milli-Q water, hydrogen peroxide (30 %) and ammonium hydroxide (25 %) (5:1:1) for 3 min and then incubated at 60°C for one hour. Prior to further use the samples were dried at 60 °C.

2.1.2 Buffers

All buffers were prepared by using Milli-Q water from an ultra purification system (Merck Millipore, Germany) with a resistance < 18 MΩ. The buffers used during this study are listed below:

- Tris 10 mM pH=7.4
- Tris 10 mM NaCl 100 mM pH=7.4
- Tris 10 mM NaCl 100 mM Cd 1 mM pH=7.4
- Tris 10 mM pH=8.0
- Tris 10 mM Glucose 340 mM pH=7.4
- Tris 10 mM Glucose 340 mM Cd 0.25 mM pH=7.4
- Tris 10 mM Glucose 340 mM Cd 1 mM pH=7.4
- Tris 10 mM Ca 1 mM Glucose 310 mM pH=8.0

The glucose containing buffers were prepared by adjusting the osmolality after each preparation step following the procedure described in section 2.2.6.

2.1.3 Proteins

Neutravidin protein (Thermo Fisher Scientific, Germany) was diluted according to the manufacturer to a concentration of 1 mg/ml. Prior to use it was ultracentrifuged for 1 h at $\approx$ 100,000 g and afterwards diluted to the working concentration of 40 µg/ml. C-reactive protein was purchased from Merck (Germany).

2.1.4 Lipids

All lipids were purchased from Avanti polar lipids (USA):

- 1,2-dioleoyl-sn-glycero-3-phosphocholine (**DOPC**)

- 1-palmitoyl-2-oleoyl-glycero-3-phosphocholine (**POPC**)

- 1-palmitoyl-2-(9'-oxo-nonanoyl)-sn-glycero-3-phosphocholine (**PoxnoPC**)

- 1-palmitoyl-2-azelaoyl-sn-glycero-3-phosphocholine (**PazePC**)

- 1-palmitoyl-2-oleoyl-sn-glycero-3-phospho-L-serine (sodium salt) (**POPS**)

- 1-palmitoyl-2-oleoyl-sn-glycero-3-phosphoethanolamine (**POPE**)

- 1,2-Dihexadecanoyl-sn-Glycerin-3-Phosphoethanolamine,

Triethylammonium salt (**DHPE-TR**)
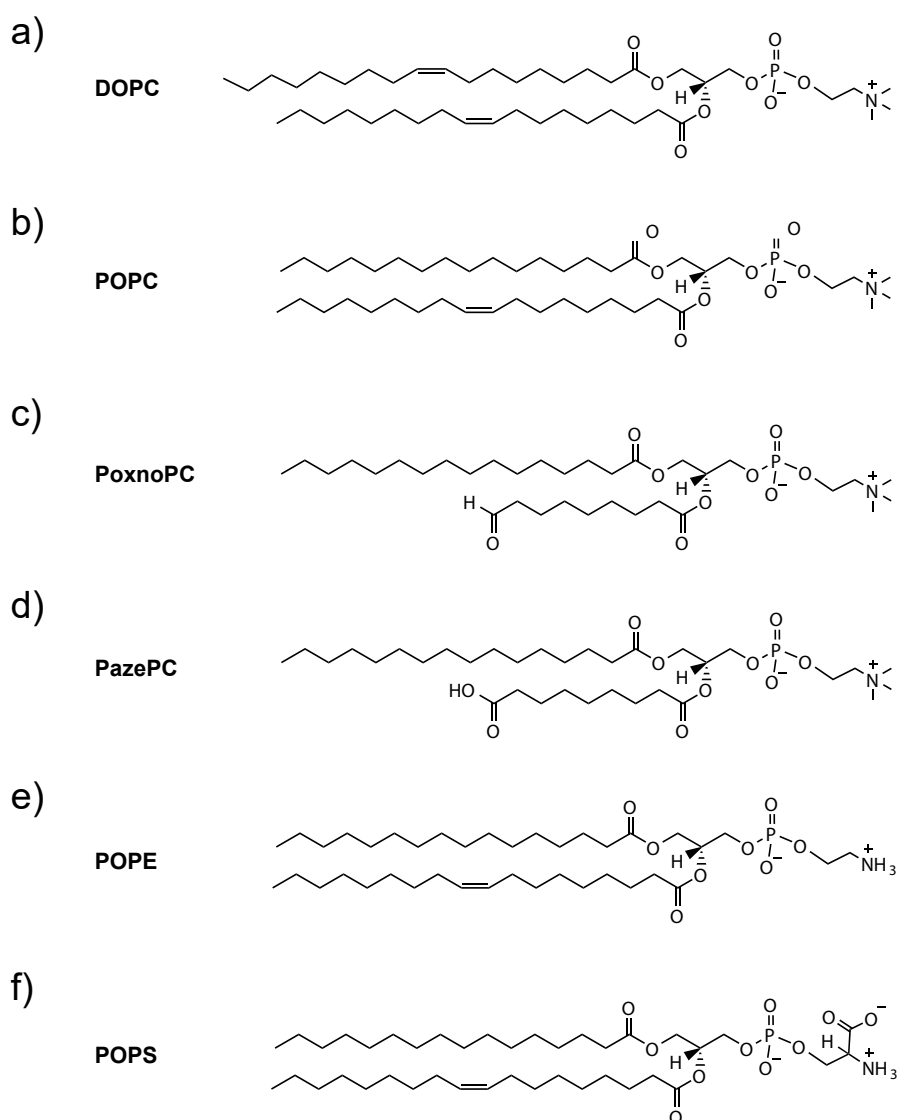
Figure 2.1. Molecular structure of lipids used in this study.

2.1.5 Cys5 Polymer

The pAA-Cys5 polymer was synthesized by Dr. Masaki Nakahata (Department of Materials Engineering Science, Osaka University). In brief, S-trityl-cysteine acrylamide (S-Tri-Cys-AAm) and acrylic acid (AA) were co-polymerized using 4,4'-((E)-diazene-1,2-diyl) bis(4-cyano-N-(2-(5-((3aR,4R,6aS)-2-oxohexahydro-1H-thieno[3,4-d] imidazol-4-yl) pentanamido)ethyl)pentanamide (ACVA-biotin) as an initiator, 2-(dodecylthio carbonothioylthio) -2-methylpropionic acid (DDMAT) as an chain transfer agent and trifluoroacetic acid (TFA) to deprotect the trityl group.

Therefore 0.05 mmol S-Tri-Cys-AAm and 0.95 mmol AA, 0.01 mmol ACVA-biotin and 0.01 mmol DDMAT were dissolved in 1 ml dimethylsulfoxide (DMSO) and dried with molecular sieves 4A. The solution was purged with nitrogen gas for 1h. Then the mixture was sealed and heated in an oil bath at 70 °C overnight. Under stirring the solution was poured into 10 ml acetone. The precipitate was collected via centrifugation (3500 rpm, 5 min). The supernatant was decanted, 1 ml TFA was added and it was stirred over night. The solution was added to 10 ml diethyl ether and the resulting precipitate was washed 3 times with 10 ml diethyl ether and got dried in vaccum over night at room temperature. The quality was ensured via ^{1}H NMR spectroscopy and gel permeation chromatography (GPC) resulting in a molecular weight M_W of 74 kDa and a poly dispersity index PDI = 2.5.[51] [35]

2.2 Methods

2.2.1 Preparation of pAA-Cys5 polymer coated substrates

Lipid solutions containing 98 mol% 1,2-dioleoyl-sn-glycero-3-phosphocholine (DOPC), 2 mol% 1,2-dioleoyl-sn-glycero-3-phosphoethanolamine-N-(cap biotinyl) (DOPE-biotin) dissolved in chloroform (1 mg/ml) were dried and after that stored under vacuum over night. The dried lipids were suspended in a 10 mM Tris(hydroxymethyl)aminomethan (Tris) buffer containing 100 mM NaCl adjusted to a pH of 7.4. The small unilamellar vesicles (SUVs) were prepared by sonicating the lipid suspension with a Misonix sonicator 3000 (Misonix, Germany) for 30 min. Thereafter, a RCA cleaned substrate was incubated with the vesicle suspension (0.5 mg/ml) at 40 °C for 30 min yielding a supported liplid bilayer. The unbound SUVs were removed by rinsing. Next, pAA-Cys5-biotin polymer brushes were grafted onto the bilayer, where neutravidin was used as a crosslinker as the dissociation constant between neutravidin and biotin is $K_D \sim 10^{-15}$ M.[52] The sample was incubated for 4 h at room temperature. The advantage of using supported membranes is the capability to generate surfaces with a defined grafting distance. In the case of 2 mol% biotinylated lipids the average distance $\langle d \rangle$ between to biotinylated lipds is defined as $\langle d \rangle = (A/\chi_{biotin})^{0.5}$. For χ_{biotin} = 2 mol% and an area per lipid of 60 $Å^2$ this results in an average grafting distance of 5.5 nm. In a next step pAA-Cys5-biotin (40 μg/ml) is coupled to neutravidin via incubation of 1 h at 40 °C.

2.2.2 Preparation of giant unilamellar vesicles

Giant lipid vesicles were prepared via electroswelling, which is a method established by Angelova and Mathivet.[53][54] Indium tin oxide glass slides (25 x 25 mm) were spin coated (300 rpm) with lipids diluted in chloroform (2.5 mg/ml) and dried under vacuum over night. The dried slides get hydrated in 300 mM sucrose solution for 2 h at 40 °C under an alternating current with an peak to peak amplitude of 3 V and a frequency of 10 Hz. To enable microscopy a portion of 0.2 ml of GUVs in sucrose are mixed with 1 ml of a buffered glucose solution to control osmolality and buoyancy.[24] The osmolality of the inner and outer solution was adjusted according to the procedure described in section 2.2.6.

2.2.3 Fluorescence microscopy

Fluorescence imaging was performed on an Axio Observer Z1 microscope (Zeiss, Germany) with a 63x oil immersion objective (NA 1.25). The exposure time for imaging was set to 1000 ms. The imaging was employed by using custom made μ-Slides VI 0.4 (Ibidi, Germany) without the bottom cover. Prior to imaging a RCA cleaned glass

slide (75 mm $\times$ 25 mm) was glued onto the slide as a bottom with polydimethylsilox-ane (PDMS).

2.2.4 Confocal fluoresence microscopy

Confocal imaging was done at the Nikon imaging center at the university of Heidel-berg with a Nikon A1R confocal microscope (Nikon Europe, Düsseldorf, Germany) via using an 60x oil immersion objective with a numerical aperture of 1.40. For fluores-cence imaging of giant unilamellar vesicles (GUVs) (preparation see in section 2.2.2), GUVs were labeled by incorporating 0.2 mol% DHPE-Texas-Red ($\lambda_{\text{excitation}}$ = 596 nm, $\lambda_{\text{emission}}$ = 615 nm). Confocal side view images were obtained due to the 3D recon-struction of the confocal bottom view images. The step size in z-direction was chosen to be 0.5 µm and the reconstruction was realized via using the reslice command in the ImageJ software. Due to different refractive indices of the immersion oil and the sample medium the vesicles appear elongated in z-direction. To correct this mismatch the con-focal microscope has been calibrated with objects where one can assume spherical shape. Within this work fluorescently labeled latex particles with a radius of r = 7.5 µm were used (see appendix 8.10). The imaging was performed by using custom made µ-Slides VI 0.4 (Ibidi, Germany) without the bottom cover. Prior to imaging a RCA cleaned glass slide (75 mm $\times$ 25 mm) was glued onto the slide as a bottom.

2.2.5 Reflection interference contrast microscopy

The interaction between GUVs and substrates was monitored via reflection interfer-ence contrast microscoy (RICM). Imaging was performed on an Axio Observer Z1 microscope (Zeiss, Germany) with a 63x oil immersion objective (NA 1.25) with a built in $\lambda/4$-plate. The illumination numerical aperture (INA) was set to 0.48. All images were collected by an Orca-Flash4.0LT camera (Hamatsu Photonics, Germany) with a time resolution of 30 ms.

2.2.6 Osmolality measurements

Adjusting the osmolality of the inner and outer medium of GUVs is crucial for their sta-bility. Thus, osmolality was monitored and adjusted using a micro-osmometer (OM 806, Löser, Germany). The sample volume was 100 µL as specified by the manufacturer.

2.2.7 X-ray reflectivity measurements

X-ray reflectivity (XRR) data were monitored using a D8 Advance diffractometer (Bruker, Germany) operating with a sealed X-ray tube emitting Mo K$_\alpha$ radiation (17.48 keV,

λ = 0.0709 nm). The slit was adjusted so that the vertical beam size h was 0.2 mm in the scattering plane. The attenuator was set to automatic to avoid radiation damage on the sample. A silicon strip detector (LynxEye Bruker AXS, Karlsruhe, Germany) was used. The reflectivity profiles were normalized by the instrument based normalization to the intensity of the incident beam.
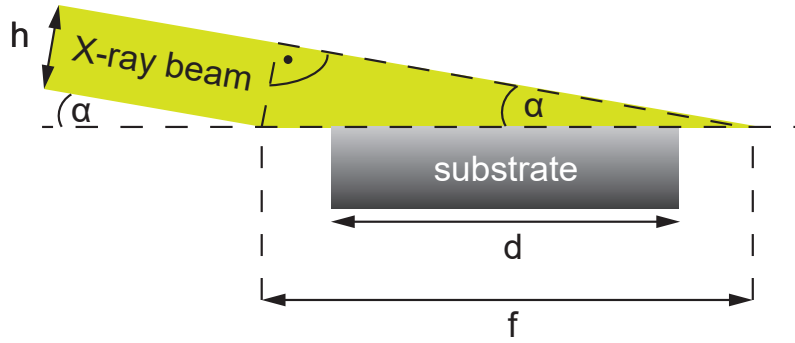
Figure 2.2. Beam foot print correction.

The beam footprint f was estimated according to geometrical considerations according to the schematic illustration of an X-ray beam impinging a substrate presented in figure 2.2 as $f = \frac{h}{\sin\alpha}$. In case of the substrate width d being smaller than the footprint f a footprint correction factor F shown in equation (2.1) is multiplied with the measured intensity and normalized to the intensity at the critical angle α_c (see section 3.7).

$$F = \frac{f}{d} \tag{2.1}$$

2.2.8 Flicker spectroscopy

To obtain mechanical properties of a membrane flicker spectroscopy was carried out. In brief, GUVs were prepared by the electroswelling method (see section 2.2.2). After the electroswelling in Sucrose (300 mM) the vesicle suspension was mixed with a buffered glucose solution containing Ca^{2+} (10 mM Tris 310 mM glucose 1 mM $CaCl_2$ adjusted to a pH of 8.0) to enable the vesicles to sediment. Each step of buffer preparation was verified by measuring the osmolality (see 2.2.6). 300 consecutive phase contrast images were monitored with a time resolution of 50 ms per frame with an 100 x oil immersion objective (NA = 1.4) and an ORCA-Flash4.0 LT camera (Hammatsu Photonoics, Herrsching, Germany). The image analysis was performed with a combination of the ImageJ (NIH, Bethesda, MD, USA) plugin "Image Differentials" written by Philippe Thévanaz[55] and an Igor Pro (WaveMetrix, OR, USA) routine kindly provided by Dr. Akihisha Yamamoto. First the phase contrast image was processed by the "Image Differentials" plugin resulting in a sharp peak between GUVs and its halo. The peak position can be detected as the rim by the Igor pro routine (see section 3.3).

2.2.9 Zetapotential measurements

Zeta potential measurements were carried out with an Malvern Zetasizer Nano ZS (Malvern Instruments Ltd., UK) by using folded capillary zeta cells (DTS 1070, Malvern Instruments Ltd., UK). Prior to each measurement the temperature was equilibrated to 20 °C. Each sample was measured 5 times (3 scans, 20-100 runs each). Values for the parameters for the measurement were taken from the database implemented in the manufacturers database. The zeta potential was calculated using the Malvern Zetasizer software applying the Smoluchowski equation (see section 3.9). The results were only used if the software classified the quality criteria as good.

2.2.10 y-shaped microfluidics

A custom made μ-slide ||| 3 in 1 (Ibidi, Germany) without the bottom coverslip was glued onto a RCA cleaned glass slide. The middle channel was not used and therefore closed with PDMS. The outer channels were connected to two syringe pumps, where the velocity was varied between 30 μl/min and 80 μl/min. The shear stress τ in the channel was calculated according to the manufacturer via equation (2.2).

$$\tau = \eta \Gamma \Phi \qquad (2.2)$$

The viscosity is given as η = 0.0072 dyn s/cm², the shear rate Γ = 227.4 s^{-1} yielding shear stresses of τ = 0.05 and 0.13 Pa for the respective flow rates of 30 μl/min and 80 μl/min.

3 Theoretical background

In this thesis lipid membranes play a key role, as they are used in form of giant unilamellar vesicles (GUVs) and supported lipid bilayer membranes in sections 4,5 and 6. Thus, GUVs and membrane mechanics are described in sections 3.1 respectively 3.2. The membrane mechanics can be characterized by flicker spectroscopy introduced in section 3.3, while the phenomenon of wetting is shown in section 3.4. In section 3.5 the conformations of polymer chains are described, while in section 3.6 the image formation in confocal microscopy is presented. In section 3.7 the basic principle of X-ray reflectivity (XRR) is shown, while in sections 3.8 and 3.9 the Debye screening length and the zeta potential are introduced. In section 3.10 reflection interference contrast microscoy (RICM) is introduced.

3.1 Formation of giant unilamellar vesicles

Giant unilamellar vesicles (GUVs) were first reported by Reeves and Dowben[56] who prepared phosphatidylcholin vesicles via hydrating lipids on a glass surface. After that several studies on the formation of GUVs and the usage as cell models were conducted. In these studies GUVs were perpared via the electroswelling method introduced by Angelova *et al.*[53] Experimental details on this technique are described in section 2.2.2. During the process of electroformation a vesicle being attached to a solid surface as schematically shown in figure 3.1a), increases in size due to osmotic and electrostatic forces, while the membrane tension σ leads to a decrease in size.
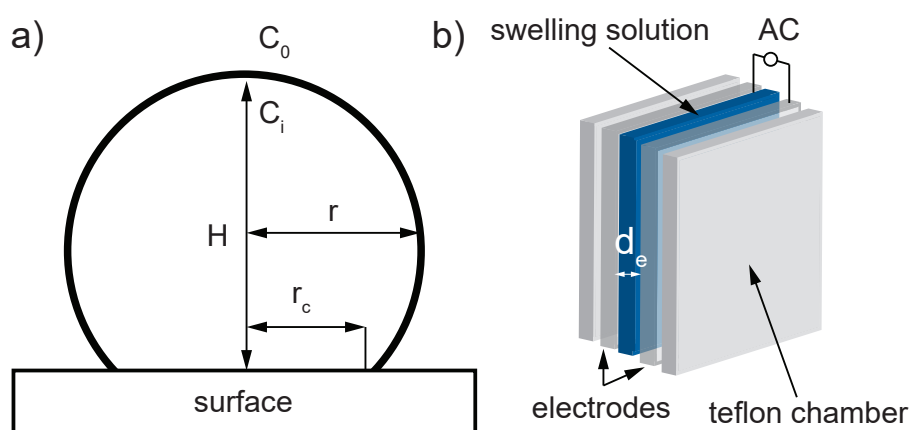
Figure 3.1. Electroformation of GUVs. a) a vesicle being attached onto a conductive surface during electroformation process, with r the radius and C_i and C_0 denoting the concentrations of the swelling media in the inside and the outside of the vesicle (adapted from[53]). b) Schematic illustration of electroformation chamber, with d_e the distance between the electrode surfaces.

The rate over which the vesicle changes its size over time is given in equation (3.1).

$$\frac{dr}{dt} = L\Delta p \tag{3.1}$$

L is the hydraulic permeability coefficient and p the driving pressure with $\Delta p = RT_k(C_i - C_0) + \frac{U\Sigma}{d_e} - \frac{2\sigma}{r}$, T_k is the absolute temperature, C_i and C_0 are the concentrations inside and outside of the vesicle, respectively (see figure 3.1a) and Σ is the surface charge density. The applied voltage is denoted by U and d_e is the distance between the surfaces of the two electrodes indicated in the illustration of a swelling chamber shown in figure 3.1b).[53]

3.2 Lipid membrane mechanics

Lipid membranes can be described as soft shells. Assuming a membrane patch the change of the area $A = u_x u_y$ according to lateral expansion in x and y direction in the membrane plane can be described via equation (3.2).[9]

$$\frac{\delta A}{A} \approx \frac{1}{2}\left[\left(\frac{\partial u}{\partial x}\right)^2 + \left(\frac{\partial u}{\partial y}\right)^2\right] \tag{3.2}$$

The expansion-elastic energy G_e can be written as shown in equation (3.3)

$$G_e = \frac{1}{2}\tau\left(\frac{\partial A}{A}\right)^2 \tag{3.3}$$

The area compressibility modulus is denoted by τ. Assuming the curvature of a membrane sheet to be determined due to two main curvatures R_1 and R_2, the energy density is proportional to the square of the mean curvature $C_m = \frac{1}{2}[(R_1^{-1}) + (R_2^{-1})]$.[17] Due to the asymmetry of biological membranes there is a spontaneous curvature C_0 that needs to be considered. Thus, the elastic energy of the whole curve per unit area G_b can be obtained via the surface integral presented in equation (3.4).[9]

$$G_b = \frac{1}{2}\kappa \int \left(R_1^{-1} + R_2^{-1} - C_0\right)^2 dS \tag{3.4}$$

While observing cells or vesicles under the microscope it is a well known effect that lipid membranes undergo a dynamic surface roughness, called flickering.[57] The flickering of red blood cells is very prominent. One reason for this might be that the adhesion of red blood cells on tissue thereby is hindered.[58] The bending rigidity can be determined via monitoring the fluctuations of the contour of a lipid membrane over time. As the fluctuations of the contour $r(\Theta, t)$ are relatively small compared to the size of the analyzed object (typically cells; within this study GUVs), the investigated object can be approximated by planar membrane sheets with the dimension $A = L \times L$.

Ihe fluctuations of the membrane patch can be represented in Fourier space given in equation (3.5).[9]

$$u(r,t) = \sum_q u_q(0)\text{exp}\left(iqr - \frac{t}{\tau}\right)$$ (3.5)

The relaxation time of the excited mode is denoted as τ, while q is the wave vector. Assuming that the membrane undergoes a lateral tension σ the elastic energy according to the bending-induced fluctuations can be described as the sum of the expansion-elastic energy presented in equation (3.2) and bending-elastic energy shown in equation (3.4) yielding equation (3.6).

$$G_{\text{ela}} = \frac{1}{2}\int \kappa \left[\frac{\partial^2 u}{\partial x^2} + \frac{\partial^2 u}{\partial y^2}\right]^2 + \sigma \left[\frac{\partial u}{\partial x} + \frac{\partial u}{\partial y}\right] dxdy$$ (3.6)

This shows that the observable undulations for each point $u(x,y)$ of a membrane patch with an area $A = L \times L$ depend on the tension σ and bending rigidity κ of the membrane. Implementing $u(x,y,t)$ in equation (3.6) enables to express the elastic energy as presented in equation (3.7).[9]

$$G_{\text{ela}} = \frac{L^2}{2}\left[\sum_{q_{min}}^{q_{max}} u_q^2(\kappa q^4 + \sigma q^2)\right]$$ (3.7)

As each natural vibration of the membrane represents one thermodynamic degree of freedom the equipartition theorem can be applied yielding the mean amplitudes $\langle u_q^2 \rangle$ of the natural vibration resulting in equation (3.8).

$$\langle u_q^2 \rangle = \frac{k_B T}{L^2(\kappa q^4 + \sigma q^2)}$$ (3.8)

Thereby, q is defined as $q^2 = q_x^2 + q_y^2$. Based on equation (3.8) and the work of Milner and Safran[59] the object can be described by an angle-dependent radius r following the spherical harmonics approach given in equation (3.9).

$$r(\Theta) = \langle r \rangle \left(1 + \sum_{l,m} u_{l,m} Y_{l,m}(\Theta)\right)$$ (3.9)

The angle is defined as Θ, $\langle r \rangle$ is the mean radius of the object and $Y_{l,m}$ the spherical harmonic for each mode l,m with the corresponding fluctuation amplitude $u_{l,m}$. Thus, the mean square amplitude of fluctuation can be derived from equation (3.6) resulting in equation (3.10).[60][48]

$$\langle u_{l,m}^2 \rangle = \frac{k_B T}{\kappa(l+2)(l-1)l(l+1) + \sigma\langle r \rangle^2 (l+2)(l-1)}$$ (3.10)

3.3   Flicker spectroscopy and image analysis

There is a variety of techniques to obtain the mechanical properties of a cell membrane. Most of these techniques like micropipette aspiration[61], optical trapping[62] or atomic force microscopy[63] rely on mechanical stimuli and thereby are invasive. Alternatively the naturally occuring thermal membrane fluctuations can be monitored. These fluctuations were already observed in the year 1890 on red blood cells and were described as "flickering"[57] resulting in the flicker spectroscopy method, where the continuous small fluctuations of "quasi-planar" membranes under thermal equilibrium are analyzed.[64] This enables to determine the mechanical properties tension σ and the bending rigidity κ of cells or other artifical model membranes.[47]

A typical phase contrast image of a giant unilamellar vesicle is shown in figure 3.2a) (left panel). The white line indicates the corresponding intensity profile (right panel). After applying the ImageJ "Image Differentials" plugin and choosing the option "Gradient Magnitude" a gradient of a greyscale image gets computed (see figure 3.2b), left panel). The corresponding intensity profile is shown in figure 3.2b), right panel giving a sharp peak that could be fitted well by a Gaussian (R=0.94), demonstrating that the edge detection was successful.

Thévanaz *et al.*[55] described a method to perform image differentiation and provided an open source software plugin "Image Differentials" based on it. In brief, data stored as discrete pixels can be expressed as continuous functions of the form described in equation (3.11).

$$f(x, y) = \sum_{k,1} c[k,1]\phi(x - k, y - 1) \tag{3.11}$$

The function $\phi(x, y) = \beta^3(x)\beta^3(y)$, is a tensor-product of cubic B-splines, used in the plugin and $c[k,1]$ the interpolation coefficients. The differentiation thereby results in equation (3.12) yielding an image with a sharper vesicle contour.[55]

$$\frac{\partial f(x, y)}{\partial y} = \sum_{k,1} c[k,1]\beta^3(x - k)\frac{\partial \beta^3(y - 1)}{\partial y} \tag{3.12}$$

Within this study the objects of interest are GUVs. Based on the sharp peaks obtained from the Gauss fit (green solid line) in figure 3.2b (right panel) the vesicle contour can be estimated for each frame in dependence of the azimuthal angle Θ and the distance between the center of mass and the contour r_{rim} shown in figure 3.3a). In figure 3.3b) r_{rim} is plotted versus the azimuth angle Θ.
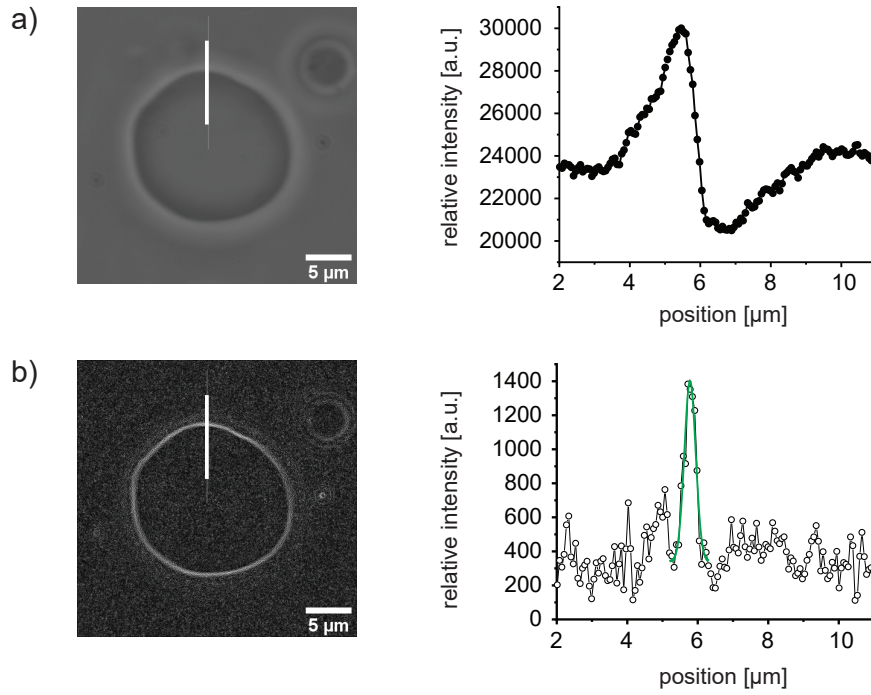
Figure 3.2. Image processing for flicker experiments. a) a typical vesicle imaged by phase contrast microscopy (left panel) and the corresponding relative intensity profile along the white solid line (right panel). b) image after processing with the ImageJ plugin "Image-Differentials" (left panel) yielding a sharp peak in the corresponding relative intensity profile along the white solid line fitted by a Gaussian function (green solid line, right panel).

In a next step, for all 300 consecutive frames the deviation of $r_{\text{rim}}(\Theta, t)$ from the averaged position is given as $R_{\text{rim}}(\Theta, t) = r_{\text{rim}}(\Theta, t) - \langle r_{\text{rim}}(\Theta, t) \rangle$ and is Fourier-transformed giving the mean square amplitude $\langle u(q)^2 \rangle$ of fluctuation as a function of q as shown in equation (3.13).
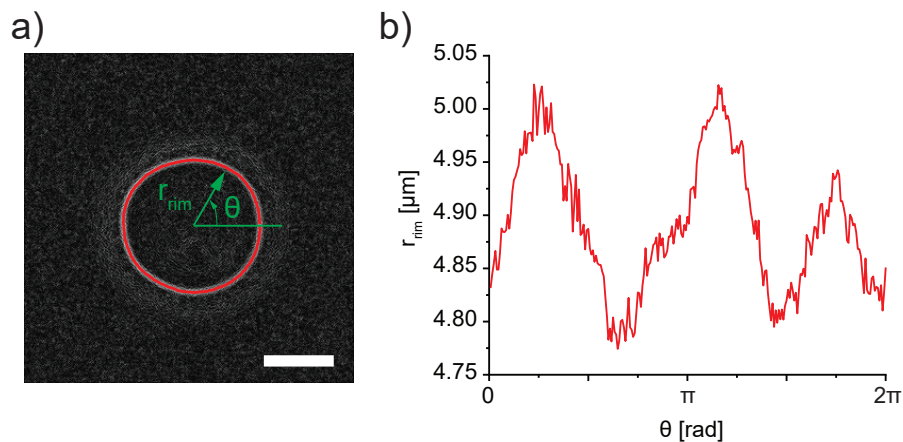
Figure 3.3. a) vesicle contour (red) obtained from radial intensity profile with azimuth angle Θ and the origin being the center of mass at each frame. b) obtained radius r_{rim} plotted versus Θ ($0 \leq \Theta \geq 2\pi$). The scale bar is 5 μm.

$$\langle u(q)^2 \rangle = \left\langle \left| \frac{2}{N} \sum_{n=0}^{N-1} R_{rim}(n\Delta\Theta, t)e^{\frac{2\pi i \langle r \rangle qn}{N}} \right|^2 \right\rangle \tag{3.13}$$

The wave number is denoted as q, $\langle \rangle$ is the time average over all frames and $\Delta\Theta = \frac{L}{N}$, with the $L = 2\pi\langle r \rangle$ and the mean radius $\langle r \rangle$ and $N = 256$ the sampling number. The theoretically predicted mean square amplitude, according to equation (3.13), can be expressed as a function of q_x, the continuous wave number corresponding to the experimental q yielding equation (3.14).[50]

$$\langle u(q_x, y = 0)^2 \rangle = \frac{k_B T}{L} \sqrt{\frac{\kappa}{2\sigma^2}} \left[\frac{1}{\sqrt{2\kappa q_x^2}} - \frac{1}{\sqrt{2\kappa q_x^2 + 2\sigma}} \right] \tag{3.14}$$

The bending rigidity κ was determined from fitting the bending dominated regime, where a power law $\langle u(q)^2 \rangle \propto q^{-3}$ is valid. During this study this was found to be the mode numbers of q between 3 to 5. The MSA data that follow the tension dominated power law $\langle u(q)^2 \rangle \propto q^{-1}$ were not utilized.

3.4 Wetting by droplets compared to vesicles

In case a vesicle is forming a contact to an adhesive substrate surface, it can gain adhesion energy by spreading onto the surface. As a consequence there must be an increase in bending energy to adapt the vesicle shape to the adhesive substrate. The adhesion energy is proportional to the contact area and therefore scales quadratically, while the bending energy scales only linearly along the contact line, resulting in the fact that the adhesion energy dominates the vesicle shape.[65]

In contrast, liquid droplets follow the classical concept of wetting, which is an omnipresent phenomenon in nature and in artificial systems.[66][67][68] There are ultrahydrophobic leaves which have self-cleaning properties. This effect, called lotus effect, is well known today.[69] In 1805 Thomas Young described the phenomenon of wetting of surfaces by liquid droplets resulting in the famous Young's equation given in equation (3.15).[28]

$$\cos(\theta) = \frac{\gamma_{\text{SV}} - \gamma_{\text{SL}}}{\gamma_{\text{LV}}} \tag{3.15}$$

The contact angle is defined as θ and is related to the surface tensions of the solid/vapor (γ_{SV}), solid/liquid (γ_{SL}) and liquid/vapor (γ_{LV}) interfaces as shown in figure 3.4.

In contrast to a droplet, a vesicle consists of a lipid bilayer, which has a bending rigidity κ. Under the assumption that $\kappa \neq 0$ the vesicle shape in the vicinity of the contact area is not determined via the surface tension σ, but via the contact curvature. The
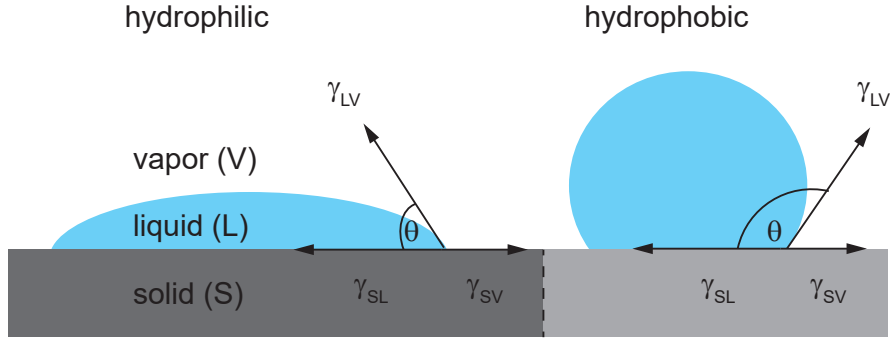
Figure 3.4. Young-Dupré wetting of liquid droplets showing hydrophilic (left) and hydrophobic (right) behavior. The broken line indicates different surface energies between left (dark grey) and right (light grey), γ_{SV} is the surface energy between the solid substrate and the vapor, γ_{SL} is the surface energy between the solid substrate and the liquid and γ_{LV} is the surface energy between the liquid droplet and the vapor.

free energy functional $F = G_b + G_W + G_P + G_\sigma$ is minimized, where G_b is the bending-elastic energy[17] (see equation (3.4)). Additionally, $G_W = \Delta\gamma_W A$ with $\Delta\gamma_W$ the adhesion free energy and the contact area A, while G_P and G_σ describe the volume and area constraints of the vesicle, which results in equation (3.16).[18]

If the vesicle has no contact to the surface at $G_W = 0$, minimization of the free energy of equation (3.16) leads to the shape equation for free vesicles, considering axisymmetric shapes.[70]

$$\frac{\kappa}{2}\int dS(R_1^{-1} + R_2^{-1} - C_0)^2 - \Delta\gamma_W A + P\int dV + \sigma\int dS \qquad (3.16)$$

In case of bound vesicles the shape equations still are valid, as the adhesion term G_W only functions as a boundary condition at the contact point. The contact angle Θ is set to be $\Theta = \pi$ resulting in a vesicle having no contact. Next, the contact point is varied resulting in equation (3.17).[18]

$$C_{1max} = \sqrt{\frac{2\Delta\gamma_W}{\kappa}} \iff \Delta\gamma_W = \frac{1}{2}\kappa C_{1max}^2 \qquad (3.17)$$

The principal curvature along the vesicle contour at the contact point is represented by C_{1max}, while $\Delta\gamma_W$ is the adhesion free energy, which is further explained and investigated in sections 3.10.1 and 4.5. According to Seifert and Lipowsky[18] for an adhering vesicle a boundary condition, the transversality condition must hold where the adhesion strength can be described by a dimensionless parameter ϵ_W represented in equation (3.18).

$$(C_{1max}R_0)^2 = 2\epsilon_W \qquad (3.18)$$

For $\kappa = 0$ the minimization of the free energy yields the Young-equation for vesicle adhesion. Bell *et al.*[22] were the first applying this concept to cell adhesion employing equation (3.19).

$$\Delta\gamma_W = \sigma(1 + \cos\Theta) \tag{3.19}$$

Obviously, equation (3.19) results for a non adhering vesicle having a contact angle $\Theta = 180°$ in an adhesion free energy of $\Delta\gamma_W = 0$.

3.5 Size and conformation of polymer chains

There are several strategies to couple polymer brushes onto a surface. One method is by physical, non-covalent interactions between moieties of the polymer and a surface shown in figure 3.5a). During this study the grafting onto strategy was used, where the coupling between the surface and the brushes occurs due to chemical coupling reactions or functional groups, which enables to control the grafting density via defined surface modifications as illustrated in figure 3.5b). Another strategy is the grafting from strategy depositing an initiator molecule onto the surface from which the polymerization starts as shown schematically in figure 3.5c).[71]
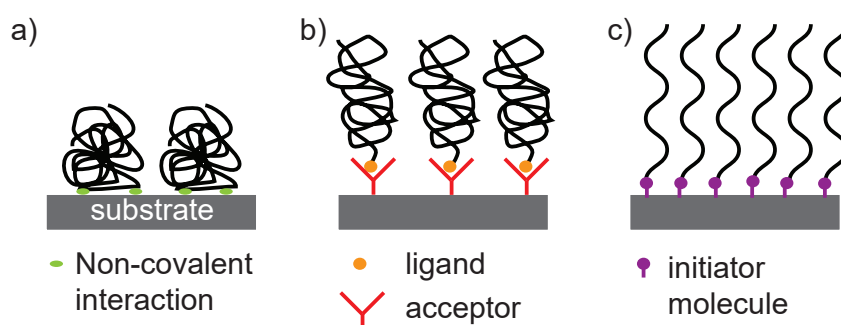
Figure 3.5. Polymers grafted onto a surface using various strategies. a) polymer attached to a surface via non-covalent interactions, b) coupled to the surface via ligand/acceptor interactions (grafting onto), c) grafting from the surface via initiator molecules (adapted from[71]).

Grafted polymer brushes have a large variety of applications, as they enable to manufacture surfaces with defined physicochemical properties. The coating of a silica wafer with poly(N-isopropylacrylamide) (PNIPAAm) e.g. enables to modulate the contact angle of a droplet via changing the temperature.[30] Even the movement of a Si-particle could have been realized via switching the brush conformations of a mixture of poly (methylmethacrylate) (PMMA) and polyglycidylmethacrylate (PGMA) brushes due to switching the topography of the substrate.[72] Sundaram *et al.* showed that proteins could be adsorbed and detached, by switching the pH value, from a surface coated

with brushes containing tertiary amine and carboxylic acid moieties.[73] Also cell adhesion can be controlled via polymer coated substrates, which plays a key role in the field of bio fouling.[74][75] In this study the adhesion between cell models (GUVs) and a bio-inspired polymer coated substrates will be investigated in sections 4 and 5.

From the theoretical view point it is interesting to consider an expression for the length of a polymer in solution. Assuming a polymer chain consisting out of N monomers, where each monomer represents a link, the length of a single monomer is represented by α in the following. If all bonds can rotate independently (random walk) the end-to-end vector can be expressed as: $L = \sum_{i=1}^{N} \alpha_i$. Thus, the mean square end-to-end distance is given in equation (3.20).[9]

$$\langle L^2 \rangle = \left\langle \left(\sum_{i=1}^{N} \alpha_i \right) \left(\sum_{j=1}^{N} \alpha_j \right) \right\rangle \tag{3.20}$$

Expanding the sum in equation (3.20) results in equation (3.21).

$$\langle L^2 \rangle = \left\langle \sum_i \sum_j \alpha_i \alpha_j \right\rangle \tag{3.21}$$

Selecting N cases where $i = j$ results in equation (3.22).

$$\langle L^2 \rangle = N\alpha^2 + \left\langle \sum_{i \neq j} \alpha_i \alpha_j \right\rangle \tag{3.22}$$

In the case of freely joint chains the different links N are uncorrelated resulting in $\sum_{i \neq j} \alpha_i \alpha_j = 0$ yielding the random walk given in equation (3.23).

$$\langle L^2 \rangle = N\alpha^2 \ or \ \sqrt{\langle L^2 \rangle} = \alpha\sqrt{N} \tag{3.23}$$

According to the Boltzmann principle, the entropy and the free energy of freely joint chains are calculated having the distribution function $P(L)$ for the end-to-end distance L, which can be expressed as a Gaussian function following equation (3.24).[76]

$$P(L) = \left(\frac{2\pi \langle L^2 \rangle}{3} \right)^{-\frac{3}{2}} \exp\left(-\frac{3}{2} \frac{L^2}{\langle L^2 \rangle} \right) \tag{3.24}$$

The Boltzmann equation yields the configurational entropy $S(L)$ of a polymer as a function of its elongation, which is expressed in equation (3.25).

$$S(L) = \frac{3k_B L^2}{2\langle L^2 \rangle} \tag{3.25}$$

Elongating the chains results in an decrease in the entropy $S(L)$ and thereby in an increase in the free energy $G(L)$ presented in equation (3.26).[77]

$$G(L) = G(0) + \frac{3}{2}\frac{k_B T}{\langle L^2 \rangle}L^2 \tag{3.26}$$

Equation (3.26) suggests that the polymer chain is confined in a harmonic potential with the spring constant $K = \frac{3k_B T}{\langle L^2 \rangle}$.

In experimental systems the polymer chains can not rotate freely, but have finite bond angles. This hindered rotation leads to an extension of the segment length by using a geometric factor C_g. The so called Kuhn's law is given in equation (3.27).[76,78]

$$\langle L^2 \rangle = C_g N' \alpha^2 = N' b^2 \tag{3.27}$$

The Kuhn length is denoted by $b = \alpha\sqrt{C_g}$. Consequently, the real polymer chains can be approximated as freely joint chains with a modified segment length b and unit number N'. It needs to be considered that the polymer chains also have a certain volume, so that two monomers can not be at the same place (finite excluded volume). In equation (3.28) the finite excluded volume can be considered as a repulsion between the ith and jth spheres similarly to a van der Waals gas.

$$w_{ij} = \nu k_B T \delta(r_j - r_i) \tag{3.28}$$

Thereby, ν is representing an empirical parameter for the excluded volume and $\delta(r_j - r_i)$ is the Dirac's delta function for hard spheres. Considering N monomers confined in a volume R^3 the monomer concentration is given as $c_m = \frac{N}{R^3}$. Thus, the repulsive energy density per unit volume is given in equation (3.29)

$$w_{ij} = \nu k_B T c_m^2 \tag{3.29}$$

The probability for the collision of two monomers is denoted by c_m^2. Assuming the volume of the polymer be R^3, the contribution of the repulsion to the inner energy yields to equation (3.30).

$$\Delta U_{\text{rep}} = R^3 w_{ij} = \frac{\nu k_B T N^2}{R^3} \tag{3.30}$$

The elastic energy ΔG_{ela} (compare (3.26)) counter-balances the repulsive interaction yielding to a total free energy as given in equation (3.31)

$$\Delta G_{\text{tot}} = \Delta U_{\text{rep}} + \Delta G_{\text{ela}} \tag{3.31}$$

The elastic energy can be expressed as $\Delta G_{\text{ela}} = \frac{3}{2}\frac{k_B T}{N\alpha^2}R^2$. Minimizing the free energy $\frac{d\Delta G_{\text{tot}}}{dR} = 0$ yields the mean radius $\langle R \rangle$ of the polymer, also called Flory radius, given in

equation (3.32).[79]

$$R_F = (\alpha^2 \nu)^{\frac{1}{5}} N^{\frac{3}{5}} \tag{3.32}$$

This expression is valid for chains in bulk medium. For polymers confined in e.g. two-dimensional networks as found in biological systems $R_F \propto \alpha N^{\frac{3}{D+2}}$ can be rewritten for various dimensions D. Thereby the mean radius of a polymer R_F is connected with the number of monomers N and the monomer size α.[80] As it is difficult to access the end-to-end distance $\langle L \rangle$ experimentally the radius of gyration R_g is introduced, which is defined as the average distance from the center of gravity to the respective chain segment as described in equation (3.33).[81]

$$R_g^2 = \frac{1}{N} \left\langle \sum_{k=1}^{N} (r_k - r_a v)^2 \right\rangle \tag{3.33}$$

For polymer chains undergoing 3D random walk R_g is defined as presented in equation (3.34).[82]

$$R_g = \frac{1}{\sqrt{6}} \langle L \rangle \tag{3.34}$$

The radius of gyration R_g can be determined experimentally via DLS experiments according to the Stokes-Einstein relationship $R_g = \frac{k_B T}{6\pi \eta D}$, where the diffusion coefficient D can be obtained by the light scattering experiments. The viscosity is represented by η. Polymers grafted onto a surface can exist in the mushroom- or brush conformation depending on the distance s between chains as shown in figure 3.6.
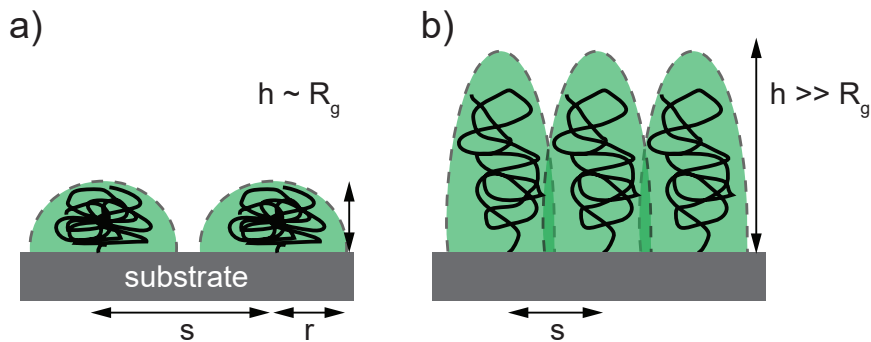
Figure 3.6. Polymer chains grafted onto a surface at various distances s. a) mushroom conformation showing no interaction between polymer chains ($s > 2r$). Thereby the radius of gyration R_g comparable with the height ($h \approx R_g$). b) brush conformation, interaction between chains (dark green cross sections) ($s < 2r$) with the height of the brush much larger than the radius of gyration ($h >> R_g$) adapted from.[83]

For a distance larger than two times the radius $s > 2r$ of the polymer in the vicinity of the surface the chains can not interact with each other and hence the mushroom conformation is favored as shown in figure 3.6a). The brush conformation is preferred

vice versa if the distance between two chains is $s < 2\,r$ as shown in figure 3.6b), where the green areas surrounded by the dotted lines represent the space which might be occupied due to the stochastic nature of polymer chains.

3.6   Three dimensional image creation in confocal microscopy

Compared to a conventional fluorescence microscope in confocal fluorescence microscopy most of the light that is not from the focal plane is excluded. Thus, a confocal microscope creates sharp image stacks of objects that would appear blurred otherwise. In figure 3.7a) a schematic illustration of a spherical object is shown where the white dashed lines indicate the different focal planes, which are monitored in a distance Δz between each other. This procedure opens up the possibility to create 3D reconstructions of an object by assembling the different image planes taken in a distance of Δz in between the focal planes, so called z-stacks. With the aid of a software (e.g. ImageJ) the z-stacks are merged enabling to obtain the confocal side view images as shown schematically in figure 3.7b).[84]
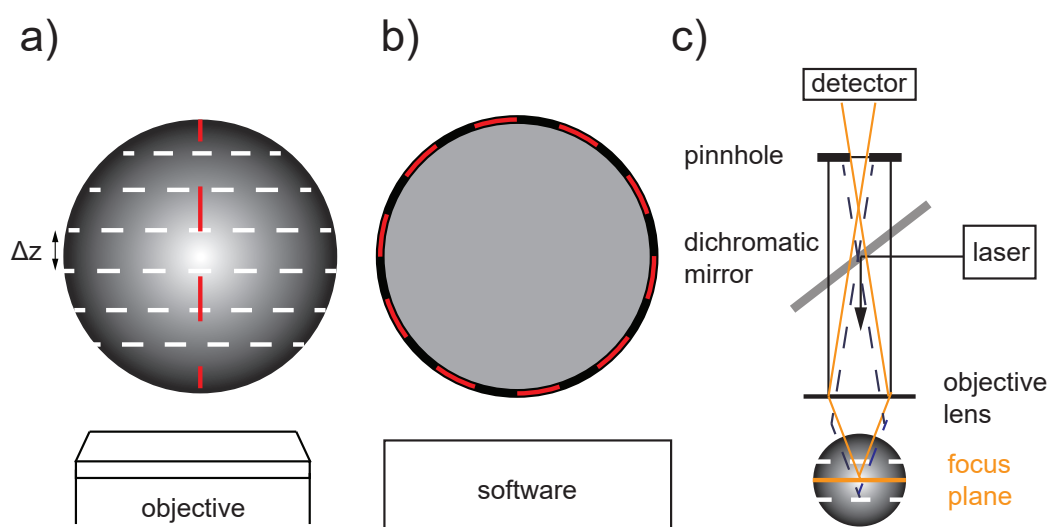
Figure 3.7. Schematic illustration of a confocal microscope objective monitoring a vesicle with a distance between focal plances of Δz (a). Deconvoluted confocal side view (b). Setup of an confocal microscope with its main components. The orange rays correspond to the focal plane, while the blue rays correspond to the out of focus light (c) (adapted from[85]).

In figure 3.7c) the main components of a confocal microscope are illustrated schematically. One of the key elements of an confocal microscope is the pinhole, which excludes light intensity from out-of-focus planes (dotted blue lines).[85] Besides, a computational method is used to reduce the out-of-focus fluorescence intensity in 3D reconstructed images. This process is called deconvolution and can be understood as an image restoration procedure. A typical deconvolution algorithm can be written as presented in

equation (3.35), where the obtained image is represented by I (x,y,z), PSF (x,y,z) is the point spread function (PSF) and the unkown distribution of light in the 3D object is represented by S (x,y,z).[86]

$$I(x, y, z) = S(x, y, z) \circledast PSF(x, y, z) \tag{3.35}$$

Imaging a sub-resolution fluorescently labeled micro-particle shows a diffraction pattern in the equatorial plane, which is known as airy disc. Such a pattern can also be observed in the axial plane. To resolve two points, according to the Rayleigh criterion, the points can not be closer than the center of the PSF and the first destructive interference band. The resolution is obtained from the FWHM of the 3D PSF, which is generated from sub-resolution fluorescently labeled micro-spheres, where the lateral resolution Γ_L can be calculated as shown in equation (3.36) and the axial resolution Γ_A can be calculated as shown in equation (3.37). The wavelength of excitation is denoted by λ, NA is the numerical aperture of the microscope and n is the refractive index.[87]

$$\Gamma_L = \frac{0.51\lambda}{NA} \tag{3.36}$$

$$\Gamma_A = \frac{0.88\lambda}{n - \sqrt{n^2 - NA^2}} \tag{3.37}$$

The $\circledast$-symbol used in equation (3.35) represents the mathematical operator for convolution. This is an operation where the PSF is shifted so that it is centered at each point. As I (x,y,z) is known this method enables to obtain S (x,y,z). This process is known as deconvolution.[86] In detail the convolution of S (x,y,z) and PSF (x,y,z) can be written as presented in equation (3.38).[88]

$$(S \circledast PSF)(t) = \int_{-\infty}^{\infty} S(\tau) PSF(t - \tau) d\tau \tag{3.38}$$

The convolution typically is done automatically by an alogrithm, which is implemented in the software. In this study the "NIS-elements" software was used provided by the imaging facility.

3.7 Specular X-Ray reflectivity

To characterize thin films X-ray reflectivity (XRR) is an established method. In section 3.7.1 the basic principle of reflectivity measurements is explained, while in section 3.7.2 the method is expanded to more complex systems with several stratified layers. As experimental systems do not have perfectly smooth interfaces in section 3.7.3 the concept of surface roughness is introduced.

3.7.1 Basic principle

The discovery of X-rays by Röntgen in 1895[89] was not only important for medical progress but also enabled the characterization of sample structures on molecular length scales as the wavelength λ for X-rays is in the range of 1 Å. The energy E of an X-ray beam is directly correlated to its wavelength λ via the Planck-Einstein relation given in equation (3.39).

$$E = \frac{hc}{\lambda} \tag{3.39}$$

Here, $h \approx 4.1357 \times 10^{-15}$ eVs denotes the Planck constant and $c \approx 2.9979 \times 10^{8}$ ms^{-1} the speed of light in vacuum. Compton was the first who established using X-rays to characterize surfaces, where he measured the reflected intensity R of a monochromatic X-ray beam as a function of the incidence angle α_i.[90] Setting the boundary condition for the amplitude of the reflected beam continuity of the electric and magnetic field at the interface yields the well known Fresnel relations.[91] Here each medium is parameterized with a refractive index n given in equation (3.40).

$$n = 1 - \delta + i\beta \tag{3.40}$$

The real part δ and the imaginary part β of the refractive index n are proportional to λ^2 respectively to λ as expressed in equations (3.41) and (3.42).

$$\delta = \frac{\lambda^2}{2\pi} SLD \tag{3.41}$$

$$\beta = \frac{\lambda}{4\pi} \mu \tag{3.42}$$

λ is the wavelength of the X-ray beam, the scattering length density (SLD) is proportional to the classical radius of an electron r_0 and to the electron density ρ_{el} via $SLD = r_0 \rho_{el}$. The absorption coefficient of the beam in a specific medium is denoted by μ. Thereby the real part δ of the refractive index shows the dependency on the interaction between materials, as the SLD is proportional to the electron density ρ_{el}, and radiation λ. For representative SLDs the real part δ is smaller than unity and the imaginary part β usually is one to two orders of magnitude lower than δ.[92] This leads to a refractive index of $n < 1$ for X-rays.

Assuming an incident plane wave impinging at a smooth interface in between two media with different refractive indices n_0 and n_1 as shown in figure 3.8 the incident beam can undergo reflection and refraction.[93] In the case of reflection the incident beam gets reflected back to the medium 0, while in case of refraction the incident beam is

refracted into medium 1, where the refraction can be described by Snell's law, given in equation (3.44). As the refractive index for X-rays is smaller than unity the ray gets refracted towards the interface as shown in figure 3.8. The green vertical arrow represents the momentum transfer q_z perpendicular to the surface plane, which can be expressed as the difference of the wave vector of the refracted beam k_r and the incident beam k_i given in equation (3.43).

$$\vec{q_z} = \vec{k_r} - \vec{k_i} \tag{3.43}$$

The angle at which refraction occurs α_t is depending on the incidence angle α_i and the ratio of refractive indices, which is expressed in equation (3.44).

$$\cos(\alpha_t) = \frac{n_0}{n_1}\cos(\alpha_i) \tag{3.44}$$
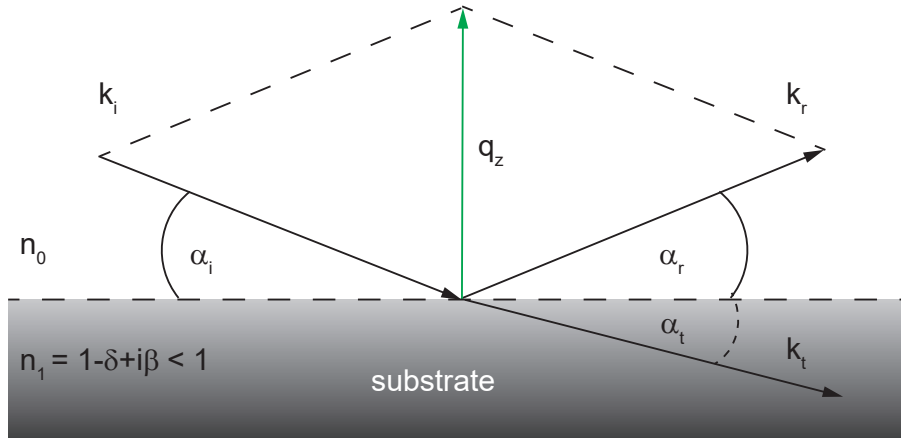
Figure 3.8. X-ray beam impinging a surface at incidence angle α_i with the wave vector $\vec{k_i}$. The momentum transfer q_z perpendicular to the surface plane is defined as $\vec{q_z} = \vec{k_r} - \vec{k_i}$.

If $\alpha_t = 0$ and $\cos(\alpha_t) = 1$ there is no transmission and the beam is totally reflected back to medium 0. This occurs at and below a definite angle of incidence which is called critical angle α_c. Neglecting absorption this leads to a simplified Snells law given in equation (3.45).

$$\cos(\alpha_i) = n_1 = 1 - \delta \tag{3.45}$$

As for most materials δ is in the order of 10^{-5}Å^{-2} the critical angle α_c is in the order of mrad. This enables one to express $\cos(\alpha_c)$ by the approximation for small angles obtained via a Taylor series development as $1 - \frac{\alpha_c^2}{2}$. Thereby the well known approximation for the critical angle $\alpha_c \approx \sqrt{2\delta}$ is obtained.[94]

Deriving an expression for the reflectivity can be realized by starting with the propagation equation of waves within a medium with a certain dielectric constant, the Helmholtz equation, which is given in equation (3.46).[91]

$$\nabla^2 E + k_j^2 E = 0 \tag{3.46}$$

Solving the Helmholtz equation (3.46) yields an expression for the electric field E_j in a homogeneous medium j as shown in equation (3.47) with $j=i$ for incident, $j=r$ for reflected and $j=t$ for transmitted X-rays, the wave vector $k_j = 2\pi/\lambda$ in medium j and the respective amplitude A_j.

$$E_j = A_j \mathsf{exp}(i(\omega t - k_j r)) \tag{3.47}$$

For the following derivations it is assumed that the z-component of the electric field is continuous (z=0). Assuming further a thickness of the medium that the transmitted beam can be completely absorbed and that Snell-Descartes second law is valid the amplitude of the transmitted X-rays can be expressed as the sum of the amplitudes A_i of the incident and refracted ones as given in equation (3.48).[95]

$$A_i + A_r = A_t \tag{3.48}$$

Thereby, the following relation shown in equation (3.49) holds.

$$A_i k_i + A_r k_r = A_t k_t \tag{3.49}$$

The reflection- and transmission coefficients can be described via the ratios between the amplitudes of the reflected and the incident amplitude as shown in equation (3.50) respectively the amplitude between the refracted amplitude and the incident amplitude which is given in equation (3.51).

$$r_{0,1}^F = \frac{A_r}{A_i} \tag{3.50}$$

$$t_{0,1}^F = \frac{A_t}{A_i} \tag{3.51}$$

In accordance to the relation presented in equation (3.49) the Fresnel equations for reflection (3.52) and transmission (3.53) are obtained.

$$r_{0,1}^F = \frac{k_{i,z} - k_{r,z}}{k_{i,z} + k_{r,z}} \tag{3.52}$$

$$t_{0,1}^F = \frac{2k_{r,z}}{k_{i,z} + k_{r,z}} \tag{3.53}$$

with the wave vectors $k_{i,z} = k\sin(\alpha_i)$ and $k_{r,z} = nk\sin(\alpha_t)$.

The square modulus of $r_{0,1}^F$ yields the reflectivity $R(q_z)^F$ given in equation (3.54) which is given in terms of the momentum transfer vector q_z defined in equation (3.55).

$$R(q_z)^F = \left| \frac{q_z - \sqrt{q_z^2 - q_c^2}}{q_z + \sqrt{q_z^2 - q_c^2}} \right|^2 \tag{3.54}$$

Thereby, q_z is the inverse proportional to the wavelength λ of the X-ray beam and proportional to the sine of the incident angle $\sin(\alpha_i)$.

$$q_z = \frac{4\pi}{\lambda}\sin(\alpha_i) \tag{3.55}$$

In figure 3.9 a simulated reflectivity curve for a silicon wafer in air with a silicon oxide thickness of 10 Å is depicted to show the 3 characteristic regimes in reflectivity profiles. At the very low q-range $0 < q_z < q_c$ total reflection occurs as $R(q_z) < q_c = 1$, where q_c is the momentum transfer perpendicular to the surface plane at the critical angle α_c.
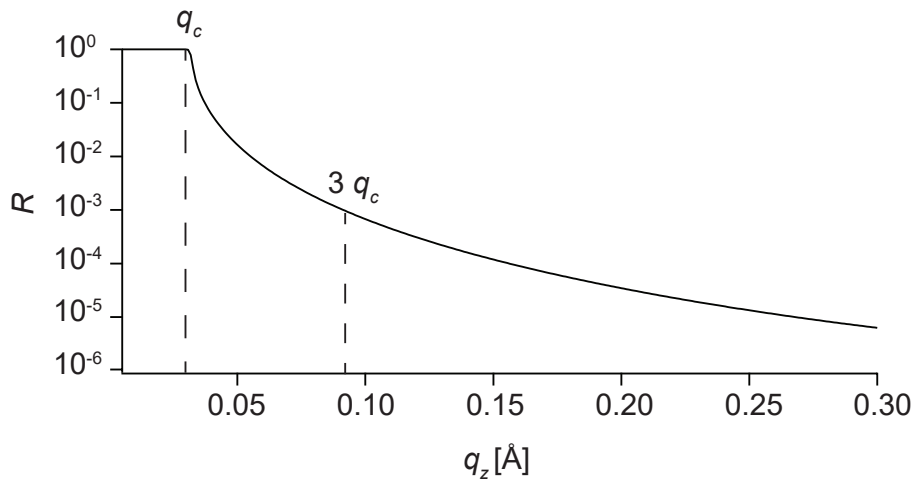
Figure 3.9. Simulated curve representing the Fresnel reflectivity of an silicon wafer in air with an oxide layer thickness of 10 Å.

For $q_z = q_c$ there is a steep decay in the reflectivity curve due to transmission. In the regime where $q_z > 3\,q_c$ the reflectivity follows a q_z^{-4} power law as shown in equation (3.56).[91]

$$R(q_z)^F = \frac{q_c^4}{16q_z^4} \tag{3.56}$$

3.7.2 Stratified layers

The equations above describe the reflections on a single smooth layer. Usually XRR is used to probe experimental systems with several layers. That is why an extension for a system with several layers is needed. The work of Parratt[96] describes a recursive method to calculate a reflectivity profile for a stratified layer system as schematically shown in figure 3.10 and is one of the most cited in the field of XRR.
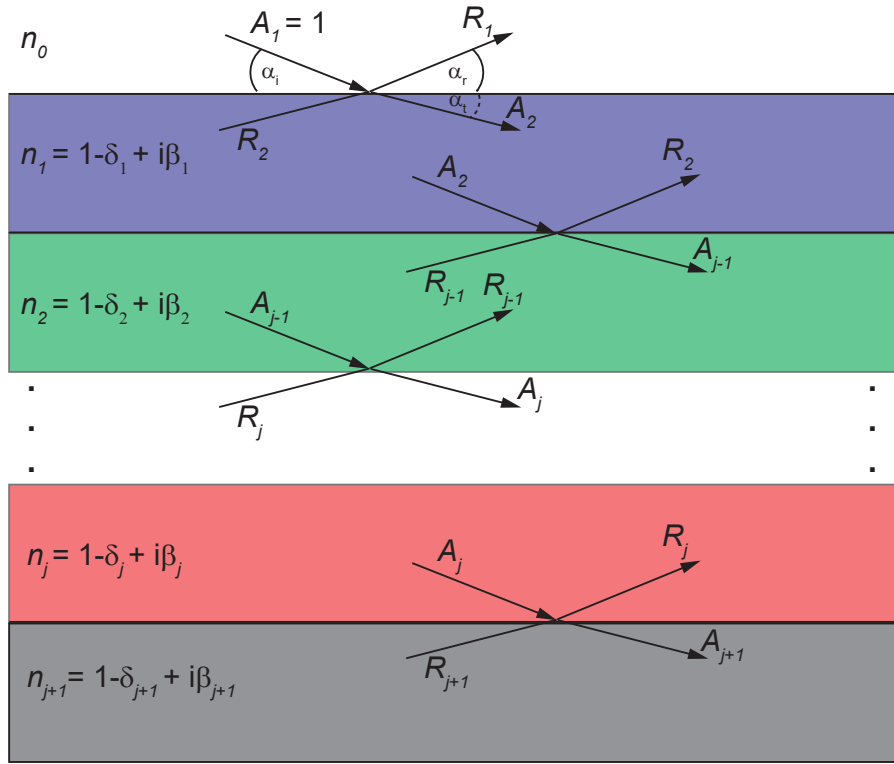
Figure 3.10. Reflectivity on multiple layers (adapted from[92]).

A X-ray wave normalized to unity $A_1 = 1$ as illustrated in figure 3.10 is impinging a surface at an angle of incidence α_i. The ratio between the reflected and impinging amplitudes for layer $j+1$ can be expressed as $X_{j+1} = \frac{R_{j+1}}{A_{j+1}}$. Consequently for the layer j above, X_j can be calculated as expressed in equation (3.57).

$$X_j = \frac{R_j}{A_j} = \exp(-2ik_{z,j}z_j)\frac{r_{j,j+1} + X_{j+1}\exp(2ik_{z,j+1}z_j)}{1 + r_{j,j+1} + X_{j+1}\exp(2ik_{z,j+1}z_j)} \tag{3.57}$$

with $r_{j,j+1} = \frac{k_{z,j}-k_{z,j+1}}{k_{z,j}+k_{z,j+1}}$ the Fresnel coefficient of the interface j; $k_{z,j} = k\sqrt{(n_j^2 - \cos(\alpha_i)^2)}$ is the z-component of the wave vector in layer j. As the substrate is assumed to be much thicker than the penetration depth of X-rays (see equation 8.1), there is no

reflection from the substrate. Thereby the recursion starts at $R_{j+1} = X_{j+1} = 0$ which after $j+N$ iterations yields equation 3.58.

$$R = |X_1^2| = |R_1^2| \tag{3.58}$$

As the sum of the reflected and transmitted beam must be unity $R_1 + T_1 = 1$ the amplitudes R_j and T_j in all layers can be expressed recursively by equations (3.59) and (3.60).

$$R_{j+1} = \frac{1}{t_{j+1,j}}(T_j r_{j+1,j}\text{exp}(-K) + R_j\text{exp}(-K)) \tag{3.59}$$

$$T_{j+1} = \frac{1}{t_{j+1,j}}(T_j\text{exp}(K) + R_j r_{j+1,j}\text{exp}(K)) \tag{3.60}$$

Thereby, K can be expressed as $K = i(k_{z,j+1} + k_{z,j})z_j$.[92]

3.7.3 Rough interfaces

Describing the reflectivity near the critical angle a_c by using equation (3.56) is not possible, as surface roughness is not taken into account.[97] Real samples always have a certain roughness, e.g. a water surface has a roughness of approximately 3 Å at room temperature due to thermally excited capillary waves.[98] Up to now the refractive index was assumed to be constant within each layer n_j with sharp transitions to the next layer n_{j+1}. In case of rough interfaces the refractive index needs to be expressed as a continuous variation of the refractive index $n_j(x,y,z)$ which leads to a SLD depending on x,y,z $\rho(x,y,z)$ and can be described by an error function. In case of specular reflectivity one is interested in the wave vector q_z which yields to the following expression for a one-dimensional refractive index profile in dependence of z, which is given in equation (3.61).

$$n_j(z) = \int\int n_j(x,y,z)dydx \tag{3.61}$$

Taking equation (3.61) into account the equations (3.59) and (3.60) can be rewritten considering the root mean square roughness σ. This yields to the modified Fresnel coefficients for rough interfaces $\tilde{r}_{j+1,j}$ and $\tilde{t}_{j+1,j}$ as expressed in equations (3.62) and (3.63).[1]

$$\tilde{r}_{j,j+1} = r_{j,j+1}\text{exp}(-2k_{z,j}^2 k\sigma_j^2) \tag{3.62}$$

---

[1]$\text{exp}(-2k_{z,j}k_{z,j+1}\sigma)$ is known as the Névot-Croce factor, which is used to mimic the effect of surface roughness in calculated reflectivity profiles[99]

$$\tilde{t}_{j,j+1} = t_{j,j+1}\exp(-(k_{z,j} - k_{z,j+1})^2\sigma_j^2/2) \tag{3.63}$$

As a result the reflectivity of layer systems with rough interfaces can be calculated by implementing the modified Fresnel coefficients in equation (3.57).[92]

3.8 Debye screening length

In a solution with positively and negatively charged ions, the positively charged cations are more likely to be found near anions and *vice versa*. Although the solution is neutrally charged, in the vicinity of ions there is an excess of their conunter ions, the so called ionic atmosphere. As there are electrostatic interactions between ions and their ionic atmospheres, the chemical potential of the central ion is lowered.[100] Analogous, on a charged surface the charge density $\rho(x)$ and the potential $\phi(x)$ can be related by using the Poisson's equation, which is given in equation (3.64). In this study a charged Si-particle (d = 3 µm) is used.

$$\frac{d^2\phi(x)}{dx^2} = -\frac{\rho(x)}{\epsilon_r\epsilon_0} \tag{3.64}$$

The dielectric constant of the medium is denoted by ϵ_r, the dielectric constant of the vacuum is denoted by ϵ_0 and the distance from the charged surface is given as x. The charge density can be described by the Boltzmann distribution[101].

$$\rho(x) = \sum_i z_i e n_i^0 \exp\left(-\frac{z_i e\phi(x)}{k_B T}\right) \tag{3.65}$$

The charge of the i-th ion is denoted by z_i, e is the elementary charge and n_i^0 the number of moles of ions of type i. Equation (3.65) and equation (3.64) can be combined resulting in the Poisson-Boltzmann equation, which is only dependent on the potential ϕ as given in equation (3.66).

$$\frac{d^2\phi(x)}{dx^2} = -\frac{1}{\epsilon_r\epsilon_0}\sum_i z_i e n_i^0 \exp\left(-\frac{z_i e\phi(x)}{k_B T}\right) \tag{3.66}$$

Assuming the electrostatic interactions between the surface and the oppositely charged ions in solution, $\Delta\phi$, to be much smaller than their average kinetic energy, which is valid for $\Delta\phi \approx$ 25-80 mV, equation (3.66) can be written as given in equation (3.67).

$$\frac{d^2\phi(x)}{dx^2} = -\frac{2N_A e^2 I}{\epsilon_r\epsilon_0 k_B T}\phi(x) \tag{3.67}$$

The ionic strength I is defined as $I = \frac{1}{2}\sum_i c_i z_i^2$. The right term of equation (3.67) can be simplified yielding an expression for κ, which is presented in equation (3.68).[100]

$$\kappa = \sqrt{\frac{2N_A e^2 I}{\epsilon_r \epsilon_0 k_B T}} \tag{3.68}$$

Thereby, κ^{-1} is defined as the Debye screening length yielding equation (3.69).

$$\frac{d^2\phi(x)}{dx^2} = \kappa^2 \phi(x) \tag{3.69}$$

Equation (3.69) can be solved by the solution approach presented in equation (3.70).

$$\phi \propto \exp(-\lambda x) \tag{3.70}$$

Implementing this expression in equation (3.69) yields $\lambda_{1,2} = \pm \kappa$. Therefore the general solution presented in equation 3.71 can be obtained.

$$\phi_i = A_1 \exp(\kappa x) + A_2 \exp(-\kappa x) \tag{3.71}$$

Assuming the boundary condition that the electrostatic potential $\phi = 0$ at an infinite distance x the coefficient $A_1 = 0$, while for the second boundary condition $x = 0$ the potential equals the potential on the electrode yielding $\phi = \phi_0$. Thus, the potential distribution according to the distance x and the salt concentration, included in the expression for the ionic strength I, can be expressed as given in equation (3.72).[102]

$$\phi(x) = \phi_0 \exp(-\kappa x) \tag{3.72}$$

In figure 3.11 the potential ϕ is plotted against the distance from the charged surface for various salt concentrations yielding an exponential decay function, where the Debye screening length κ^{-1} is defined as the distance x where the potential equals ϕ_0/e. As an example in case of a surface potential of 40 mV this yields a potential of 40 mV/$e \approx 14.7$ mV corresponding to the black horizontal line in figure 3.11 for the respective κ^{-1}. The vertical dashed lines in figure 3.11 indicate the respective Debye screening lengths for salt concentrations of a monovalent salt c = 1, 10 and 100 mM resulting in $\kappa^{-1}_{1\,mM} \approx 10$ nm (red dashed line), $\kappa^{-1}_{10\,mM} \approx 3$ nm (green dashed line) and $\kappa^{-1}_{100\,mM} \approx 1$ nm (blue dashed line).
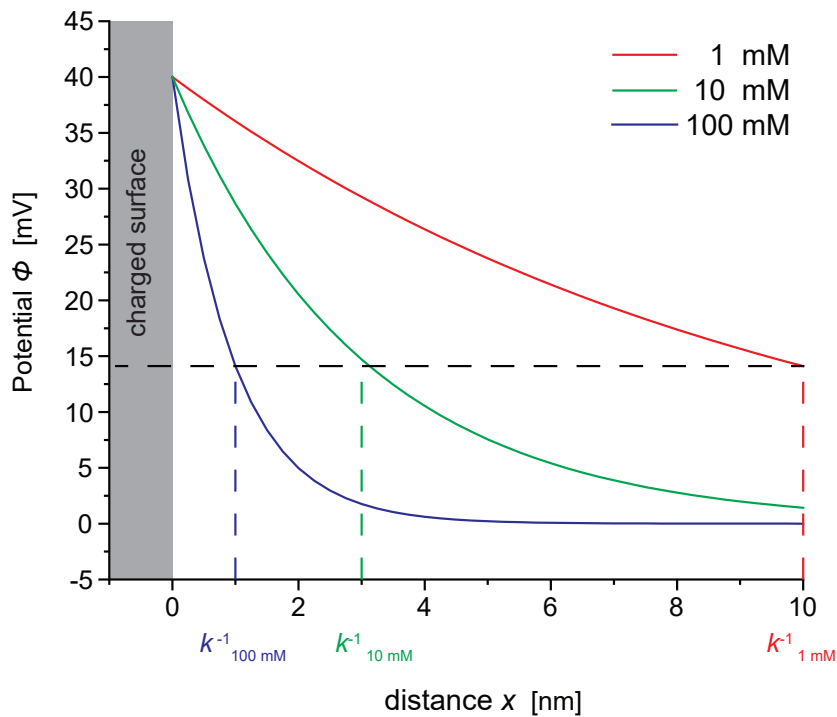
Figure 3.11. Exponential decay of the potential ϕ versus the distance x from a charged surface in accordance to increasing salt concentrations; 1 mM (red), 10 mM (green), 100 mM (blue). The vertical dashed lines indicate the respective Debye screening length κ^{-1}.

3.9 Zeta potential

The distribution of ions in the vicinity of a charged particle is affected by the net charge of the respective particle. Assuming a negatively charged particle, a double layer is formed, which consists out of two different layers. Next to the particle positively charged ions accumulate, which are strongly bound to the negatively charged particle surface. This layer is the so called Helmholtz- or Stern layer.[103] The outer region consists of a mixture of positively and negatively charged particles which are not strongly bound to the particle surface. This layer is called diffusive layer. Both layers form the electrical double layer.[104][105] When a particle is accelerated in an electric field, the Stern layer and some parts of the diffusive layer move with the particle. The other part of the diffusive layer does not move and stays at its position in the bulk. This border is called slipping plane which is indicated by the dashed line in figure 3.12. The potential at this boundary is called zeta potential and can be calculated via the electrophoretic mobility U_{e} following equation (3.73).

$$U_{\mathrm{e}} = \frac{v}{E} \tag{3.73}$$

The velocity of the particle is denoted by v and E is the electric field strength. Both parameters can be measured by the instrument. This enables to calculate the elec-
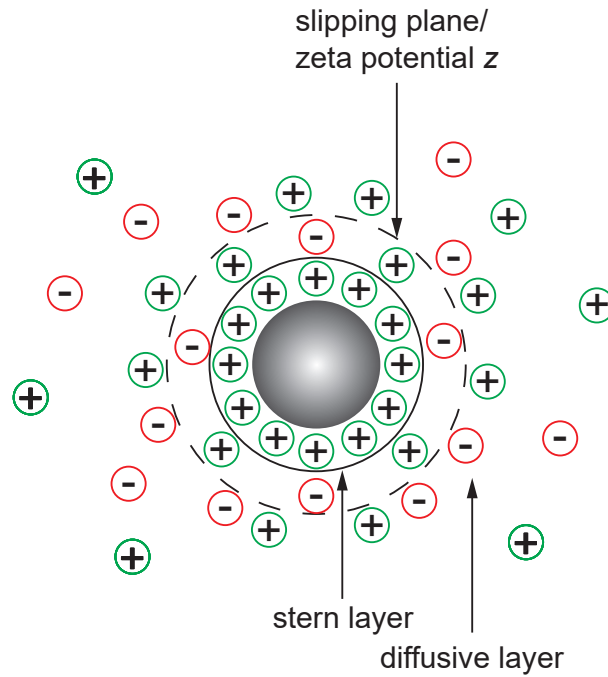
Figure 3.12. Schematic illustration of the zeta potential z. A negatively charged particle immersed in a monovalent salt solution moving under an applied electric field U_e, solid black circle indicating the stern layer, broken black line indicating the zeta potential z.

trophoretic mobility U_e, which is crucial to calculate the zeta potential z via the Henry equation which is given in equation (3.74).[106]

$$U_\mathsf{e} = \frac{2\epsilon z f(kR)}{3\eta} \qquad (3.74)$$

The dielectric constant of the medium is labeled by $\epsilon = \epsilon_0 \epsilon_r$, the viscosity of the medium by η and $f(\kappa R)$ is the Henry's function, with the particle radius R and the Debye-Hückel parameter κ, where κ^{-1} is the Debye screening length. For large particles compared to the screening length, $R >> \kappa^{-1}$, the Henry function yields $f(\kappa R) = 1.5$, giving the Helmholtz-Smoluchowski equation presented in equation (3.75).

$$U_\mathsf{e} = \frac{\epsilon z f(\kappa R)}{\eta} \qquad (3.75)$$

Equation (3.75) is valid for particles larger than R = 1 µm in electrolytes containing salt concentrations higher than 10 mM. For smaller particles $R \leq 100$ nm and low salt concentrations of 10^{-2} mM equation (3.74) is valid as $f(\kappa R) = 1.0$.[107]

3.10 Reflection interference contrast microscopy

The shape of an object on a planar surface can be investigated by label- and contact-free reflection interference contrast microscoy (RICM). Typical objects of interest are

living cells, lipid membranes or micrometer-sized spherical beads.[108][109][110][111] In this study GUVs have been observed, which consist out of lipid bilayer membranes.

Figure 3.13 shows a scheme of a typical RICM setup consisting out of a light source, a polarizer, an antiflex objective and a CCD camera. The antiflex method was first introduced by Ploem[112] to overcome stray reflection inside the microscope which obscures the signal. The stray light is eliminated by the analyzer. In this study blue light with a wavelength of $\lambda = 475$ nm gets linear polarized as indicated by the dashed line. The 63x antiflex objective has a built in $\lambda/4$-plate which yields elliptically polarized light. If the rays get refracted at interfaces with different refractive indices n the phase of the electromagnetic wave is shifted by π. After passing again through the $\lambda/4$-plate the resulting light is linearly polarized perpendicular to the incident light, which is represented by the dotted line.[113]
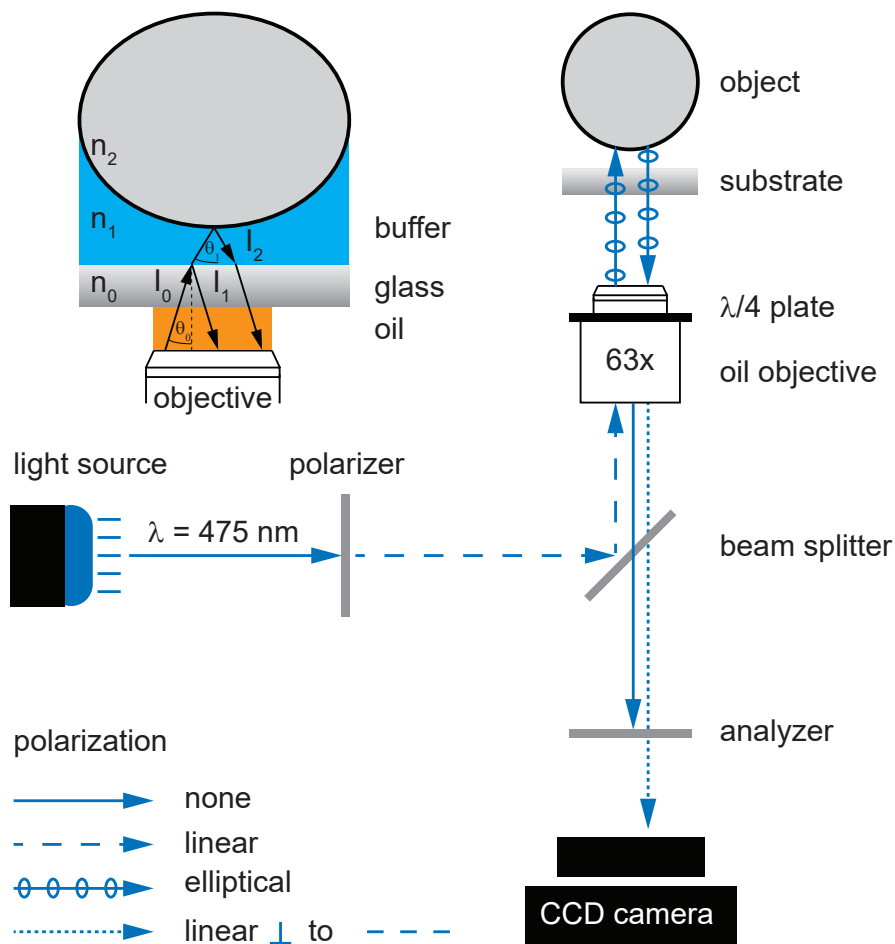
Figure 3.13. Experimental setup of RICM. Blue light with a wavelength of $\lambda = 475$ nm is linear polarized (dashed line). Passing the $\lambda/4$-plate results in elliptically polarized light. Refraction at the interfaces and passing again through the $\lambda/4$-plate yields linear polarized light perpendicular to the initial linear polarized light (dotted line).

The formation of an RICM image occurs due to interference of reflected light from the different optical interfaces with different refractive indices n. The intensity $I(x,y)$ of a

quasi-monochromatic point source for a position (x,y) can be described as the time average of the local electric field E as shown in equation (3.76) under the assumption that the layers are homogeneous and separated by parallel interfaces.[114]

$$I(x,y) = \langle E \rangle_t^2 \tag{3.76}$$

The electric field E can be written as presented in equation (3.77).

$$E(r,t) = A \exp(i(\omega t - kr)) \tag{3.77}$$

The wave vector is denoted by $k = \frac{2\pi}{\lambda}$, while r is the spatial coordinate. Assuming that only rays from a single point source can interfere, the electric field amplitudes A can be defined as shown in equation (3.78).

$$A = r_{01}A_0 + (1 - r_{01}^2)r_{12}A_0\exp(-ik\Delta_1) + ...+ = RE_0 \tag{3.78}$$

The amplitude of the incident light is denoted by A_0, the difference in optical path length by Δ_i, while r_{ij} are the Fresnel coefficients, which describe the interface between the two layers i and j. The effective reflection coefficient R is obtained by summation of the reflection coefficients r_{ij}.

If the refractive indices are known the Fresnel reflection coefficients can be expressed for waves polarized perpendicular (s) and parallel (p) to the incident plane resulting in equations (3.79) and (3.80).

$$r_{i,j}^s = \frac{n_i\cos\Theta_i - n_j\cos\Theta_j}{n_i\cos\Theta_i + n_j\cos\Theta_j} \tag{3.79}$$

$$r_{i,j}^p = \frac{n_j\cos\Theta_i - n_i\cos\Theta_j}{n_j\cos\Theta_i + n_i\cos\Theta_j} \tag{3.80}$$

In classical optics the angle Θ is defined respective to the surface normal, while in XRR the angle α is respective to the surface as described in section 3.7. Figure 3.13 shows the path of an incident ray I_0 which gets reflected and transmitted. This yields to a ray reflected from the glass/buffer interface I_1 and a transmitted ray I_2 that will be reflected at the buffer/object interface. The intensities I_1 and I_2 are defined by the reflection coefficients and depend on the incident intensity I_0 yielding equation (3.81).[113]

$$I_1 = r_{01}^2 I_0 \text{ and } I_2 = (1 - r_{01}^2)r_{12}^2 I_0 \tag{3.81}$$

Depending on the difference in optical path length the rays I_1 and I_2 interfere either in a constructive or destructive manner. Notably, the transmission coefficient t_{ij} is written as $(1 - r_{ij}^2) = t_{ij}^2$. Using the definition $I(x,y) = R * RI_0$ the effective reflection coefficient

R can be expressed as presented in equation (3.82).[114]

$$R = r_{01} + (1 - r_{01}^2)r_{12}\exp(-i2k\Delta_i))$$ (3.82)

Here, $\Delta_i = n\delta z$, where δz is the distance between the substrate and the object, yields the well known equation for the intensity $I(x, y)$ of an RICM image given in equation (3.83).[113]

$$I(\delta z) = I_1 + I_2 + 2\sqrt{I_1 I_2}\cos(2kn\delta z(x, y) + \Phi)$$ (3.83)

I_i represents the intensity of light which is reflected at the ith interface, n is the refractive index of the buffer and Φ is the phase shift. The intensity extracted from RICM images I can be converted to the relative height δz via the inverse cosine transform of equation (3.83). $I_{\mathsf{max}} = I_1 + I_2 + 2\sqrt{I_1 I_2}$ and $I_{\mathsf{min}} = I_1 + I_2 - 2\sqrt{I_1 I_2}$ correspond to the intensity maxima and minima, while the phase shift $\Phi = \pi$.

$$\delta z(t) = \arccos\left(\frac{2I(t) - (I_{\mathsf{max}} + I_{\mathsf{min}})}{(I_{\mathsf{max}} - I_{\mathsf{min}})}\right)\frac{\lambda}{4\pi n}$$ (3.84)

3.10.1 Determination of adhesion free energy

In figure 3.14a) a typical RICM snapshot of a vesicle adhering onto a pAA-Cys5 coated substrate is shown. The relative intensity profile is obtained along the azimuthal angle ϕ and plotted against the vesicle radius r as shown in figure 3.14b), where the red dotted line corresponds to the intensity maximum I_{max} corresponding to the red dotted circle in panel a). Via inverse cosine transformation the vesicle contour presented in figure 3.14c) can be obtained via equation (3.84).
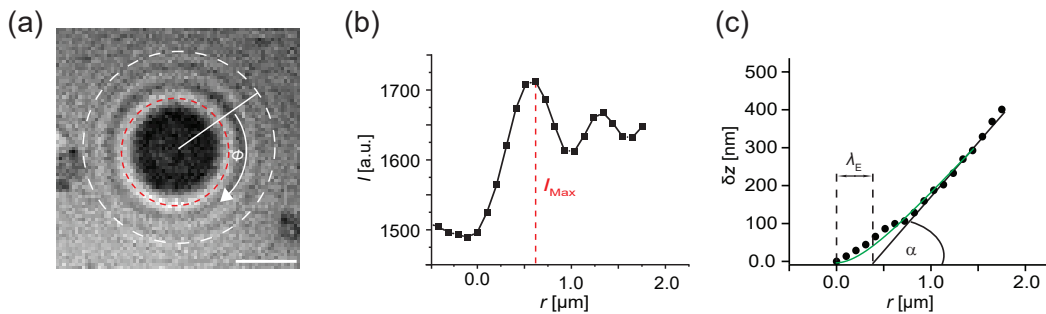
Figure 3.14. Determination of adhesion free energy $\Delta\gamma_W$ at [CdCl$_2$] = 1 mM. a) A typical RICM snapshot of a vesicle adhered on a pAA-Cys5-coated substrate. Scale bar = 2 µm. b) Relative intensity profile integrated along azimuthal angle ϕ plotted versus the distance from the center. c) Height of vesicle contour z versus the distance r, reconstructed from the relative intensity profile in figure 3.14b).

As presented in section 3.4 the adhesion free energy $\Delta\gamma_W$ can be described as shown in equation (3.85).

$$\Delta\gamma_W = \frac{1}{2}\kappa C_{1max}^2 \tag{3.85}$$

Thereby, C_{1max} is the contact curvature and κ is the bending rigidity. Under the assumption that the adhesion does not change the volume of the vesicle, the elastic energy is dominated by the contribution of the contact zone and can be expressed as presented in equation (3.85).[115][116]

$$\Delta g_{ela} = 2\pi r_A \int_0^\infty dr \left[\frac{\kappa}{2}\left(\frac{d^2z}{dr^2}\right)^2 + \frac{\sigma}{2}\left(\frac{dz}{dr}\right)^2 \right] - \int_{-\infty}^0 \Delta\gamma_W(r)dr \tag{3.86}$$

The radius of the contact zone is denoted by r_A, z is the membrane height, r the distance as shown in figure 3.14c) and σ the lateral tension. Considering a straight contact line perpendicular to r the elastic energy can be minimized resulting in equation (3.87).

$$\sigma\frac{d^2z}{dr^2} - \kappa\frac{d^4z}{dr^4} = 0 \tag{3.87}$$

For large distances r the profile $z(r)$ must be linear $z(r) = \alpha r - \alpha\lambda_E$ (see figure 3.14c)), while it must apply $r = 0$ and $z(r) = 0$. Bruinsma wrote down a solution fulfilling the boundary conditions $z = 0$, $\frac{dz}{dr} = 0$ and $\frac{d^2z}{dr^2} = \frac{\alpha}{\lambda_E} = C_{1max}$ at the edge of the adhesion zone $r = r_E$ resulting in equation (3.88).

$$z(r) = \alpha(r - r_E - \lambda_E) + \alpha\lambda_E \exp\left(-\frac{r - r_E}{\lambda_E}\right) \tag{3.88}$$

This expression was used in previous studies to analyze experimental data.[24][115][25] Within this study the vesicle contour is fitted by equation (3.88) yielding the capillary length λ_E and the angle α. In a next step, a linear fit along the vesicle contour is employed with the intersection matching λ_E at the abscissa, yielding the angle α. Thus, the curvature $C_{1max} = \frac{\alpha}{\lambda_E}$ of the vesicle at the edge of the adhesion zone is determined by implementing λ from equation (3.88) and α from the linear fit. This enables to calculate the free energy of adhesion $\Delta\gamma_W$ following equation (3.85).

3.10.2 Determination of interfacial potential

In figure 3.15a) a schematic illustration of a vesicle adhering onto pAA-Cys5 polymer coated substrates is shown with the corresponding RICM image. The height fluctuations are monitored over time by collecting the mean intensity from 3 × 3 pixels
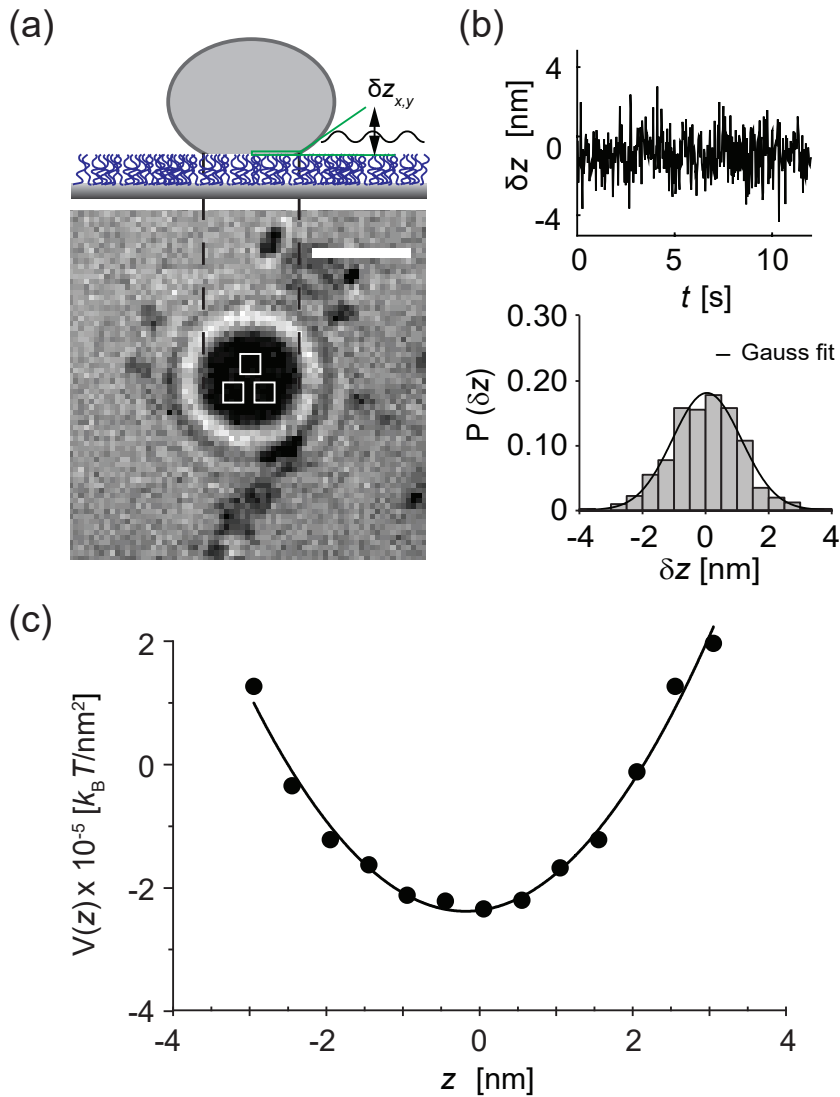
Figure 3.15. Membrane fluctuations of an adhered vesicle modulated by [CdCl$_2$]. a) From three independent locations in the adhesion zone (3 × 3 pixels, indicated by the white squares) the intensity fluctuations were converted to the heigth fluctuations (see equation (3.84)). The scale bar is 2 µm. b) Laterally averaged membrane-substrate distance δz versus time and corresponding height flucutations probability distribution $P(\delta z)$. c) Absolute interfacial potential $V(z)$ versus z. The potential curvature $V''(z{=}0)$ represents the sharpness of the membrane confinement, where the potential corresponds to $\Delta\gamma_W$, the adhesion free energy (see section 3.10.1).

indicated by the white squares in figure 3.15a) as a function of time following equation (3.84).

The analysis were performed using a self-written Matlab routine (R2019a) by Dr. Benjamin Fröhlich.[117] The selected regions of 3 × 3 pixels corresponds to 0.096 µm² and are taken from the center of the adhesion zone. Applying equation (3.84) the laterally height fluctuations $\delta z = \bar{z} - \langle z \rangle$ with $\bar{z}$ corresponding to the lateral average membrane height in a small region of 3 × 3 pixels and $\langle z \rangle = 0$ the average height over the entire

membrane patch of the macroscopic dimension L were determined. The height fluctuations $\delta z(t)$ shown in figure 3.15b) were monitored over 12 s with a time resolution of 30 ms. The obtained height fluctuations probability distribution $P(\delta z)$ can be approximated by a Gaussian distribution. The curvature around the maximum of the Gaussian distribution $V'' = \frac{d^2 V}{dz^2}$ can be well fitted by a parabolic function and corresponds to the membrane-substrate interaction from the measured variance $\langle \delta z^2 \rangle$. Considering an almost planar membrane patch $|\nabla z| \ll 1$ and using the Monge representation yields equation (3.89).

$$\mathcal{H}_0[z] = \int dx \, dy \, \left\{ V(z) + \gamma + \frac{\gamma}{2} (\nabla z)^2 + \frac{\kappa}{2} (\triangle z)^2 \right\} \tag{3.89}$$

The membrane-substrate interaction is quadratically expanded around its minimum with aid of a Taylor series expansion at z=0 yielding equation (3.90).

$$V(z) = -\Delta \gamma_{\mathsf{W}} + \frac{1}{2} V'' z^2 \tag{3.90}$$

Under the assumption that the membrane tension is negligible ($\gamma \approx 0$) equation (3.91) is obtained.

$$\frac{\mathcal{H}_0[\tilde{z}]}{L^2} = -\Delta \gamma_w + \frac{1}{2} V'' \tilde{z}_0^2 + \frac{1}{2} \sum_{q \neq 0} \left(V'' + \kappa q^4 \right) |\tilde{z}_q|^2 \tag{3.91}$$

$\tilde{z}_q$ is the two-dimensional Fourier transform of $z(x,y)$ and L is the length of a membrane patch. Under equilibrium, the Fourier modes are Gaussian distributed with zero mean and the variance following equation (3.92).[51]

$$\langle \tilde{z}_q \tilde{z}_{q'} \rangle = \frac{k_{\mathrm{B}} T}{L^2 (V'' + \kappa q^4)} \delta_{q,-q'} \tag{3.92}$$

On short-length scales the fluctuation spectrum is dominated by the bending rigidity κ, whereas the curvature of the membrane-substrate potential dictates the fluctuation of the physically coupled membrane on large scales. The parallel correlation length, $\xi_\parallel = \sqrt[4]{\kappa/V''}$ represents the crossover of these two length scales. The pixel size determines the resolution of microscopy. In case of the 63x oil immersion objective used in this study the pixel size is 103 nm. In this manner the membrane fluctuation is laterally averaged over a scale $\Delta_{3p} \gg \xi_\parallel$ resulting in equation (3.93).

$$\delta z = \frac{1}{\Delta_{3p}^2} \int_{\Delta_{3p}^2} dx \, dy \, z(x,y) = \sum_{q \neq 0} \tilde{z}_q \frac{2\mathsf{sin}(\frac{q_x \Delta_{3p}}{2})}{q_x \Delta_{3p}} \frac{2\mathsf{sin}(\frac{q_y \Delta_{3p}}{2})}{q_y \Delta_{3p}} \tag{3.93}$$

Using equations (3.92) and (3.93) $\langle \delta z^2 \rangle$ can be calculated as presented in equation (3.94).

$$\langle \delta z^2 \rangle = \frac{k_B T}{V''(2\Delta_{3p})^2} \tag{3.94}$$

Thereby the curvature of the membrane-substrate interaction, V'', near the average height of an adhered membrane patch was estimated. The variance of the height fluctuations from figure 3.15b was extracted and enables calculating the curvature of the membrane substrate interaction at the potential minimum, $V'' = k_B T / [\langle \delta z^2 \rangle (2\Delta_{3p})^2]$ shown in figure 3.15c), which corresponds to the "spring constant" of a harmonic oscillator.[51]

4   Static wetting of bio-inspired stimulus responsive polymer brushes by giant lipid vesicles

In the last decades the interest of cell adhesion to biological- and inorganic materials increased tremendously.[118][74][119] In section 4 the interaction between giant unilamellar vesicles (GUVs) and bio-inspired pAA-Cys5 polymer brushes is investigated. In section 4.1 the bio-inspired polymer is introduced, which is characterized in section 4.2 by X-ray reflectivity (XRR) measurements and in section 4.3 by zeta potential measurements. Next, the wetting by giant unilamellar vesicles (GUVs) is demonstrated qualitatively in section 4.4 and then quantified in sections 4.5 and 4.6.

4.1   Bio-inspired pAA-Cys5 polymer brushes

Several studies demonstrated that Cadmium ions (Cd^{2+}) are toxic for plants. Shah *et al.*[120] found that Cd^{2+} exposure altered the ribonucleic acid (RNA) activity, while Woolhouse *et al.*[121] showed that Cd^{2+} intake is lowering the rate of photosynthesis. Nevertheless, if plants get exposed to heavy metal ions such as Cd^{2+} they express phytochelatins, which are able to chelate heavy metal ions and thereby help the plant to detoxify itself. Phytochelatins consist out of glutathione oligomers, while glutathione consists out of a sequence of γ-glutamin, cysteine and glycine giving the following sequence: $(\gamma\text{-Glu-Cys})_n$Gly.[122] The affinity between phytochelatin and Cd^{2+} is very high which can be quantified by a dissociation constant of $K_D \approx 10^{-16}$ M.[123] Natural phytochelatins and metallothionein proteins posess both -SH (orange) and -COOH (green) side chain moieties as indicated in figure 4.1.[124][125]
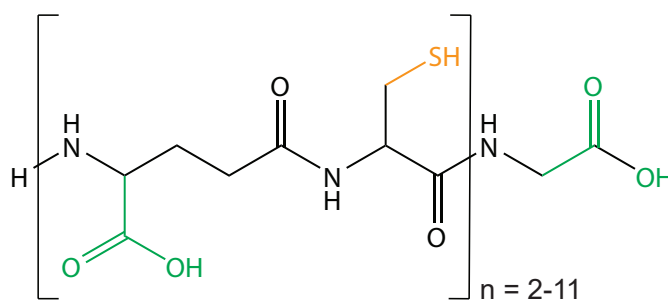
Figure 4.1. Molecular structure of phytochelatines consisting of γ-glutamin, cysteine and glycine. The carboxy moieties are represented in green, while the thiol moieties are represented in orange.

Based on this concept the artificial pAA-Cys5 polymer was developed consisting out of a poly acrylic acid backbone and 5 % cysteine side chains. The molecular structure of pAA-Cys5 is shown in figure 4.2. Analogous to the natural phytochelatin shown in

figure 4.1 the artifical pAA-Cys5 polymer contains -COOH (green) and -SH (orange) moieties, which might be important for the capturing of Cd^{2+} as Jalilehvand[123] reported a tetrathiolate Cd(II) N-acetylcysteine complex. To couple pAA-Cys5 to neutravidin a biotin moiety was introduced (blue). The pAA-Cys5 polymer was synthesized and kindly provided by Dr. Masaki Nakahata (Osaka university). Indeed, in a recent study including pAA-Cys5 it was found that the coexistence of -COOH and -SH side chains is necessary to achieve sensitive Cd^{2+} capturing.[35]
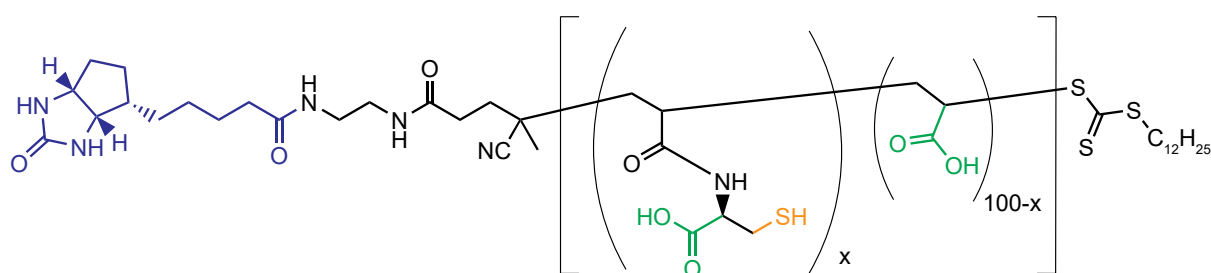
Figure 4.2. Molecular structure of pAA-Cys5. The carboxy moieties are represented in green, while the thiol moieties are represented in orange.

4.2 Structural changes of pAA-Cys5 polymer brushes induced by Cd^{2+} monitored by X-ray reflectivity measurements

To investigate whether the incorporation of Cd^{2+} into pAA-Cys5 alters its structure, high energy X-ray reflectivity (XRR) measurements were carried out following the protocol described in section 2.2.7. pAA-Cys5 polymer brushes were grafted onto a DOPC membrane containing 2 mol% DOPE-biotin via neutravidin crosslinkers. This method enables a defined grafting distance $\langle d \rangle$ between the polymer brushes, which can be controlled with nm accuracy by varying the fraction of DOPE-biotin χ_{biotin}. Assuming an area per lipid molecule of 0.6 nm² the distance between DOPE-biotin can be controlled following equation (4.1).[126]

$$\langle d \rangle = \sqrt{\frac{0.6 \text{ nm}^2}{\chi_{\text{biotin}}}} \qquad (4.1)$$

The experimental system was build up step wise while each preparation step was verified by XRR measurements. As a prerequisite the bilayer and the successive coupled neutravidin to the bilayer need to be analyzed to be able to monitor the changes in the sample structure due to the addition of pAA-Cys5 in the absence and presence of Cd^{2+}. Figure 4.3 shows Rq^4 plotted versus q_z obtained from XRR measurements of a DOPC bilayer containing 2 mol% of DOPE-biotin. The black line represents the best fit results according to χ^2 minimization corresponding to a 5 layer slab model: outer head
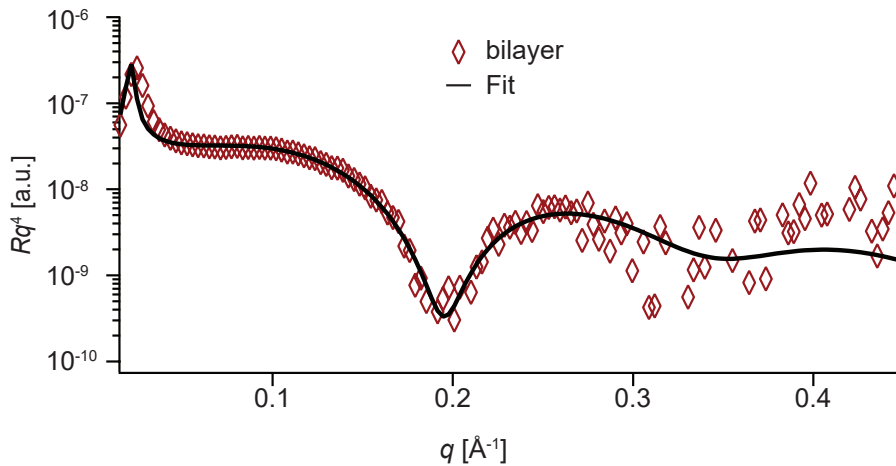
Figure 4.3. Rq^4 plotted versus q_z obtained from XRR measurements of a lipid bilayer containing DOPC doped with 2 mol% DOPE-biotin. Black line represents the best fit results.

group, alkyl chains, inner head group, water layer and Si-oxide layer. The parameters thickness d, scattering length density SLD and roughness σ obtained from the best fit results are presented in table 4.1. The total thickness of the membrane d_{tot} = 3.8 nm is in good agreement with previous studies, e.g. Miller *et al.*[127] found for a pure DOPC membrane a total thickness of d_{tot} = 4.1 nm, while Fragneto *et al.* obtained d_{tot} = 3.9 nm for each DOPC layer of a multilayer system.[128] The SLD values obtained from the best fit results are in good agreement with the numbers obtained from Miller *et al.*[127] Also the thin layer of buffer between the substrate and the lipid head group is consistent with previously reported data ($d_{buffer} \approx 0.4$ nm).[127][129][130] The SLD of the inner lipid headgroup SLD_{iH} = $(13.1 \pm 0.7) \times 10^{-6}$ Å^{-2} is higher compared to the SLD of the outer lipid head group SLD_{oH} = $(11.3 \pm 0.2) \times 10^{-6}$ Å^{-2}. This indicates a lower water content in the inner head group compared to the outer one, which is in agreement with previous studies.[131][132] The thickness of the inner head group (d_{ih} = 0.74 ± 0.04 nm) is smaller compared to the thickness of the outer one (d_{oh} = 0.97 ± 0.06 nm), indicating interactions of the inner leaflet of the bilayer with the substrate as reported previously.[133]

The bilayer was incubated for 4 h at room temperature with a neutravidin solution having a final concentration of 40 µg/ml. The binding strength between DOPE-biotin and neutravidin is comparable to a covalent bond as described in section 2.2.1. To confirm the successful binding of neutravidin onto the bilayer fluorescence imaging of Texas Red-labeled neutravidin was employed. A schematic illustration showing the binding of neutravidin onto biotinylated lipids (DOPE-biotin) is presented in figure 4.4a), where the average grafting distance $\langle d \rangle$ corresponds to 5.5 nm for a molar fraction of 2 mol% of biotinylated lipids according to equation (4.1). Figure 4.4b) shows a typical corresponding fluorescence microscopy image indicating homogeneous coating of the bilayer by neutravidin after 4 h of incubation. The incubation time was varied between 2 to 8 h
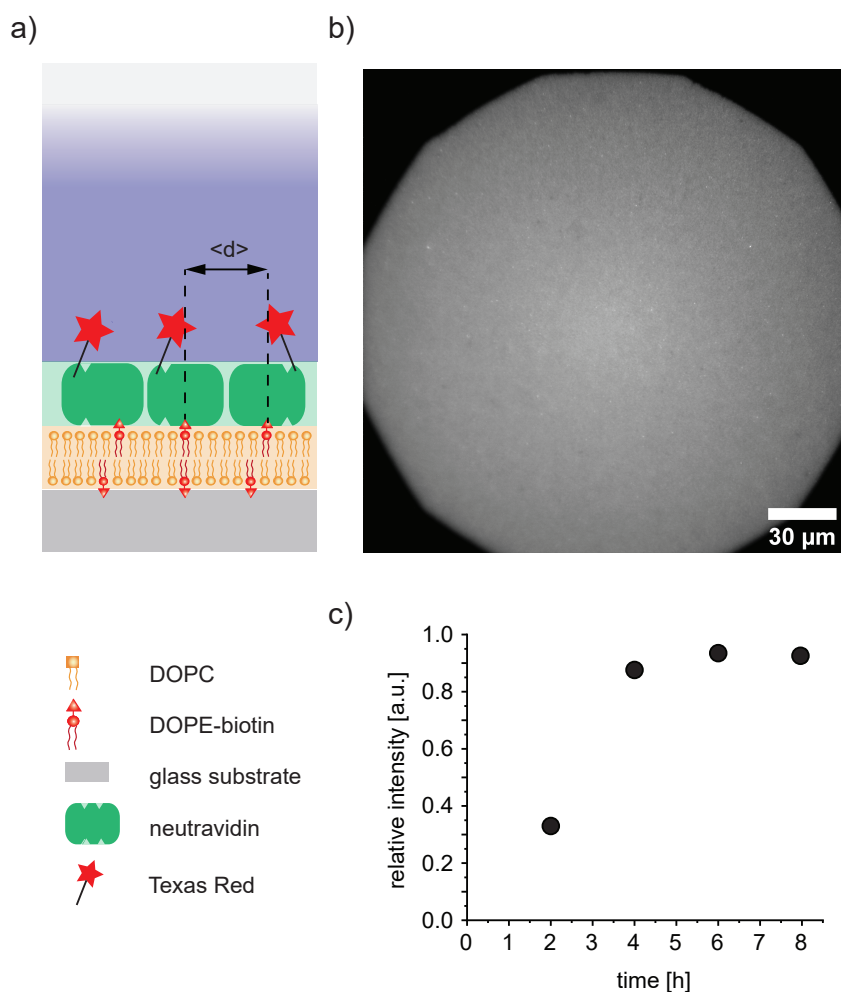
Figure 4.4. Fluorescence imaging of neutravidin labeled with Texas Red. a) Schematic illustration of Texas-Red labeled neutravidin coupled to biotinylated lipids. b) Corresponding fluorescence image. c) Relative fluorescence intensity plotted versus time.

with a temporal distance of 2 h, showing a saturated relative fluorescence intensity signal after 4 h, with no further increase, confirming 4 h of incubation time to be sufficient for the XRR experiments. The Rq^4 plotted versus q_z data for neutravidin added to the bilayer show a distinctive difference in the global shape of the XRR curve, indicating that the coupling of neutravidin was successful as demonstrated in figure 4.5. To fit the data properly, the structural parameters for the bilayer presented in table 4.1 were constrained to around $\pm$ 10 %, despite the parameters for the outer lipid head group to enable significant changes due to the coupling of neutravidin. The fit (black line) following a 6 layer slab model with neutravidin as an additional slab on top yields a thickness for neutravidin of $d_{\text{neutravidin}}$ = 4.26 nm which is reasonable as neutravidin in dry state was determined to be 4.0 nm.[134] Also Abuillan and Burk got similar results for neutravidin in solution obtaining thicknesses of 4.78 nm and 4.35 nm.[135][132]

The sample was incubated with the pAA-Cys5 polymer with a final concentration of
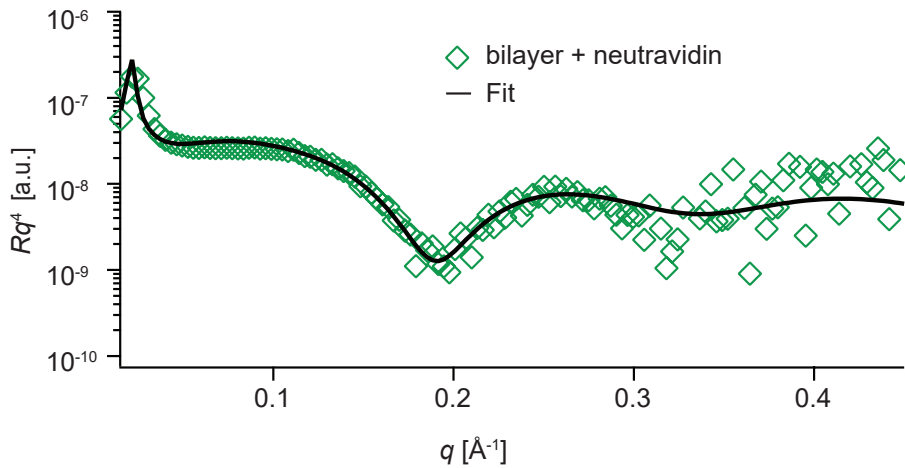
Figure 4.5. Rq^4 plotted versus q_z obtained from XRR measurements of neutravidin coupled to the lipid bilayer from figure 4.3. Black line represents the best fit results.

Table 4.1. Layer parameters of bilayer corresponding to the best fit results of high energy specular X-ray reflectivity data (black solid lines).

	bilayer		
	d	SLD	σ
	[nm]	[10^{-6}Å^{-2}]	[nm]
SiO$_2$	1.10 ± 0.06	18.9	0.37 ± 0.06
buffer	0.52 ± 0.02	9.45	0.41 ± 0.05
lipid headgroup$_{inner}$	0.75 ± 0.04	13.1 ± 0.7	0.44 ± 0.09
lipid alkyl chain	2.07 ± 0.07	6.2 ± 0.3	0.60 ± 0.65
lipid headgroup$_{outer}$	0.97 ± 0.06	11.3 ± 0.2	0.56 ± 0.16

	bilayer + neutravidin		
	d	SLD	σ
	[nm]	[10^{-6}Å^{-2}]	[nm]
SiO$_2$	1.10 ± 0.04	18.9	0.40 ± 0.02
buffer	0.53 ± 0.02	9.45	0.38 ± 0.04
lipid headgroup$_{inner}$	0.76 ± 0.03	13.8 ± 0.1	0.44 ± 0.05
lipid alkyl chain	1.99 ± 0.02	6.6 ± 0.01	0.57 ± 0.03
lipid headgroup$_{outer}$	0.79 ± 0.06	12.7 ± 0.2	0.57 ± 0.04
neutravidin	4.26 ± 0.43	10.0 ± 0.01	1.19 ± 0.17

40 µg/ml overnight at room temperature and was coupled to neutravidin via the biotin moiety (see figure 4.2). The global shape of Rq^4 plotted versus q_z shows a distinct shift to lower q values which indicates an increase in thickness following $q_{minimum} \approx \frac{2\pi}{d}$ respectively the binding of pAA-Cys5 to the system as shown in figure 4.6. Hydrated polymers are well known to have an SLD very close to buffer which makes analysis difficult due to a lack of contrast (see section 3.7) between the polymer and the buffer. That
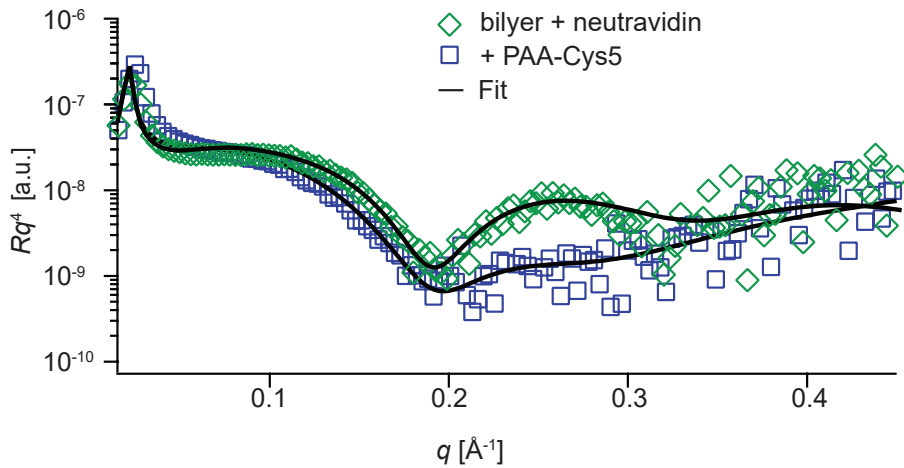
Figure 4.6. Rq^4 plotted versus q_z obtained from XRR measurements of the bilayer + neutravidin shown in figure 4.5 overlayed with the addition of pAA-Cys5. The black line represents the best fit results.
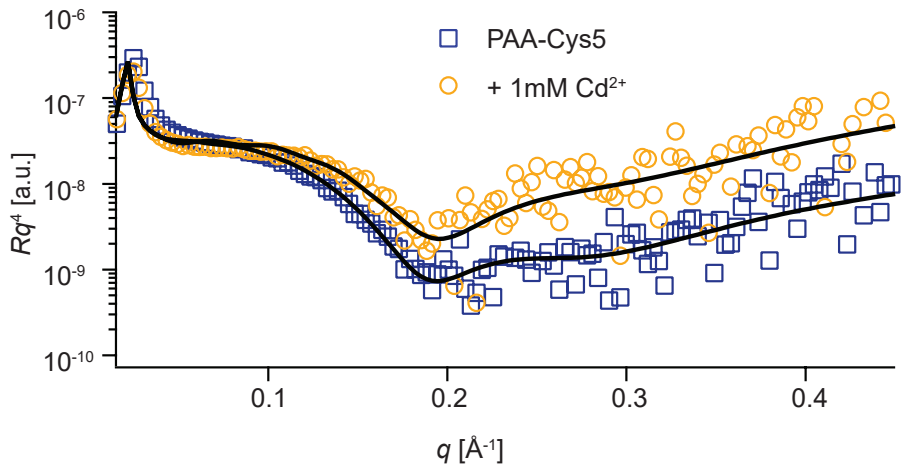
Figure 4.7. Rq^4 plotted versus q_z obtained from XRR measurements of pAA-Cys5 before and after the addition of 1 mM Cd^{2+}. The black line represents the best fit results.

is why neutravidin and pAA-Cys5 are fitted as one slab which leads to a 6 layer slab model in total. The best fit results (black line) are presented in table 4.2. The thickness of pAA-Cys5 yields a thickness of $d_{pAA-Cys5} = 13.9 \pm 0.8$ nm. In figure 4.7 an overlay of Rq^4 plotted versus q_z obtained from XRR measurements of pAA-Cys5 in the absence and presence of $[Cd^{2+}] = 1$ mM is presented. The XRR curves show a distinctive difference in their global shapes as the minimum $q_{minimum}$ in the presence of $[Cd^{2+}] = 1$ mM is shifted to higher q_z values indicating a decrease in thickness. Indeed, fitting of the data shows that the addition of $[Cd^{2+}] = 1.0$ mM results in a decrease in thickness yielding $d_{pAA-Cys5+Cd^{2+}} = 9.9 \pm 1.2$ nm, showing a compaction of 4 nm. The surface roughness σ of the brush/buffer interface decreases from $\sigma_{pAA-Cys5} = 2.1$ nm to $\sigma_{pAA-Cys5+Cd^{2+}} = 1.2$ nm. This indicates a compaction of the brushes in the presence of $[Cd^{2+}] = 1.0$ mM yielding a sharper transition between brush and buffer interface, indicating that the negative

charges of the -COOH side chains were compensated by the Cd^{2+} binding. This is supported by an increase of the SLD between the brushes in the absence and in the presence of $[Cd^{2+}]$ = 1.0 mM yielding $SLD_{pAA-Cys5}$ = $(9.7 \pm 0.1) \times 10^{-6}$ Å^{-2} respectively $SLD_{pAA-Cys5+Cd}$ = $(9.9 \pm 0.1) \times 10^{-6}$. The experiments are performed in 100 mM NaCl resulting in a Debeye screening length of $\kappa_D^{-1} \approx 1$ nm and buffered with 10 mM Tris adjusted to a pH of 7.4. Therefore the addition of 1 mM Cd^{2+} does not alter the Debeye screening length nor the pH value.

Table 4.2. Layer parameters of pAA-Cys5 corresponding to the best fit results of high energy specular X-ray reflectivity data (black solid lines).

pAA-Cys5-biotin in the absence of Cd^{2+}			
	d [nm]	SLD [10^{-6}Å^{-2}]	σ [nm]
SiO_2	1.23 ± 0.03	18.9	0.55 ± 0.01
buffer	0.46 ± 0.01	9.45	0.45 ± 0.02
lipid headgroup$_{inner}$	0.68 ± 0.01	13.1 ± 0.2	0.47 ± 0.01
lipid alkylchain	2.24 ± 0.03	6.8 ± 0.01	0.59 ± 0.02
lipid headgroup$_{outer}$	0.89 ± 0.05	12.3 ± 0.2	0.62 ± 0.06
neutravidin + pAA-Cys5	18.2 ± 0.8	9.7 ± 0.1	2.05 ± 0.1
pAA-Cys5-biotin in the presence of 1mM Cd^{2+}			
	d [nm]	SLD [10^{-6}Å^{-2}]	σ [nm]
SiO_2	1.19 ± 0.04	18.9	0.51 ± 0.01
buffer	0.48 ± 0.01	9.45	0.44 ± 0.03
lipid headgroup$_{inner}$	0.67 ± 0.02	12.9 ± 0.3	0.44 ± 0.03
lipid alkylchain	2.21 ± 0.04	7.1 ± 0.02	0.59 ± 0.03
lipid headgroup$_{outer}$	0.88 ± 0.07	12.3 ± 0.4	0.57 ± 0.06
neutravidin + pAA-Cys5	14.2 ± 1.2	9.9 ± 0.1	1.20 ± 0.11

Based on the obtained fitting parameters presented in table 4.1 and 4.2 a detailed schematic illustration of the layer fine structure is presented in figure 4.8. In 4.8a) the bilayer on a silicon substrate is shown with the corresponding SLD profile represented by the red line. In figure 4.8b) the addition of neutravidin to the corresponding bilayer is shown, where the green line represents the SLD profile. In figure 4.8c) and 4.8d) the addition of the bio-inspired, stimulus responsive pAA-Cys5 polymer is illustrated in the absence and presence of $[Cd^{2+}]$ = 1.0 mM showing a clear compaction in the presence of $[Cd^{2+}]$ = 1.0 mM. An overlay of the corresponding SLD profiles is shown in figure 4.8e) showing the transition from the pAA-Cys5 polymer into the buffer in the inset, clearly showing a sharper transition in the presence of $[Cd^{2+}]$ = 1.0 mM.
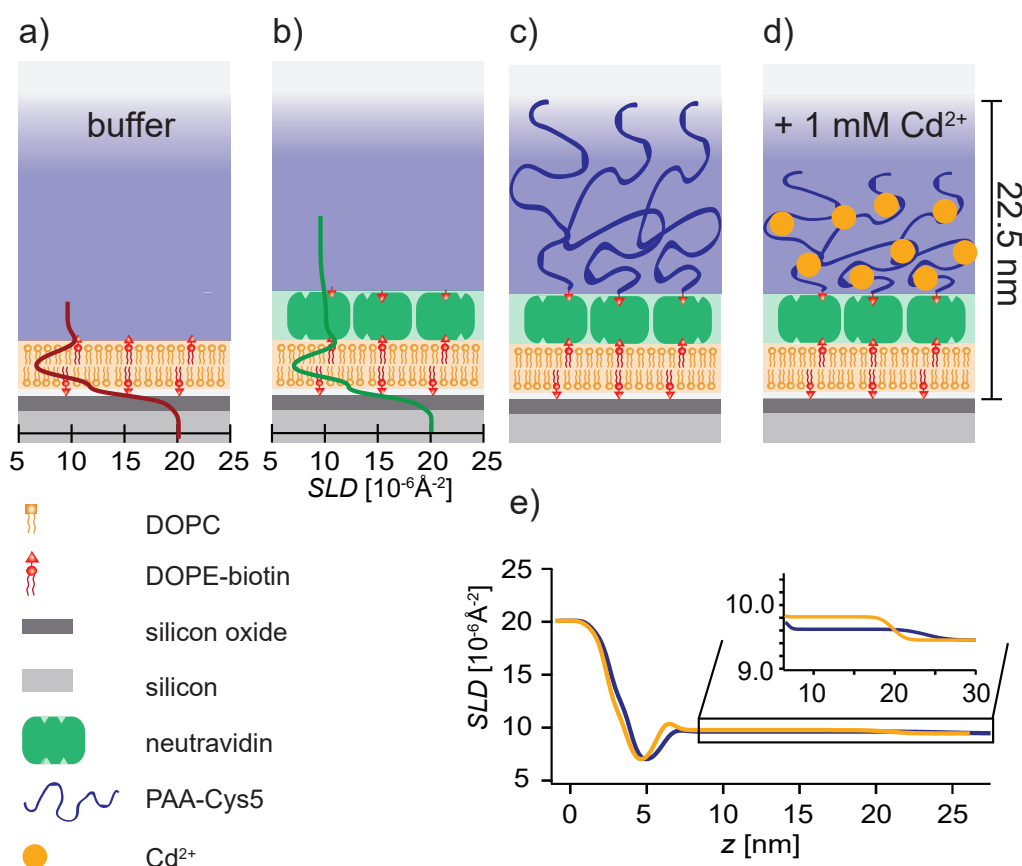
Figure 4.8. Fine structure of each preparation step according to XRR analysis. a) DOPC bilayer containing 2 mol% DOPE-biotin. Red line represents the SLD. b) Coupling of neutravidin via DOPE-biotin. Green line represents SLD profile. c) Coupling of pAA-Cys5 due to neutravidin-biotin interaction. d) Addition of 1 mM Cd^{2+} induces compaction of pAA-Cys5. e) Overlay of SLD profiles of c) and d).

4.3 Incorporation of divalent cations into pAA-Cys5 probed by zeta potential measurements

The XRR data presented in section 4.2 show a clear compaction of pAA-Cys5 due to the addition of 1 mM Cd^{2+}. To further investigate if the incorporation of divalent cations such as Cd^{2+} and Ca^{2+} compensate the negative charges located in the -COOH side chains of pAA-Cys5, zeta potential z measurements were carried out. Therefore, a bilayer containing 2 mol% DOPE-biotin was deposited onto Si-beads (d = 3 μm) via vesicle fusion. pAA-Cys5 was coupled to the bilayer via using neutravidin as a crosslinker as shown in figure 4.9a) and further explained in section 4.2. Zeta potential measurements were carried out in a 10 mM Tris buffer adjusted to a pH of 7.4. In figure 4.9b) the zeta potential z is plotted as a function of the Cd^{2+} (orange) and Ca^{2+} (black) concentration.

In both cases there is an monotonic increase in z indicating that the ions get incorporated into the pAA-Cys5 brushes compensating the negative charges of the -COOH
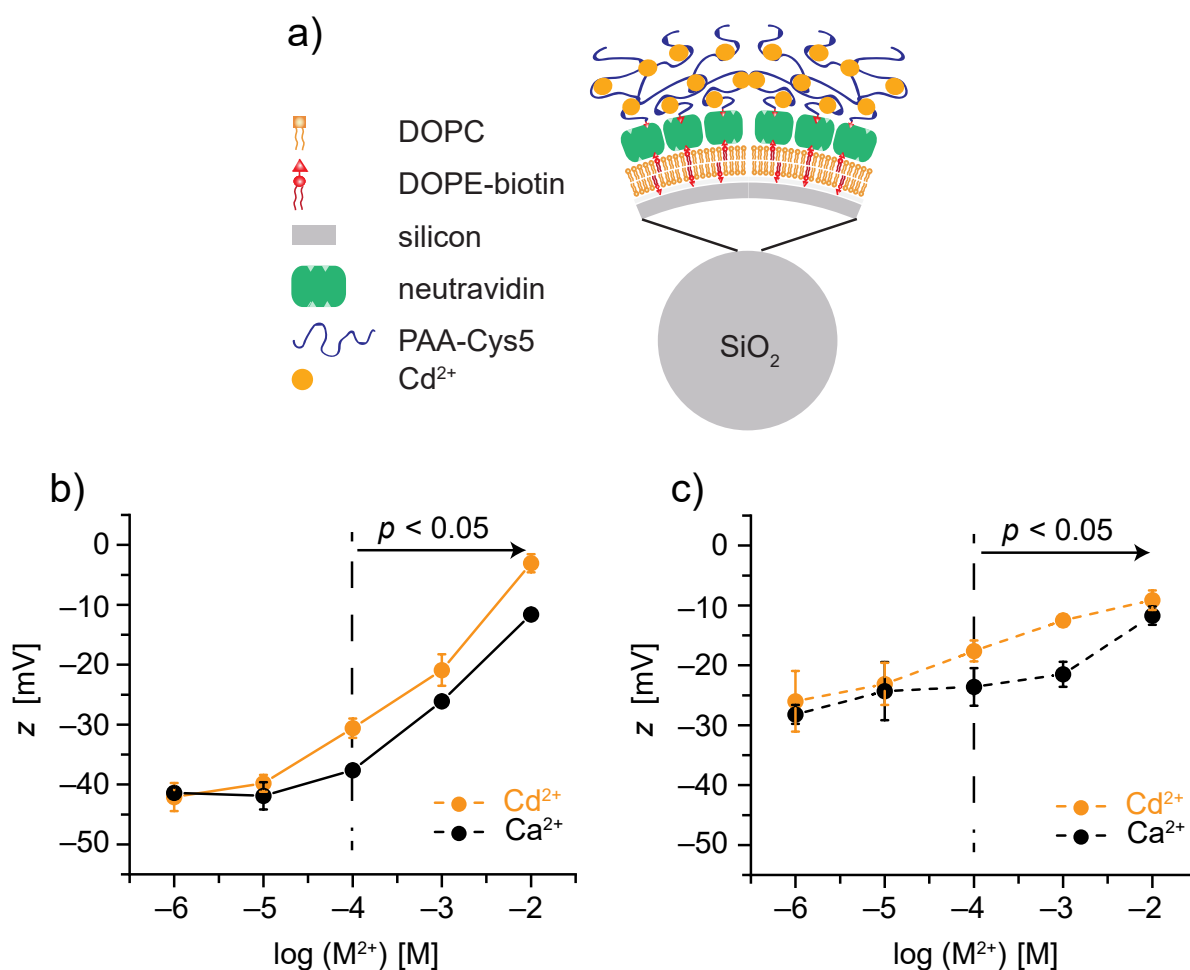
Figure 4.9. Scheme of a Si-bead (d = 3 µm) coated with pAA-Cys5 (a). Corresponding zeta potential z measurements at various Cd^{2+} (orange) and Ca^{2+} (black) concentrations in the absence (b) and in presence of 100 mM NaCl (c).

groups located in the side chains. From concentrations of $[M^{2+}]$ = 0.1 mM z in the presence of Cd^{2+} (orange) is significantly higher compared to Ca^{2+} (black). This indicates that the dissociation constant between pAA-Cys5 and Cd^{2+} is higher than for Ca^{2+}. In fact, Tanaka *et al.*[34] found that the dissociation constant between Cd^{2+} and pAA-Cys5 is around 4 orders of magnitude lower compared to Ca^{2+}, demonstrating a significantly higher affinity between Cd^{2+} and pAA-Cys5 compard to Ca^{2+}. This is in good agreement with the obtained zeta potential results. In figure 4.9c) 100 mM NaCl is added to the 10 mM Tris buffer solution. Also in the presence of 100 mM NaCl there is an monotonic increase of z with increasing $[M^{2+}]$, but the increase is remarkably lower compared to the sample in the absence of 100 mM NaCl. This is an understandable result as the electrostatic interactions get screened by it leading to a Debye screening length of $\kappa_D^{-1} \approx 1$ nm.

4.4   Wetting of pAA-Cys5 by giant unilamellar vesicles

Next the wettability of pAA-Cys5 coated substrates by giant unilamellar vesicles (GUVs) containing DOPC as a matrix lipid and 0.2 mol% Texas-Red labeled lipids is investigated. Figure 4.10a shows a scheme of a "non-wetting" vesicle hovering on the brush-coated substrate, while the vesicle in 4.10b established a stable adhesion contact to the surface ("wetting vesicle"). To discriminate whether the vesicles established contact to the surface reflection interference contrast microscoy (RICM) imaging at $[Cd^{2+}] = 0$ mM, 0.25 mM and 1.0 mM was carried out as presented in figure 4.10c-e. In figures 4.10f-h) the global shapes of vesicles of comparable size are visualized showing the confocal side view from the middle plane obtained du to the 3D reconstruction of confocal bottom view images as shown in section 3.6. The solution inside the vesicle was adjusted to be slightly higher in density than the outer solution ($\Delta\rho = 40$ kgm^{-3}) so that the vesicle sediments to the substrate. The RICM image in figure 4.10c shows a bright disc with a shallow dark spot, changing its size and intensity over time, in its center. This indicates that the vesicle does not adhere to the surface, but sediments due to the difference in density between the inner and outer medium (see above). This result is in good agreement with the confocal side view of a vesicle in the absence of Cd^{2+} showing no indication of wetting. The RICM image of a vesicle in the presence of $[Cd^{2+}] = 0.25$ mM shows a dark disk in the center due to destructive interference, suggesting that the vesicle adheres to the brush coated substrate (see 4.10d). In comparison from the confocal side view image in figure (4.10g) a flat vesicle-substrate contact can be detected hardly. The RICM image of a representative vesicle in 4.10e in the presence of $[Cd^{2+}] = 1.0$ mM shows a more prominent dark disc, indicating an even stronger adhesion compared to the vesicle in the presence of $[Cd^{2+}] = 0.25$ mM. Also the confocal side view image is showing a clear flattening of the contact between the vesicle and the brush substrate at the bottom. Thus, the adhesion contact can be detected only at $[Cd^{2+}] \geq 0.25$ mM.

To support the obtained results, in figure 4.11a) a vesicle in the absence of Cd^{2+} is monitored over 150 ms showing a bright disk with a faint dark spot in the center at $t = 0$ ms, changing its size and intensity over time resulting in a dynamically changing of size and intensity of the adhesion area, suggesting that the vesicle sedimented but did not adhere onto the surface. For vesicles at $[Cd^{2+}] \geq 0.25$ mM the interference patterns did not change over time, indicating an established adhesion contact of the vesicle to the brush coated substrate as shown in figure 4.11b-c).

In addition, more data sets of confocal side view images and RICM images are presented in figure 4.12. In the absence and presence of $[Cd^{2+}] \leq 0.1$ mM there is no stable vesicle-substrate contact detectable as indicated in figure 4.12a-b). At $[Cd^{2+}] \geq 0.25$ mM a stable contact could have been established, verifying the onset of wetting starting
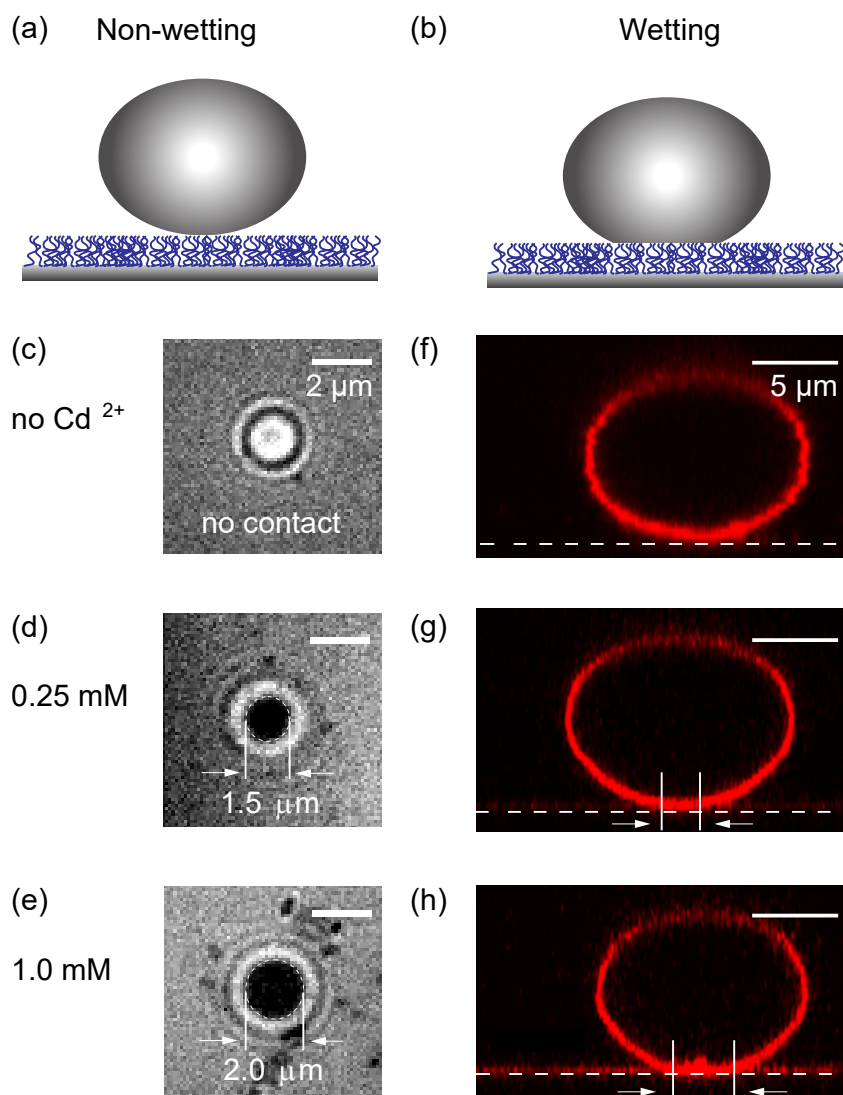
Figure 4.10. [Cd^{2+}] dependent wetting of pAA-Cys5 by DOPC GUVs (d = 10 µm). Scheme of a non-wetting (a) and wetting vesicle (b). RICM images (c-e) and side view images obtained from the 3D reconstruction of confocal microscopy bottom view images (f-h) under [Cd^{2+} = 0 mM, 0.25 mM and 1.0 mM], where the onset of wetting was observed at [Cd^{2+}] $\geq$ 0.25 mM, indicated due to the formation of a stable interference pattern showing a dark disk in the center.

from [Cd^{2+}] $\geq$ 0.25 mM as demonstrated by the confocal side view images presented in figures 4.12c-e) and the RICM images depicted in figures 4.12c) and e).

To verify that the different wettability can be accounted to the change in the brush conformation and is not an effect of a decrease in bending rigidity 1,2-dioleoyl-sn-glycero-3-phosphocholine (DOPC) GUVs were monitored on a pure DOPC bilayer. In figure 4.13a) the vesicles show no vesicle-substrate contact in the absence of Cd^{2+}, while at [Cd^{2+}] = 1.0 mM they show no contact as well similar to the sample in the absence of Cd^{2+} as shown in 4.13b), indicating that the compaction of pAA-Cys5 brushes causes the different wetting behaviors.
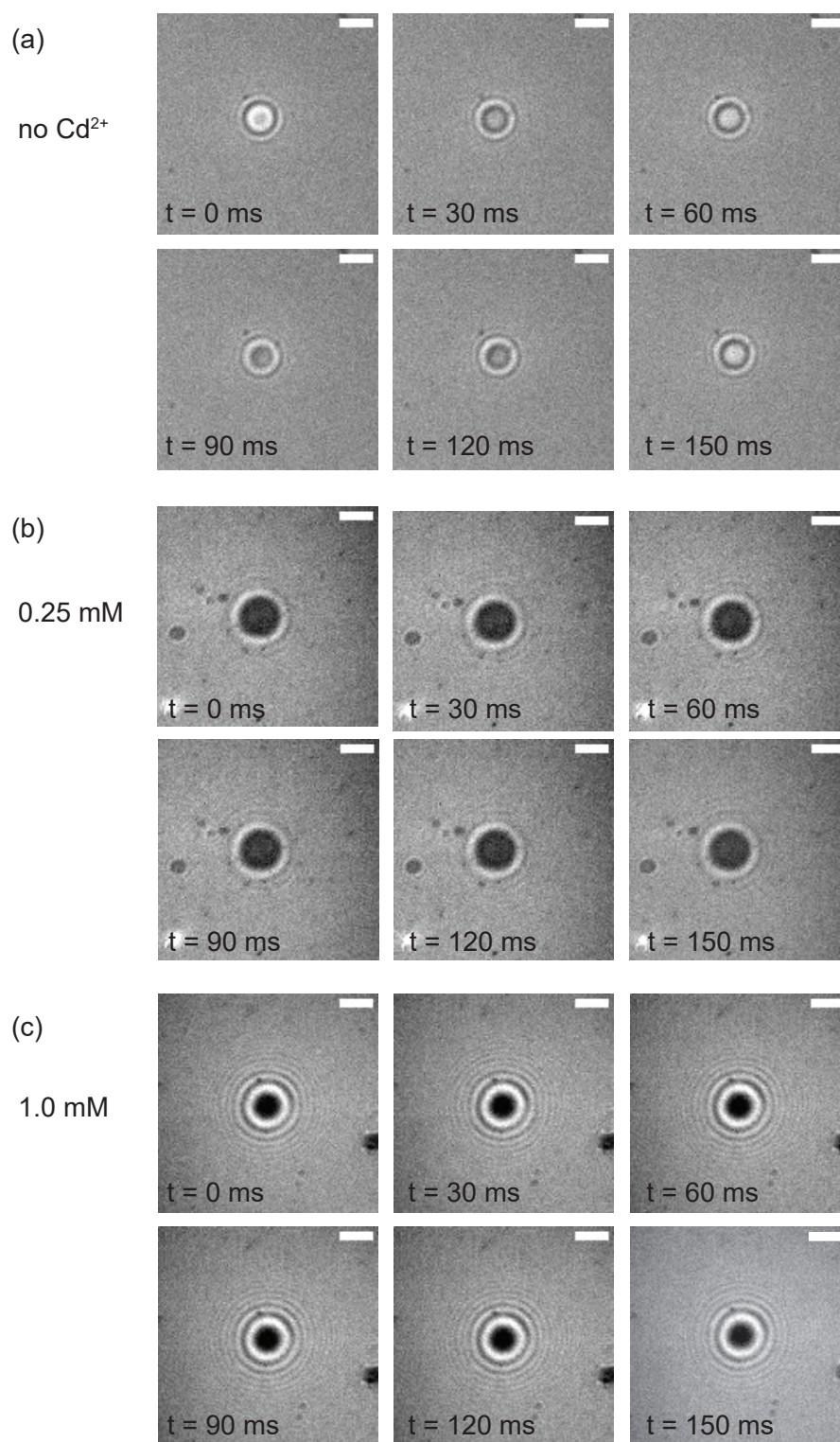
Figure 4.11. RICM images of GUVs on pAA-Cys5 with 30 ms in between frames. In the center of the vesicle, the intensity fluctuates in the absence of Cd^{2+} (a), while the interference pattern did not show detectable changes over time for $[Cd^{2+}] \geq 0.25$ mM. (b-c). The scale bar is 2 μm.

In previous studies GUVs doped with cationic lipids deposited on supported membranes doped with negatively charged lipids, caused a change in surface charge dens-
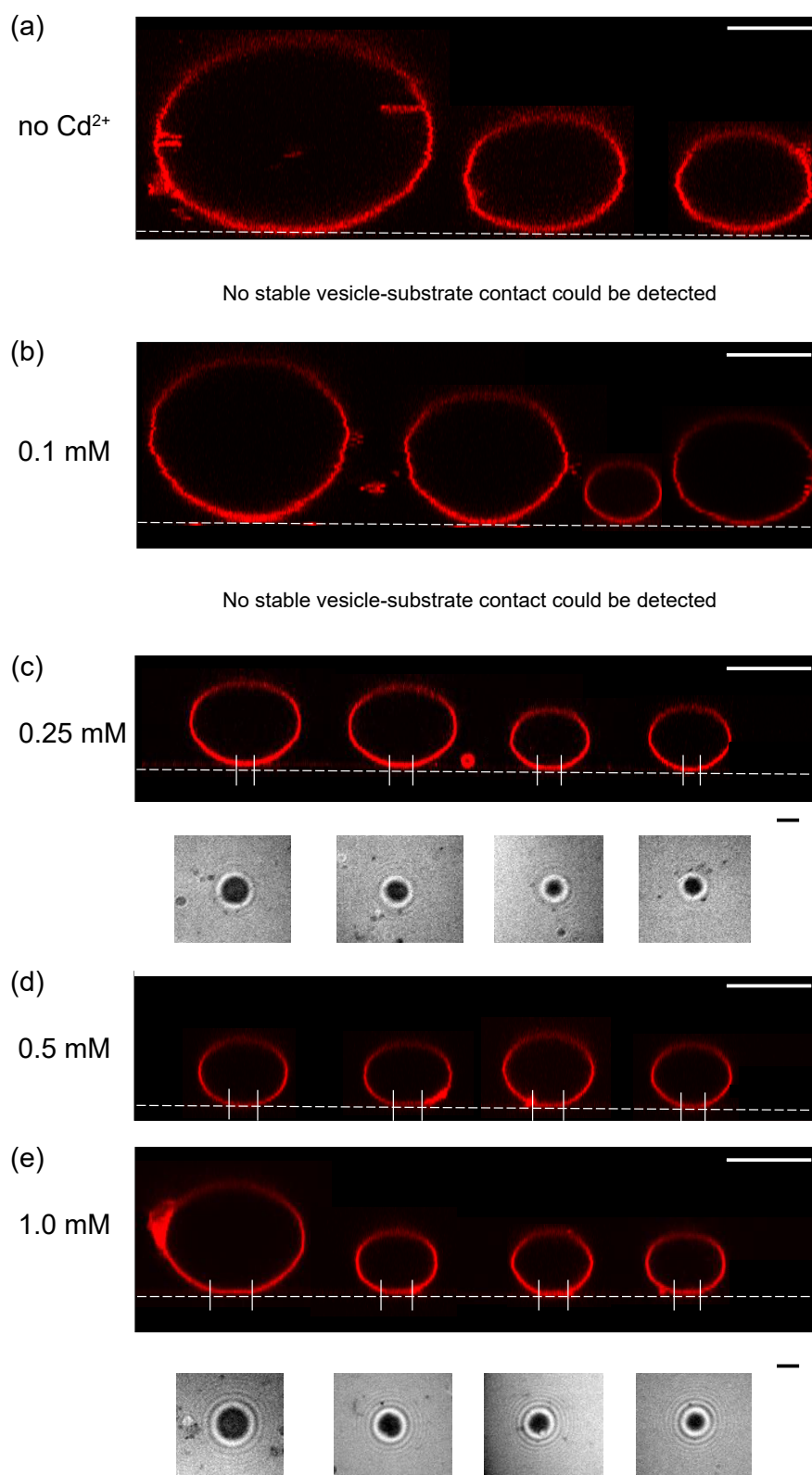
Figure 4.12. Confocal side views of DOPC GUVs showing no adhesion at $[Cd^{2+}] \leq 0.1$ mM (a-b), while showing adhesion at $[Cd^{2+}] \geq 0.25$ mM (c-e) with the corresponding RICM images (c,e). The white scale bar is 10 µm; the black scale bar is 2 µm.

(a)

no Cd^{2+}

(b)
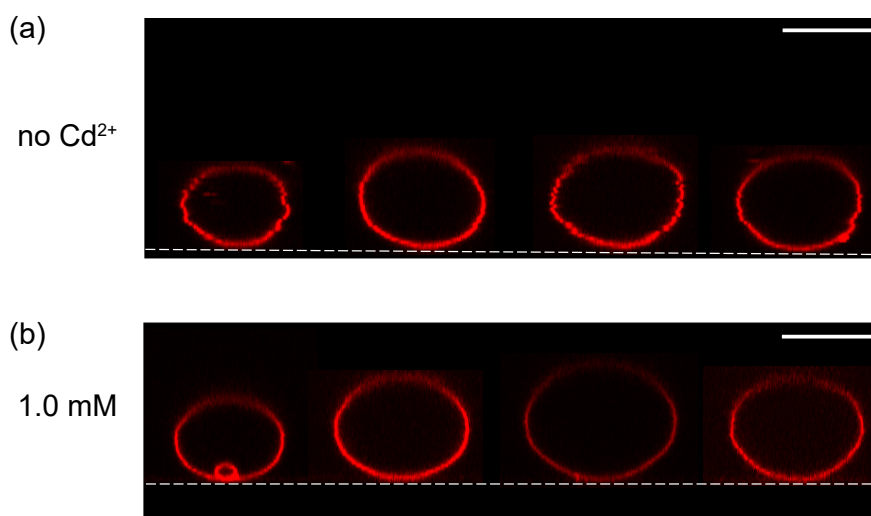
1.0 mM

Figure 4.13. DOPC vesicle on a pure DOPC bilayer in (a) the absence and (b) the presence of [Cd^{2+}] = 1.0 mM, showing no clear sign of adhesion in both cases. The sacle bar is 10 μm.

ity due to modulating the pH value, where a breakdown of Young-Dupré wetting as described in section 3.4 due to the formation of blisters, was observed.[136] In contrast, the experiments presented in this work were performed in the presence of 10 mM Tris buffer showing no detectable difference in wetting behavior for a pure DOPC bilayer without pAA-Cys5 brushes grafted onto it as shown in figure 4.13. In section 4.2 a clear compaction of pAA-Cys5, accompanied by an decrease in roughness was observed due to a slight change of [Cd^{2+}] in the presence of 100 mM NaCl and 10 mM Tris buffer. Thus, the adhesion can be modulated without changing the pH value nor the electrochemical screening. Further no change in temperature is required to modulate the wetting behavior, as necessary for thermoresponsive polymers, such as poly(N-isoprpylacrylamide)[137], avoiding the hydrodynamic perturbation by thermal convection. Okhata *et al.*, e.g., grafted poly(N-isopropylacrylamide) onto nylon capsules to control their permeability for drug release by temperature changes.[138]

4.5 Determination of adhesion free energy of GUVs on pAA-Cys5 at different Cd^{2+} concentrations

In section 4.4 it is shown qualitatively that the onset of wetting of pAA-Cys5 by GUVs occured at [Cd^{2+}] $\geq$ 0.25 mM. In the following section the adhesion strength $\Delta\gamma_W$ is investigated to gain quantitative insights into the concentration dependent adhesion. In figure 4.14a) a typical reflection interference contrast microscoy (RICM) image of a vesicle deposited on a pAA-Cys5 coated substrate in the presence of Cd^{2+} is shown. The signal intensity was integrated following the azimuth angle ϕ to increase count-

ing statistics as shown in figure 4.14b). Executing an inverse cosine transformation according to equation (3.84) of the radially integrated RICM intensity profiles, enables to obtain the height profile of the vesicle in the vicinity of the substrate shown in figure 4.14c). The length over which the vesicle shape is dominated by elasticity is the capillary length λ which is given in equation (4.2).[139][140]

$$\lambda = \sqrt{\frac{\kappa}{\sigma}} \qquad (4.2)$$

Here, κ is the bending rigidity and σ the tension. The determination of the contact angle between the vesicle membrane and the substrate is difficult due to the curvature of the contour. Bruinsma wrote down an equation which overcomes this problem describing the height profile $z(r)$ in dependence of λ and the macroscopic contact angle α presented in equation (4.3).

$$z(r) = \alpha(r - r_\mathsf{E} - \lambda_E) + \alpha\lambda_E \exp\left(-\frac{r - r_\mathsf{E}}{\lambda_\mathsf{E}}\right) \qquad (4.3)$$

Equation (4.3) is only valid at the edge of adhesion zone, where $r = r_\mathsf{E}$ and $\lambda = \lambda_\mathsf{E}$. In figure 4.14c) the fit (green line) is according to equation (4.3). This expression was used in previous studies to obtain the effective contact angle α and the capillary length λ_E.[25][24] The solution Bruinsma[140] obtained is based on the minimization of the free energy of a membrane patch in Monge representation for zero-ranged, contact interactions fulfilling the boundary conditions: $z = 0$, $\frac{dz}{dr} = 0$ and $\frac{d^2z}{dr^2} = \frac{\alpha}{\lambda_\mathsf{E}}$, yielding the curvature of the contour $C_{1\mathsf{max}}$. The adhesion free energy can be calculated via $\Delta\gamma_\mathsf{W} = \frac{\kappa}{2} C_{1\mathsf{max}}^2$ with $\kappa \approx 1 \times 10^{-19}$ J as reported previously[49] and described in detail in section 3.10.1. The curvature $C_{1\mathsf{max}}$ is plotted versus the vesicle radius R_eq showing similar curvatures for the probed vesicle sizes as shown in figure 4.14d), where the average curvature $C_{1\mathsf{max}} = 1.81\ \mathsf{\mu m}^{-1}$, yielding $\Delta\gamma_{\mathsf{W},1.0\ \mathsf{mM}} \approx 40\ \mathsf{k}_BT/\mathsf{\mu}m^2$ for vesicles in the presence of 1 mM Cd^{2+}, which is in good agreement with the free energy obtained for integrin-mediated vesicle adhesion.[25][24]

In the same manner the adhesion free energy for a vesicle in the presence of 0.25 mM Cd^{2+} was determined to be $\Delta\gamma_{W,0.25\ mM} \approx 24\ k_B T/\mu m^2$.
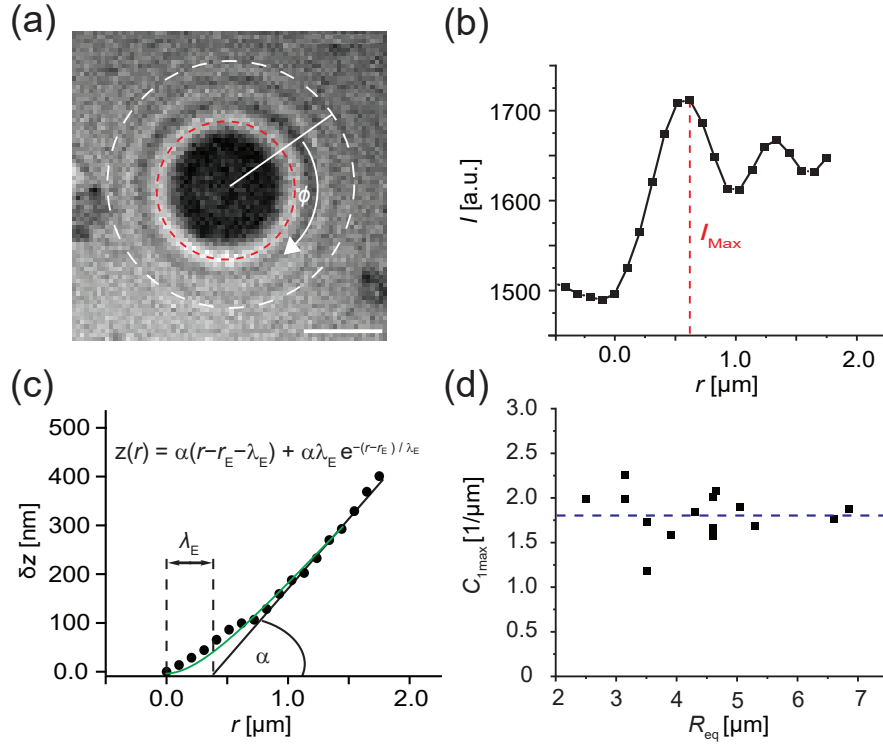
Figure 4.14. Determination of adhesion free energy $\Delta\gamma_W$ in the presence of $[Cd^{2+}] = 1.0$ mM. RICM snapshot of a vesicle adhering onto a pAA-Cys5 coated substrate (a); Radially integrated relative intensity along azimuth angle ϕ according to panel 4.14(a); Membrane height δz *versus* distance r reconstructed from panel 4.14 (b); Contact curvature C_{1max} *versus* vesicle radius R_{eq}.

4.6 Determination of absolute interfacial potential between GUVs and pAA-Cys5 at different Cd^{2+} concentrations

In addition to the curvature of the vesicle contour in the vicinity of the interface, presented in section 4.5, the membrane height fluctuations of the adhered membrane within the adhesion zone can be monitored via RICM and analyzed as described in details in section 3.10.2. In brief, height fluctuations δz of the adhered membrane can be calculated of the intensity fluctuations following equation (3.84) and were monitored over 12 s with a time resolution of 30 ms as shown in figure 4.15a). The height fluctuations δz yield the height fluctuations probability distribution $P(\delta z)$ presented in figure 4.15b) following a Boltzmann probability distribution as shown in equation (4.4).

$$P(\delta z) = \exp\left(-\frac{V(\delta z)}{k_B T}\right) \tag{4.4}$$

The potential energy $V(\delta z)$ around the minimum at $\delta z = 0$ can be written in form of a Taylor series expansion resulting in equation (4.5).

$$V(\delta z) = -\Delta \gamma_{\mathsf{W}} + \frac{1}{2}V"\delta z^2 \qquad (4.5)$$

The adhesion free energy is denoted by $\Delta \gamma_{\mathsf{W}}$ giving the potential minimum, while $V"$ is the curvature of the potential, which is independent from the potential minimum $\Delta \gamma_{\mathsf{W}}$. Therefore $\Delta \gamma_{\mathsf{W}}$ can be neglected yielding equation (4.6).

$$P(\delta z) = \exp\left(-\frac{1}{2}\left(\frac{V"\delta z^2}{K_B T}\right)\right) \qquad (4.6)$$

The probability distribution $P(\delta z)$ determined from the experiments can be well approximated by a Gaussian distribution as shown by the fit in figure 4.15b). A Gaussian distribution in general can be written as shown in equation (4.7).

$$P(\delta z) = \exp\left(-\frac{1}{2}\left(\frac{x-\mu}{\sigma}\right)^2\right) \qquad (4.7)$$

Comparing the Gaussian distribution shown in equation (4.7) around the minimum at $\mu = 0$ with equation (4.6) yields the variance shown in equation (4.8).

$$\sigma^2 = \langle \delta z^2 \rangle = \frac{K_B T}{V"} \qquad (4.8)$$

This shows that the mean squared amplitude $\langle \delta z^2 \rangle$ is proportional to the inverse of the second derivative. The maximum of the distribution shown in figure 4.15b) can be well fitted with an parabolic function corresponding to the membrane-substrate interaction from the measured variance $\langle \delta z^2 \rangle$. Assuming that the membrane fluctuations are correlated over a scale of 3 pixels the mean squared amplitude of fluctuations $\langle \delta z^2 \rangle$ can be calculated via equation (4.9), which is described in details in section 3.10.2.

$$\langle \delta z^2 \rangle = \frac{k_B T}{V"(2\Delta_{3p})^2} \qquad (4.9)$$

According to equation (4.8) and equation (4.9) the mean squared amplitude $\langle \delta z^2 \rangle$ is obtained from fitting the distribution in figure 4.15b) with a Gaussian and approximating the maximum with an parabolic function and calculating the second derivative. Assuming a function $y = ax + bx^2 + c$, yields $\langle \delta z^2 \rangle = 1/2b$. Here, $\langle \delta z^2 \rangle_{0.25\ \mathsf{mM}} = 1.035$ nm² and $\langle \delta z^2 \rangle_{1.\ 0\ \mathsf{mM}} = 0.671$ nm². The obtained curvatures of the membrane-substrate interaction near the average height of an adhered membrane patch yield for [Cd^{2+}] = 0.25 mM $V"_{0.25\ \mathsf{mM}} = \mathsf{k}_B T/[\langle \delta z^2 \rangle (2\Delta_{\mathsf{3P}})^2] = (2.5 \pm 1.8) \times 10^{-6}$ k$_B T$/nm^4 and for [Cd^{2+}] = 1.0 mM $V"_{1.0\ \mathsf{mM}} = \mathsf{k}_B T/[\langle \delta z^2 \rangle (2\Delta_{\mathsf{3P}})^2] = (3.9 \pm 0.9) \times 10^{-6}$ k$_B T$/nm^4 (n=15). The increase in $V"$ indicates that the membrane fluctuations in the adhesion zone are more sharply

confined near the substrate. V'' can be interpreted as the spring constant of an harmonic oscillator, but does not yield the potential energy minimum $\Delta\gamma_W$. The simulations show that the transversality condition holds (see equation (3.18))[51] supporting that the adhesion free energy $\Delta\gamma_W$ is the potential minimum. Hence, the absolute interfacial potential $V(z)$ was calculated following equation(3.90) according to the potential minima obtained in section 4.5 $\Delta\gamma_{W,1.0\ mM} \approx 40\ k_BT/\mu m^2$ and $\Delta\gamma_{W,0.25\ mM} \approx 24\ k_BT/\mu m^2$ as shown in figure 4.15c).
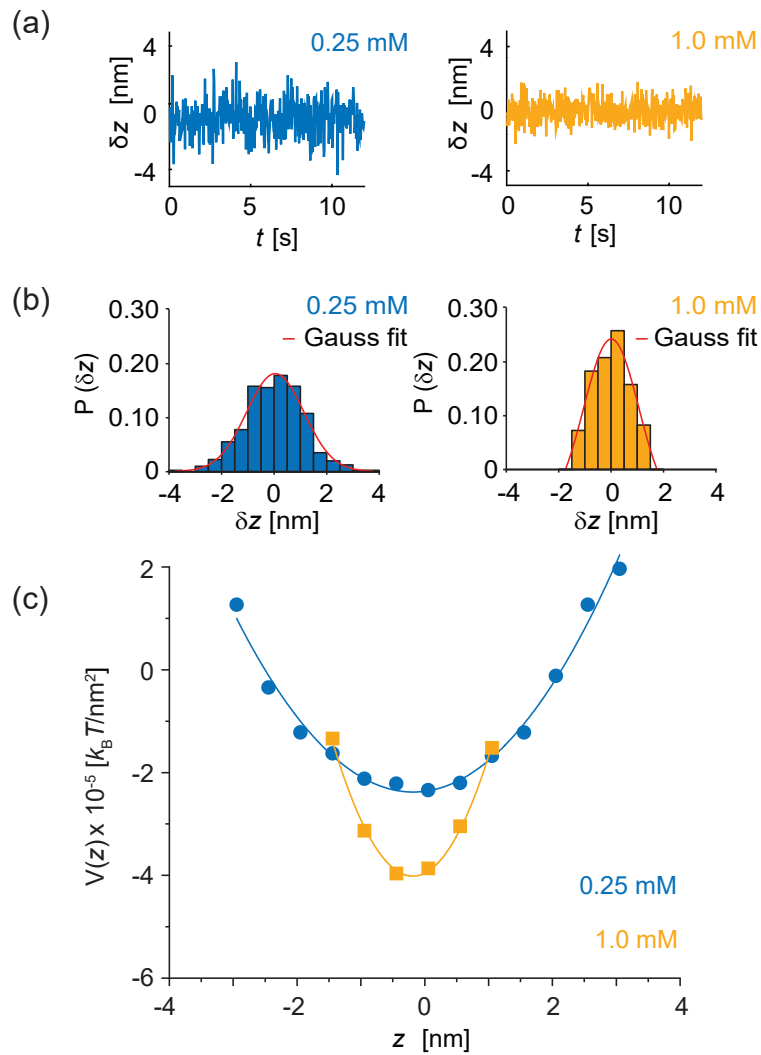
Figure 4.15. Membrane fluctuations of an adhered vesicle modulated by [CdCl$_2$]. a) Laterally averaged membrane-substrate distance δz versus time. b) Corresponding height flucutations probability distribution $P(\delta z)$. c) Absolute interfacial potential $V(z)$ versus z. The potential curvature $V''(z{=}0)$ represents the sharpness of the membrane confinement, where the potential minimum corresponds to $\Delta\gamma_W$, the adhesion free energy (see section 3.10.1).

4.7   Discussion

Polymer brushes have a large variety of applications including biomedical applications. Boronate-containing polymer brushes were found to induce adhesion of cancer cells, while they can be detached by fructose solution.[141] Interestingly, poly (poly (ethylene glycol) methacrylate) can prevent cell adhesion[142], while poly(ethylene glycol) can impede protein adsorption.[143] In fact, GUVs do not adhere on pAA-Cys5 polymer coated substrates in the absence of Cd^{2+}.

Within this study the pAA-Cys5 coated substrate was build up successively and each preparation step was monitored via XRR. The structural parameters obtained from the best fit results of the XRR data for the lipid bilayer are in good agreement with previous studies[127], as well as the obtained parameters for neutravidin.[132][135] The analysis of polymer brushes in a good solvent solution via XRR is non trivial caused by the poor contrast between a hydrated polymer layer and the bulk. Due to the fact of an estimated low contrast between pAA-Cys5 and the bulk solution, neutravidin and pAA-Cys5 were fitted as one slab yielding an SLD value of 9.7×10^{-6} Å^{-2} which is in between the SLD of water and pure neutravidin. The fit was repeated 10 times with the quality criteria of a deviation of less than 10 % for each parameter yielding a total thickness for pAA-Cys5 of 13.9 ± 0.9 nm, which is in good agreement with the data of Yamamoto *et al.*[35] obtained from QCM-D measurements yielding a thickness of $d = 13.4 \pm 2.2$ nm. Czajor *et al.* determined the thickness of a diffusive oligoethylen glycol layer due to splitting the SLD profile into sets of 1 Å thick slabs and successively computing the reflectivity curve as a function of q.[144], while Ahrens *et al.* found that the incorporation of counter ions into a polymer brush is useful to enhance the contrast.[145] In fact, during this study the addition of $[Cd^{2+}] = 1.0$ mM leads to an increasing SLD value. Also the compensation of the charges within the pAA-Cys5 polymer due to incorporation of divalent cations could be monitored by zeta potential measurements.

In a recent study it was found that hydrogels containing liposomes can prevent bacterial adhesion to medical implants such as silicone catheters.[146] Interestingly, Thet *et al.*[147] reported a biosensor for specific bacteria detection based on liposomes with a fluorescently labeled dye inside which gets released due to bacterial toxins, while Wang *et al.* could release pharmaceuticals stored in liposomes due to sono-activation.[148] Mimicking biomimetic prototissues with predictable physical properties is desirable for studying cellular tissues and was achieved due to the adhesion of biotinylated GUVs mediated by streptavidin.[149] Within this study the adhesion was modulated by adding different $[Cd^{2+}]$ showing adhesion energies comparable with integrin-mediated vesicle adhesion.[24][25] In previous studies the curvature of the interfacial potential V'' between inorganic beads and polymer brushes was determined by analyzing the vertical Brownian motion of the beads by microinterferometry[117] yielding distinctive dif-

66

ferences of V'' for latex particles deposited on pAA-Cys5 coated substrates in the absence and presence of $[Cd^{2+}]$ = 1.0 mM.[35] In contrast to beads, GUVs adhering onto a surface show a distinctive adhesion zone, where the membrane fluctuations are modulated by different $[Cd^{2+}]$. As the membrane fluctuations are obtained from regions of 3×3 pixels the correlation over this length scale was taken into account as demonstrated in equation (4.9). The adhesion strength was compared to the respective vesicle size by simulations showing that for the analyzed vesicles the transversality condition holds (see equation (3.18)), which enables the assumption that $\Delta\gamma_W$ corresponds to the potential minimum yielding the absolute interfacial potential.[51] However, it needs to be mentioned that the contribution of buoyancy to the interfacial potential is not taken into account. As the potential strength is strongly linked to the different $[Cd^{2+}]$ the change in brush conformation can be attributed to the different wetting behaviors yielding the onset of wetting at $[Cd^{2+}] \leq 0.25$ mM.

5 Dynamic switching of vesicle-brush interaction

5.1 Transition from non-wetting to wetting of giant unilamellar vesicles onto bio-inspired stimulus responsive polymer brushes

During the last decades GUVs were studied as cell models[47][53][150][151][152] and as *in vivo* delivery systems for pharmaceutic active substances. Papahadjopoulos *et al.* found that a prolonged liposome circulation time, which was achieved by incorporating polyethylene glycol moieties in the membrane of GUVs filled with anti-tumor agents, in blood is associated with an increase in pharmacological efficacy.[153] One widely used anti-tumor agent is Doxorubicin, which is incorporated in liposomes to improve its therapeutic activity.[154] This indicates that the pharmaceutical effectiveness is associated with the wetting properties of liposomes on the respective body tissues. Ngassam *et al.*[155] observed the dynamic rupture of GUVs onto hydrophobic and hydrophilic surfaces with a time resolution in the order of seconds monitoring the decrease in contact area and the number of ruptured vesicles, while Borghi *et al.* observed the dynamic spreading of GUVs onto polylysine-coated glass microfibers proposing a new fiber coating technique.[156] In a previous study it was found that the spreading of GUVs on poly-L-lysine modified (PAA)gels with different elastic moduli caused traction stresses on the substrates.[157] In the following, the dynamic wetting of pAA-Cys5 by GUVs is investigated via RICM imaging of the time dependent local height fluctuations with a time resolution of 30 ms which is significantly higher than in the previous studies.

5.1.1 Results

Biotinylated pAA-Cys5 polymer brushes were coupled to a DOPC lipid bilayer containing biotinylated lipids via neutravidin as a linker molecule (see section 4). In a next step GUVs were deposited onto the polymer and sedimented. Thus, they are hovering over the surface showing a characteristic pattern of periodically switching between bright and dark spots in the vesicle center, presented in figure 4.11a). 40 µl of a solution containing $[Cd^{2+}]$ = 1 mM was added to the channel and the vesicle was monitored via RICM with a time resolution of 30 ms, showing no contact as indicated by the white disc in the vesicle center after Δt = 2 s. At Δt = 6 s the spot in the center gets darker as presented in figure 5.1b), indicating vesicle adhesion. In figure 5.1c) the vesicle is monitored at Δt = 40 s after Cd^{2+} injection showing that the contact zone increased in size, indicating a stable contact. In figure 5.1d) the relative height fluctuations δz obtained from the mean intensities of a square of 3×3 pixels in the vesicle center according to equation (3.84) are plotted versus Δt. The time point i) corresponds to the height fluctuations where no contact between the vesicle and the substrate is es-

tablished. Position ii) is accounted to the transition zone, as the height fluctuations decay but still did not have reached the stady state iii) which represents stable contact between the vesicle and the pAA-Cys5 coated substrate. This indicates a time scale of around 25 s for the non-wetting to wetting transition according to figure 5.1d). In figure 5.1e) the adhesion free energy $\Delta\gamma_W$ is monitored over time Δt, where $\Delta\gamma_W$ was determined according to the "Bruinsma-method" presented in sections 3.10.1 and 4.5. The images where the vesicle shows a white disc in the center at $\Delta t = 0$ and 2 s could not have been analyzed by applying the "Bruinsma-method", as it is only viable for adhered vesicles.
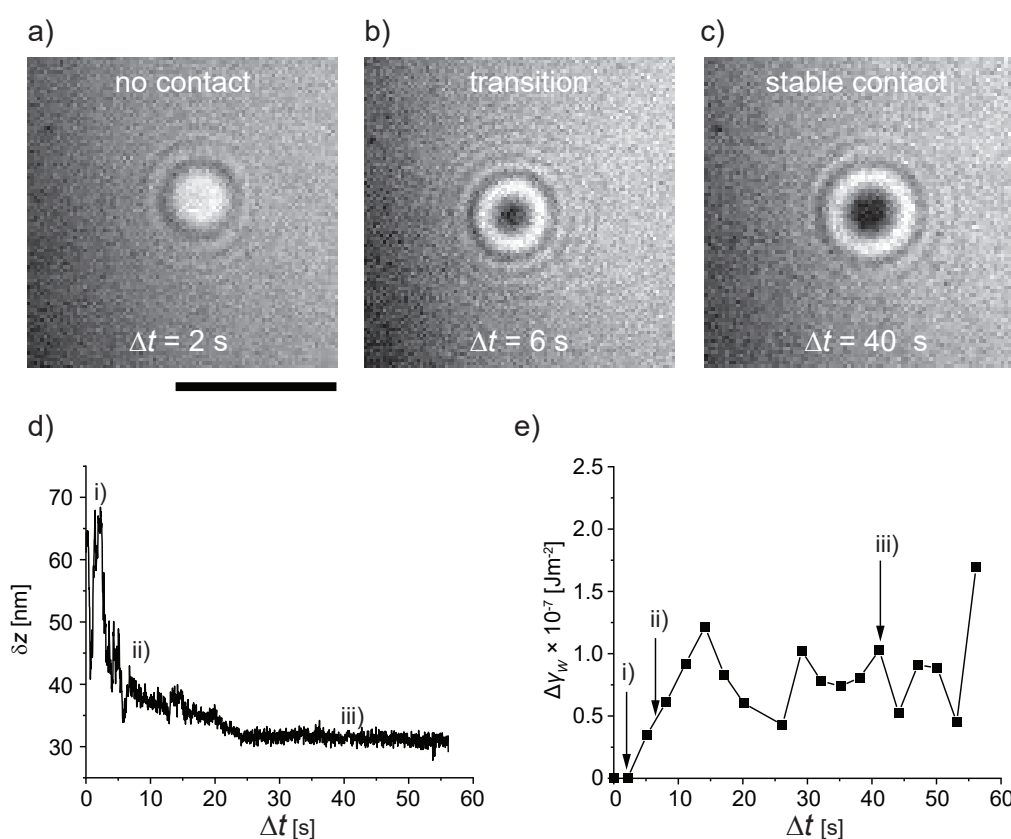
Figure 5.1. 2000 consecutive RICM snapshots (30 ms between frames) of a vesicle approaching the pAA-Cys5 coated substrate. a) no contact between vesicle and substrate at $\Delta t = 2$ s; b) transition $\Delta t = 6$ s obtained from exponential time constant; c) stable contact after $\Delta t = 40$ s. d) height fluctuations δz over time; e) Corresponding adhesion free energy monitored over time; Scale bar is 5 μm.

Therefore the adhesion free energy for those time points was set to zero. At $\Delta t = 5.13$ s $\Delta\gamma_W$ increases to 3.49×10^{-8} J/m² monotonically increasing further up to $\Delta\gamma_W = 1.22 \times 10^{-7}$ J/m² at $\Delta t = 14.13$ s. Next, $\Delta\gamma_W$ decreases back to 4.29×10^{-8} J/m² at $\Delta t = 26.13$ s. After 3 s $\Delta\gamma_W$ increased back to 1.022×10^{-7} J/m², then it decreases successively before it increases again up to $\Delta\gamma_W = 1.03 \times 10^{-7}$ J/m² at $\Delta t = 41.13$ s. The obtained adhesion free energies are slightly lower than those obtained for GUVs on pAA-Cys5

coated substrates in the presence of 1 mM Cd^{2+} ($\Delta\gamma_W = 1.63 \times 10^{-7}$ J/m²) presented in section 4.5.

Between $\Delta t = 2$ s and $\Delta t = 6$ s the vesicle shows the transition from no contact (figure 5.1 a) to contact as shown in figure 5.1b). That is why in figure 5.2 a temporal zoom with a resolution of 30 ms is presented showing a dark spot in the vesicle center for the first time at $\Delta t = 3030$ ms, indicating adhesion. Until $\Delta t = 3930$ ms the dark spot increases further, while at $\Delta t = 4230$ ms the spot is only barley seen again, before it grows again and the vesicle establishes stable contact.
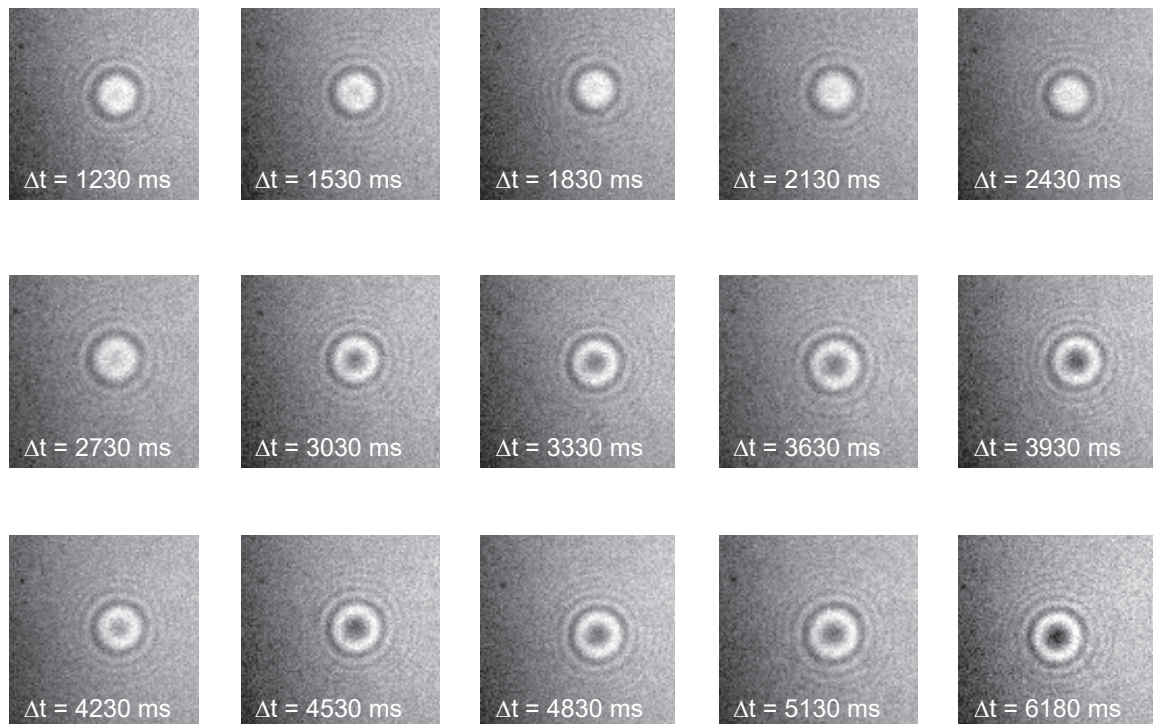
Figure 5.2. Time series between i) and ii) according to figure 5.1 corresponding to 1230 ms $\leq \Delta t \leq$ 6180 ms visualizing the establishment of a contact zone in the center of the vesicle.

5.1.2 Discussion

Wetting dynamics are of high importance for many industrial applications including lubricants, adhesives and printing.[67][68][158] To design bio-inspired materials understanding of dynamic wetting processes is also of high interest. Interestingly, inspired by the feeding of shorebirds a new material was developed, which can collect water from foggy air[159], while the legs of water striders show self removing abilities of condensed water from the insects legs.[160] Bayer *et al.* observed the dynamic wetting of substrates with different wetting properties by water droplets of sizes between 1.3-2.8 mm in diameter and observed the process of spreading by an ultra fast camera, which enabled to monitor the contact angle with a time resolution in the order of ms.[161]

In contrast to liquid droplets, GUVs are much smaller having a diameter between 5-50 μm, wherefore the observation of the global shape can not be achieved by using a camera compared to liquid droplets. Ngassam *et al.* observed the dynamic rupture of GUVs on hydrophilic and hydrophobic substrates with a time resolution in the order of seconds by monitoring the diameter of the vesicles with an fluoresence microscope, while Borghi *et al.* could establish a new coating method of polylysine-coated glass fibers by liposomes due to dynamic spreading.[155][156] In a recent study the radius of the adhesion zone of biotinylated GUVs on streptavidin coated substrates was monitored over time by RICM, where $\Delta t = 0$ was defined as the time point when the vesicle already adhered to the surface.[162].

Within this study the transition between non-adhered and adhered vesicles was monitored by RICM with a time resolution of 30 ms, which enables to extract information about the vesicle shape in the vicinity of the vesicle/substrate contact as shown in section 3.10.1. Therefore the stimulus responsive pAA-Cys5 substrate plays a key role, as it enabled first to let the vesicle sediment showing characteristic hovering over the surface (no adhesion). Adding Cd^{2+} leads to vesicle adhesion. Notably, a super position of sedimentation due to the difference of the interior and exterior media in the inside and outside of the GUVs and dynamic change in adhesion strength due to an increasing concentration of Cd^{2+} influences the process of wetting. The adhesion energy does not approach a constant value during the time the vesicle was monitored which can be attributed to elastic deformations of the vesicle after sedimentation. It has to be considered that the exact $[Cd^{2+}]$ in the vicinity of the vesicle during the transition could not be determined, but comparing the estimated adhesion free energies for $[Cd^{2+}] = 1.0$ mM indicates that the local $[Cd^{2+}] \leq 1.0$ mM, which is reasonable as the theoretical $[Cd^{2+}]$ in the measuring chamber was around 0.2 mM.

5.2 Stop and go motion of GUVs on pAA-Cys5 coated substrates

Dynamic wetting processes are of importance for biological organisms like carnivorous plants[66] and of high interest in technology including lubricants and adhesives.[67][68] However, the fabrication and experimental realization of dynamic switchable substrates to study these phenomena and effects in laboratory model systems, is challenging. Pant *et al.* developed a polystyrene/titania nanocomposite, which can switch the wettability by a liquid droplet from hydrophobic to hydrophilic via exposure to UV-light, while switching the wettability *vice versa* is possible due to thermal annealing at 180 °C.[163] Changing the surface roughness, due to electrostatic actuation, of a PDMS substrate selectively at the front of a droplet leads to a moving droplet without exerting other external stimuli.[164] The fabrication of polymer corals, which can switch their wetting properties between brush and mushroom conformation due to good- and poor solvents was investigated recently, where the interactions between the polymer moieties and the solvent molecules are energetically preferred in case of a good solvent, while the interactions between the polymer moieties themselves are preferable in case of a poor solvent.[165] Consequently, polymers in a good solvent exist in form of brushes, while in a poor solvent they are present in the mushroom conformation. A viable strategy to modulate the cell-substrate interactions was achieved due to hydrogels cross linked via host-guest interactions modulating the substrate stiffness.[166] The movement of GUVs was achieved by the fabrication of an heterogeneous substrate containing the ATPase MinD protein and the ATPase-activating MinE protein. This results in oscillating protein binding and dissociation inducing directional motion, due to asymmetric mechanical force gradients, which was monitored by confocal fluorescence microscopy.[167] Bartelt *et al.*[168] fabricated GUVs which can undergo motion due to photoactived protein dimerization, where the GUVs and the surface are coated with the respective proteins. For the experiments employed within this study the motion of GUVs should be induced by an adhesion gradient without changing the membrane composition. Therefore a microfluidic system was fabricated to switch the solution from $[Cd^{2+}] = 1.0$ mM, where the vesicles adhere, to 10 mM ethylenediaminetetraacetate (EDTA), a chelating agent forming a complex with Cd^{2+} and thereby reducing adhesion gradually. The results are presented in section 5.2.1.

5.2.1 Results

Within this study y-shaped microfluidic channels were fabricated enabling the modulation of [Cd^{2+}] within the channel. To monitor the EDTA distribution in the channel, a mixture of EDTA/Cy5 ($\lambda_{excitation}$ = 647 nm, $\lambda_{emission}$ = 665 nm) was added and visualized by fluorescence microscopy. In brief, GUVs were deposited onto pAA-Cys5 coated substrates at [Cd^{2+}] = 1 mM in a y-shaped microfluidic chamber. In a next step the adhesion was verified under a flow rate of 80 μl/min at [Cd^{2+}] = 1.0 mM. The region of interest of the vesicle at the starting point is indicated by the yellow square in figure 5.3a) and set as Δt < 0. Next, the vesicle was immersed in EDTA by increasing the flow rate of [EDTA] = 10 mM to 80 μl/min and lowering the flow rate of [Cd^{2+}] = 1.0 mM to 30 μl/min. Thereby the Cd^{2+} concentration successively decreases due to the formation of an EDTA-Cd^{2+} complex, which has a dissociation constant of K_D = 2.1 $\times$ 10^{-8} M, which is 3 orders of magnitude lower compared to the pAA-Cys5-Cd^{2+} complex, indicating a more stable complex.[169][34] The time point at which the flow rates are switched is set as Δt = 0. In figure 5.3b) the EDTA distribution was imaged by fluorescence microscopy showing a homogeneous distribution of EDTA in the channel (upper panel). In the presence of Cd^{2+}, presented in the lower panel, no fluorescence is shown from the bulk, which indicates Cd^{2+} flow in the channel. The bright spots can be attributed to GUVs labeled with Texas Red which also show weak intensity at $\lambda_{excitation}$ = 647 nm. The vesicle position is monitored over 120 min, while every two minutes 200 consecutive RICM images with a time resolution of 30 ms were recorded. In figure 5.3c) the RICM image for the starting position Δt < 0 is shown where the vesicle is immersed in [Cd^{2+}] = 1 mM and therefore is attributed to not moving (STOP). Next, the vesicle is immersed in [EDTA] = 10 mM and monitored over the time points Δt = 0, 21, 42, 60, 80 and 100 min showing movement in the direction of flow, indicating that EDTA successfully removes Cd^{2+} from the pAA-Cys5 polymer and thereby decreases the adhesion strength. The black dashed line functions as a guidance for the eyes. In figure 5.3d) the transition from "GO" to "STOP" is monitored. After Δt = 100 min the vesicle is immersed in the initial [Cd^{2+}] = 1 mM solution by increasing the Cd^{2+} flow to 80 μl/min. Consequently, the vesicle does not show further movement at Δt = 115 and 120 min. The center of mass of the vesicle in each snap shot shown in figures 5.3c) and 5.3d) was determined and the relative position of the vesicle was plotted versus time as presented in figure 5.3e). The vesicle moves a total distance between Δt = 0 min and Δt = 100 min of around 1.1 μm, which yields an average velocity of around 10 nm/min.
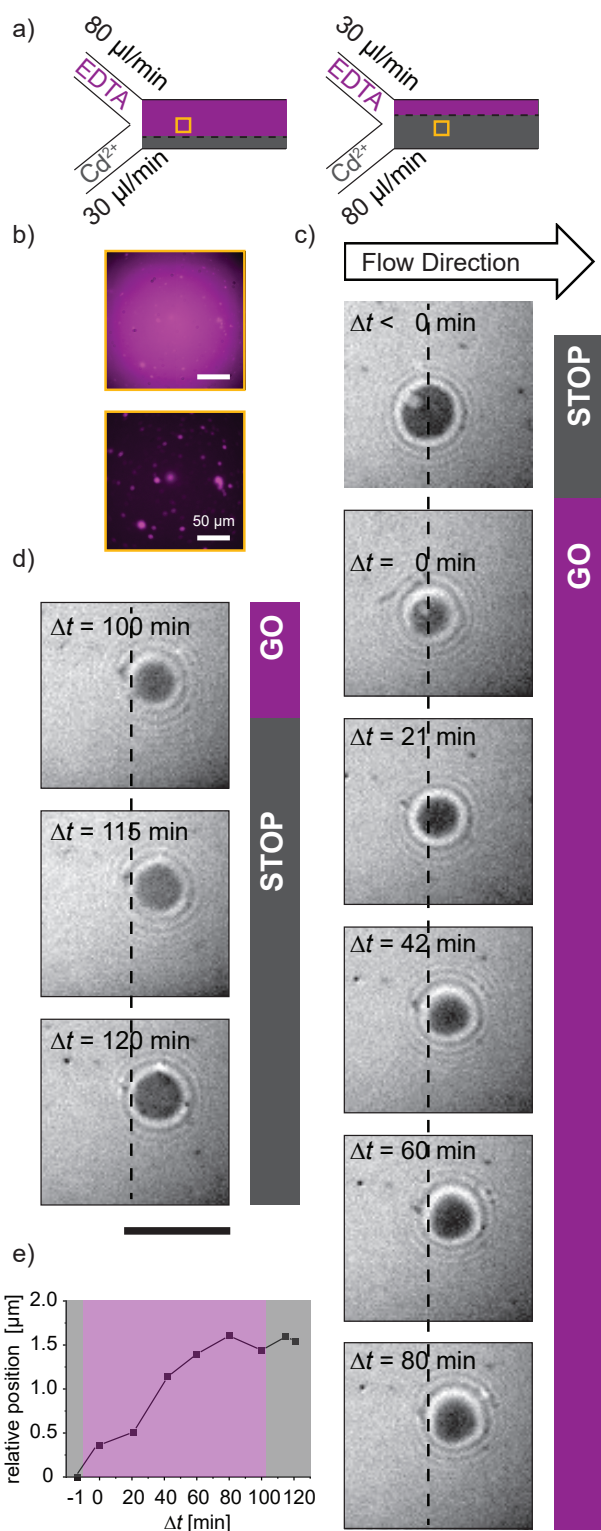
Figure 5.3. Stop go motion of vesicles on pAA-Cys5 coated substrates under flow. a) schematic illustration of y-shaped microfluidic chambers. b) fluorescence intensity of region of interest (yellow square in panel a)) in the presence and absence of EDTA. c) switching from "STOP" to "GO" via changing the medium from 1 mM Cd^{2+} to EDTA; black dashed line perpendicular to the direction of flow as a guidance for the eye to track the vesicle movement over time. d) switching from "GO" to "STOP" due to changing the medium back to $[Cd^{2+}]$ = 1.0 mM, black dashed line indicates no vesicle movement. e) relative position of the vesicle monitored over time. Scale bar = 5 µm.

Since the vesicle between Δt = 21 min and 42 min is moving the fastest compared to the other time intervals, this time region is investigated in more detail. In figure 5.4a) a RICM snapshot of the vesicle at Δt = 21 min is shown and the vesicle contours at the rear (green) and at the front (red) are extracted. This is accomplished by following the procedure introduced in section 3.10.1. Here, the average contour of the first 5 frames was taken into account for the analysis. According to equation (4.3) fitting the contours yields the capillary lengths λ_{rear} = 0.30 µm (green fit) and λ_{front} = 0.29 µm (red fit). The RICM image and the corresponding profiles for the vesicle at Δt = 28 min are presented in figure 5.4b). The vesicle contours for the rear and for the front are steeper compared to Δt = 21 min, yielding λ_{rear} = 0.22 µm (green fit) and λ_{front} = 0.25 µm (red fit). At Δt = 32 min the contours are more flattened compared to the time points before yielding λ_{rear} = 0.59 µm (green fit) and λ_{front} = 0.65 µm (red fit), before they get steeper again as can be seen in figure 5.4d) and e) yielding λ_{rear} = 0.10 µm (green fit) and λ_{front} = 0.13 µm (red fit) respectively λ_{rear} = 0.12 µm (green fit) and λ_{front} = 0.11 µm (red fit). In figure 5.4f) the relative position of the vesicle is plotted versus the time (black) with the indicated time points corresponding to figure 5.4a)-e) demonstrating that the vesicle moved from Δt = 21 min to Δt = 42 min around 0.52 µm corresponding to an average velocity $\langle V \rangle$ of around 25 nm/min. The red curve represents the first derivative of the relative position dx/dt versus time yielding the velocity, resulting in a maximum velocity V_{Max} of around 60 nm/min. The velocity profile indicates that the vesicle is not moving continuously but having a distinct maximum in velocity at Δt = 28 min. In figure 5.4g) the capillary lengths corresponding to the contours at the rear and front of the vesicle are plotted versus time showing that after reaching V_{Max} at Δt = 28 min the capillary length of the front and rear show a maximum, which indicates that the vesicle at this time point has the flattest contour. This is reasonable as a non adhered vesicle can be approximated by an ellipse only having one point of contact to the surface.
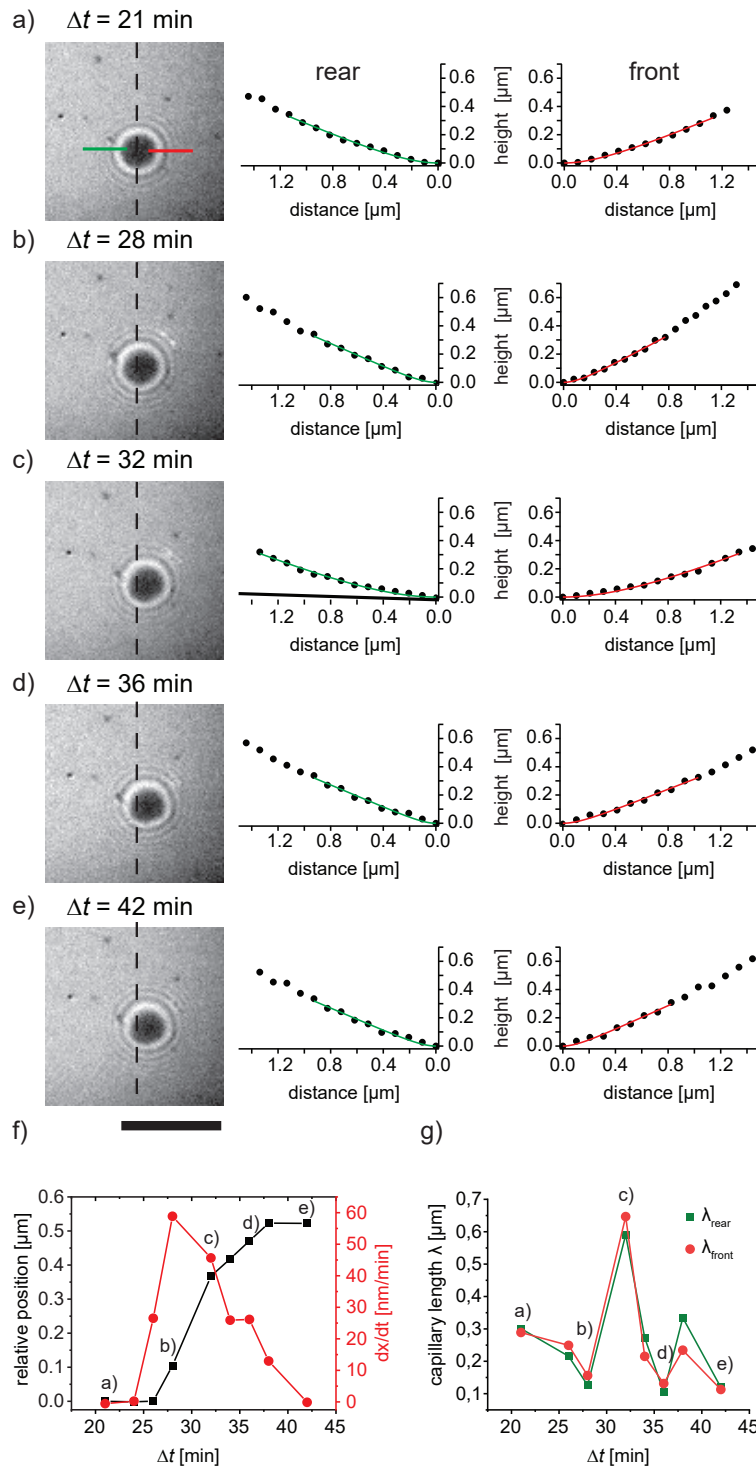
Figure 5.4. Change in vesicle position between Δt = 21-42 min and corresponding contour analysis of RICM images. The intensity profiles of the rear (green) and of the front (red) were averaged over 5 frames yielding the vesicle contour, where the capillary length λ was extracted by the Bruinsma equation (see equation (4.3)). a) vesicle position and contours after Δt = 21 min, b) Δt = 28 min, c) Δt = 32 min, d) Δt = 36 min, e) Δt = 42 min, f) vesicle position over time, g) difference of λ_{front} and λ_{rear}. Scale bar is 5 μm.

5.2.2 Discussion

Previous studies suggest an increasing interest of dynamically switchable surfaces, due to their importance in industrial technologies[67][68] and for the cultivation of stem cells, where dynamically switching the elasticity of a polymer coated substrate can enhance the duration of multiple lineage potentials of the cells.[170] Within this study the motion of a vesicle in a microfluidic chamber was controlled via external stimuli due to Cd^{2+} addition or removal by complexation via EDTA, which enables to "stop" and to "move" the vesicle via switching the flow rates. As Cd^{2+} is toxic this particular system can not be used to cultivate stem cells but is a promising proof of concept as the switching of the pAA-Cys5 properties does not alter the pH value, electrostatics or the temperature in the channel, nor needing UV light as reported for other dynamic switchable substrates.[163][165][170]

The adhesion gradient on the substrate combined with a gentle flow induces the directional motion of the GUVs. A sliding motion of a liquid droplet results in an receding and advancing contact angle, where the advancing contact angle is larger than the receding one.[171] Lam *et al.* found that for moderate rates up to at least 1 mm/min the dynamic contact angle is identical with the static contact angle.[172] In contrast to liquid droplets, within this study the motion of a lipid vesicle under moderate flow was investigated. That is why in analogy to the contact angle the curvature of the vesicle in the vicinity of the adhesion area was investigated by the Bruinsma equation yielding the capillary length λ. The capillary lengths of the contour at the front λ_{front} and at the rear λ_{rear} are similar, however until Δt = 34 min $\lambda_{\text{front}} > \lambda_{\text{rear}}$. This tendency is in agreement with the motion of liquid droplets, where the advancing contact angle is larger than the receding one. Considering that the vesicle does not move between Δt = 21 min and 26 min and has a clear maximum in velocity at Δt = 28 min, indicates a so called stick-jump motion. After the "jump" $\lambda_{\text{rear}} > \lambda_{\text{front}}$ suggesting an elastic relaxation due to the loss in velocity, which is reasonable considering that GUVs are elastic shells compared to droplets.

6   Interaction of oxidized lipids with C-reactive protein

C-reactive protein (CRP) is an established marker for inflammations, injuries and infections in clinical examinations.[173] It is well known that CRP activates the complement component 1q (C1q) on apoptotic cells activating the classical complement pathway of the immune system.[174] Further, there is evidence that CRP binds favorable to PC moieties.[41] Chang *et al.* found that it binds to oxidized low density lipoprotein (LDL) and PC moieties.[42] In recent studies Korytowski monitored the size of lipid vesicles by DLS measurements with various degrees of oxidation in dependency on the CRP concentration indicating a higher binding affinity with an higher degree of lipid oxidation.[46] Based on these findings the influence of lipid oxidation on the binding of CRP is further investigated. First in section 6.1 the electrostatic interactions are probed via zeta potential measurements. In section 6.2 the influence on membrane mechanics due to binding of CRP is investigated via flicker spectroscopy and in section 6.3 the affinity between CRP and the respective lipids is quantitatively compared.

6.1   Role of electrostatics in CRP binding to oxidized lipids

To investigate the role of electrostatic interactions of the binding of CRP to oxidized lipids, zeta potential measurements were carried out. In figure 6.1 the changes in zeta potential of POPC, POPC/PazePC and POPC/PoxnoPC small unilamellar vesicles (SUVs) incubated with 0, 0.8 and 2.9 µm CRP are shown. The zeta potential of 1-palmitoyl-2-oleoyl-glycero-3-phosphocholine (POPC) vesicles (black squares) showed no remarkable change as the zeta potential for all three [CRP] yields z ≈ 7-9 mV, indicating no interaction between CRP and the pure POPC SUVs. This is in agreement with dynamic light scattering (DLS) and isothermal titration calorimetry (ITC) data from previous studies.[46] The zeta potential of POPC/Poxno vesicles (red circles) in the absence of CRP (z ≈ 7 mV) was very similar to pure POPC. In the presence of [CRP] = 0.8 and 2.9 µM the zeta potential did not show remarkable changes (z ≈ 8-10 mV). Although, DLS and ITC measurements[46] indicate an interaction between CRP and the POPC/Poxno membranes, zeta potential measurements revealed that the surface potential of the membranes seems not to be affected. In contrast, POPC/PazePC vesicles display a significantly lower zeta potential (z ≈ -5 mV). The negative zeta potential is reasonable taking flipping of -COOH groups of PazePC into account, which was suggested by molecular dynamics (MD) simulations.[175] In the presence of [CRP] = 0.8 µM the sign of the potential reversed (z ≈ = 3 mV), while in the presence of [CRP] = 2.9 µM the zeta potential increased slightly further (z ≈ 4 mV). For the increase in zeta potential there are two possible explanations. One reasonable scenario might be that the

78

binding of CRP is facilitated electrostatically by negative charges carried by PazePC. As DLS and ITC data show that CRP also leads to aggregates of PoxnoPC vesicles, electrostatically modulated binding seems to be unlikely. A second viable scenario is that binding of CRP is screening the electrostatics of the negatively charged lipids on the membrane surface, which do probably not play a significant role in facilitating CRP binding. The experiments were performed in 10 mM Tris buffer corresponding to a Debye screening length of about $\kappa^{-1} \approx 3$ nm. CRP can be approximated by a pentameric ring with a diameter of 8 nm and a thickness of 3 nm.[176] Thus CRP, which is bound to the membrane, can screen the electrostatics. Hence, increase in zeta potential of PazePC leads to the interpretation that CRP binding causes screening of the negative charges located on the vesicle membrane.
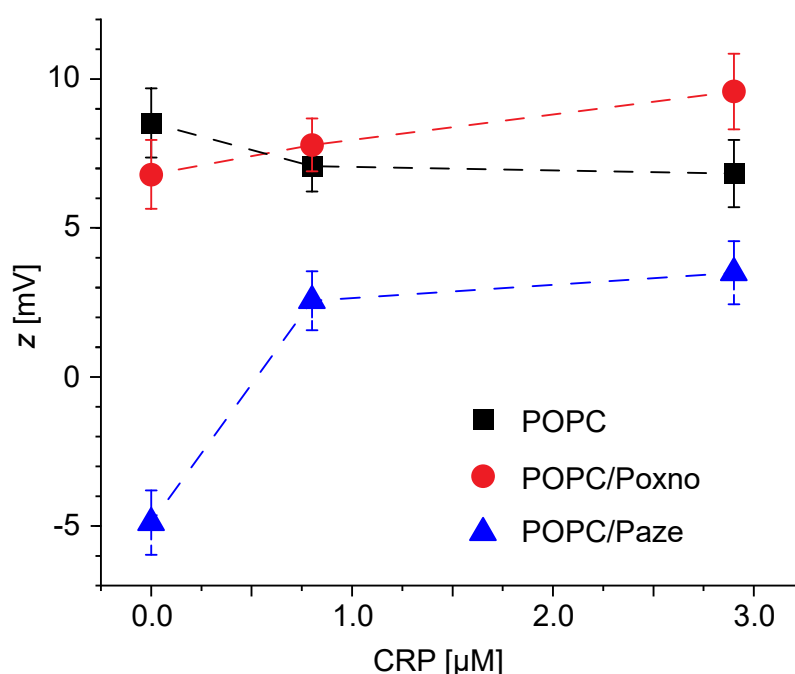
Figure 6.1. Zeta potential of POPC (black), POPC/PoxnoPC (red) and POPC/PazePC vesicles (blue) measured at [CRP] = 0, 0.8 and 2.9 µM.

6.2 Influence of CRP binding on membrane mechanics

To shed light on how the binding of CRP influences the mechanical properties of the respective lipid bilayer membranes, the thermal fluctuation of the membrane contour of GUVs was monitored in the presence and absence of 0.8 µM CRP. Next the bending rigidity κ was calculated via equation (3.14) (see section 3.3). In the following the data from POPC and POPC/PazePC are presented. It should be noted that it was not possible to prepare POPC/PoxnoPC GUVs as they form large aggregates. The bending rigidities κ for POPC GUVs in the absence (grey) and presence of 0.8 µM CRP (black)

are presented in figure 6.2a. The boxes represent the 25–75 percentiles, whereas the whiskers represent the 5–95 percentile ranges. The red lines correspond to the mean values. The bending rigidity κ for pure POPC GUVs (figure 6.2a, grey) yields $\kappa_{POPC} = 0.58 \pm 0.25 \times 10^{-19}$ J (n=7) which is in good agreement with previous reports for fluid phospholipid vesicles yielding $\kappa \sim 10^{-19}$ J.[47][49] In the presence of 0.8 μM CRP (figure 6.2a, black) no major changes compared to the data without CRP were found resulting in $\kappa_{POPC+CRP} = 0.43 \pm 0.13 \times 10^{-19}$ J (n = 10). This result is confirmed by the statistical analysis via t-test showing no statistical significance between the two data sets for POPC in the absence and presence of 0.8 μM CRP ($p > 0.05$). In figure 6.2b the analogical data for POPC/PazePC in the absence (light blue) and in the presence of 0.8 μM CRP (blue) are presented. In the absence of CRP κ of POPC/PazePC ($\kappa_{POPC/PazePC} = 0.31 \pm 0.07 \times 10^{-19}$ J, n = 6) is smaller compared to κ of pure POPC without CRP. Considering previous studies the decrease in $\kappa_{POPC/PazePC}$ might be attributed to a decrease in the lateral packing density of the hydrocarbon chains caused by the carboxy-groups from PazePC. Indeed, quartz crystal microbalance with dissipation (QCM-D) studies indicated that the vesicles were more prone to bending deformations.[44] The presence of 0.8 μM CRP leads to an increase in κ ($\kappa_{POPC/PazePC+CRP} = 0.47 \pm 0.17$, n = 9) compared to $\kappa_{POPC/PazePC}$. This difference was statistically significant ($p < 0.05$) indicating that CRP interacts with PazePC by increasing its bending rigidity.
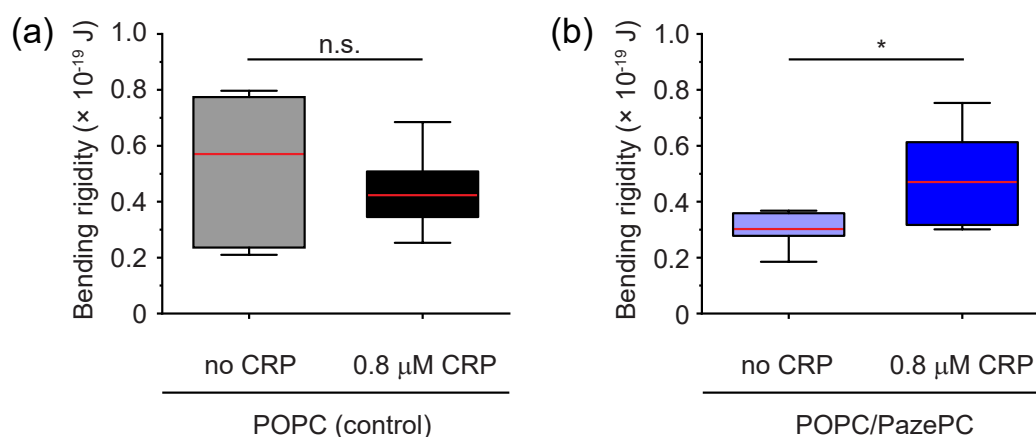
Figure 6.2. Influence of CRP on the mechanical properties of GUVs determined via flicker spectroscopy analysis. (a) Bending rigidity κ of POPC GUVs in the absence (grey) and presence of 0.8 μM CRP (black). (b) κ of POPC/PazePC in the absence (light blue) and presence of 0.8 μM CRP (blue). The red line represents the mean value. The boxes correspond to the 25–75 percentile ranges, and the whiskers to the 5–95 percentiles. The asterisk indicates $p < 0.05$ according to the Student-T-test.

In figure 6.3 representative fits of vesicle contours (red) obtained by the procedure described in section 3.3 and their corresponding representative flicker spectra are shown.

The contour fit and flicker spectrum for a POPC vesicle in the absence and in the presence of 0.8 µM CRP are presented in figure 6.3a) and 6.3b). In figure 6.3c) and figure 6.3d) the flicker spectra for POPC/PazePC in the absence respectively the presence of 0.8 µM CRP are shown as representative experimental data.
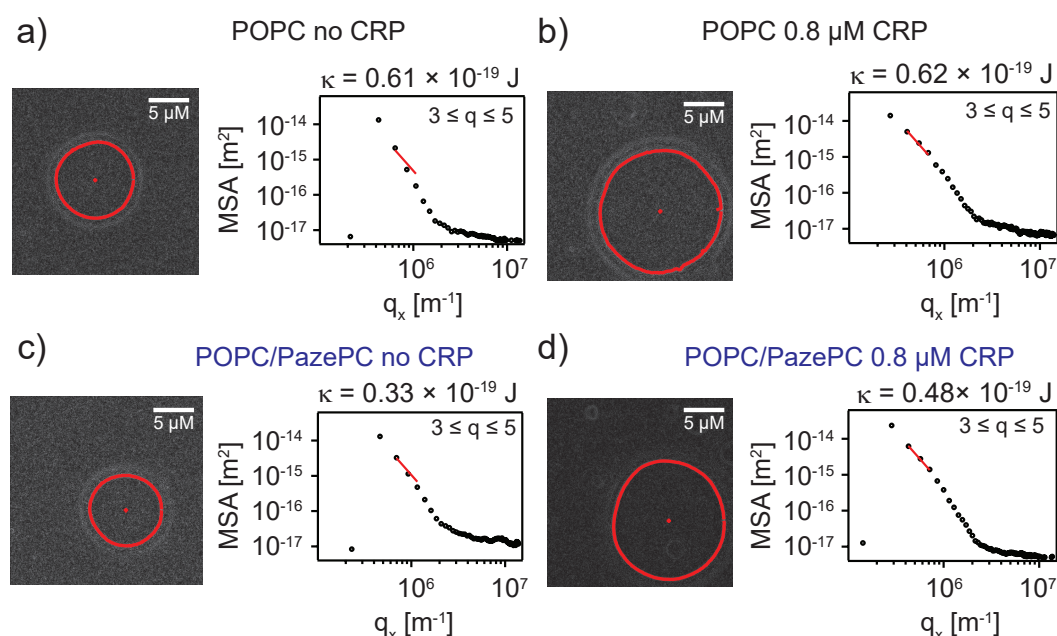
Figure 6.3. Phase contrast images processed with the ImageJ macro "Image Differentials" overlayed with the detected rim position (red circle) and the center of mass (red cross) and the corresponding flicker spectra for representative vesicles for a) POPC in the absence of CRP; b) POPC at [CRP] = 0.8 µM; c) POPC/PazePC in the absence of CRP; d) POPC/PazePC at [CRP] = 0.8 µM.

6.3 Affinity of CRP to phospholipid membranes

The affinity between CRP and POPC membranes immobilized on Si-beads with a diameter of d = 10 µm is compared via determining their partition coefficients P as illustrated in figure 6.4. The partition coefficient P is defined as shown in equation (6.1).

$$P = log\left(\frac{[C_{\text{mem}}]}{[C_{\text{sup}}]}\right) \tag{6.1}$$

The [CRP] bound to the membrane C_{mem} can be expressed as the difference between the initial [CRP] C_{init} and [CRP] in the supernatant C_{sup}. Due to the density difference between the Si-beads (ρ = 2.33 g/ml) and the aqueous solution the separation of the CRP bound to the membrane on the beads and in the supernatant was possible via mild centrifugation (100 g, 30 s). This would not have been possible by using only vesicle suspensions where the density is almost identical to water. Several studies

have shown that the binding of CRP to PC is mediated via Ca^{2+}.[41,177] That is why the negative control experiments were carried out in the absence of Ca^{2+}.
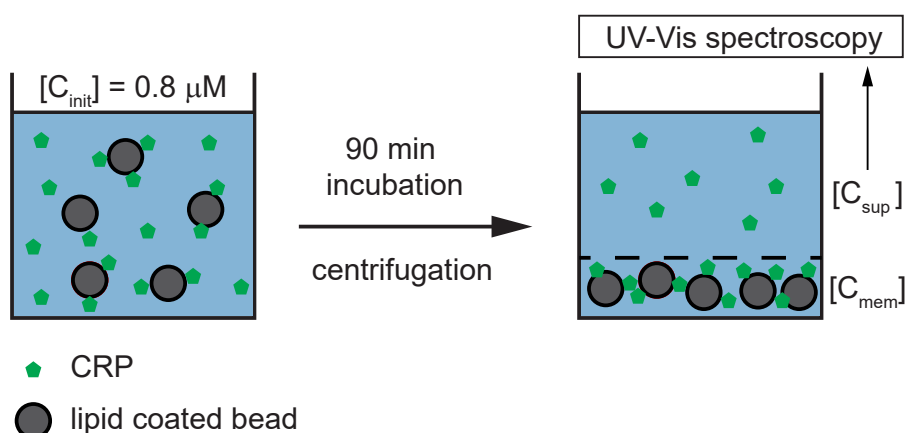
Figure 6.4. Experimental setup for partition coefficient P determination of CRP to lipid membranes with and without PazePC deposited onto Si-beads. $[C_{sup}]$ was determined via UV-Vis spectroscopy at $\lambda = 280$ nm. The experiments were performed in the presence and absence of Ca^{2+} to verify the Ca^{2+} mediated interaction between CRP and PC.

Si-beads were incubated with POPC/PazePC membranes labeled with 0.2 mol% DHPE-Texas Red and the homogeneously coating was confirmed by fluorescence microscopy as shown in figure 6.5. Prior to the determination of unbound CRP in the supernatant $[C_{sup}]$ a calibration curve for pure in buffer dissolved CRP of different concentrations was obtained by UV-Vis measurements at $\lambda = 280$ nm as presented in figure 6.6.
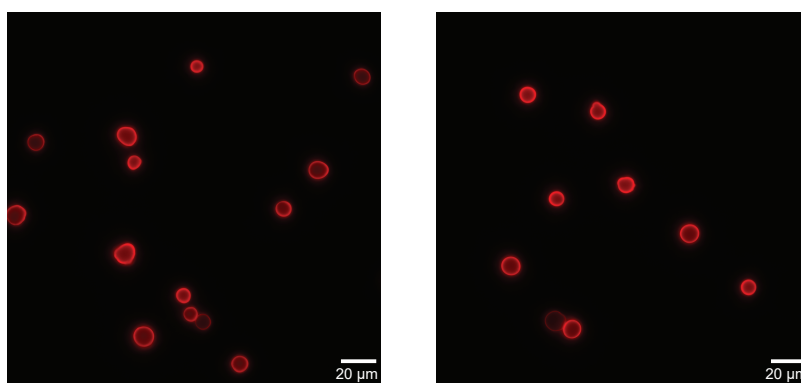
Figure 6.5. Fluorescence images of Si-beads coated with POPC/PazePC lipid membranes containing 0.8 µM CRP to verify homogeneous coating.

In table 6.1 the partition coefficients P are presented according to equation (6.1).
In the absence of Ca^{2+} the partition coefficient P yields negative values for POPC as well as for POPC/PazePC, whereas in the presence of $[Ca^{2+}] = 1.0$ mM the partiton coefficient is positive for both membrane compositions. This confirms that the presence of Ca^{2+} is required for the interaction between CRP and the respective mem-
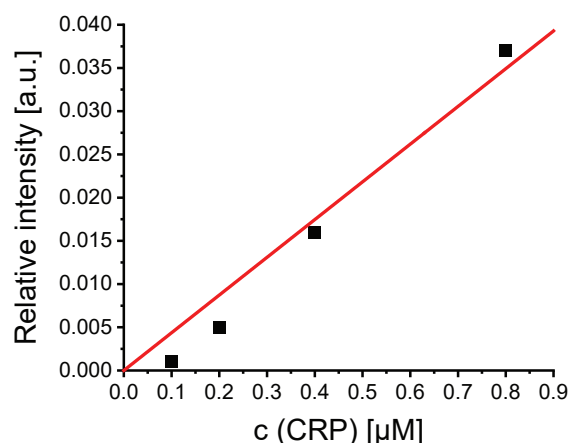
Figure 6.6. Calibration curve for CRP between 0.1 and 0.8 µM. Red line represents a linear fit curve starting from the origin, Pearson R = 0.99.

branes. Moreover the partition coefficient between CRP and the membrane containing oxidized PazePC was more than by a factor of two larger compared to pure POPC. This indicates that the higher partition of CRP to POPC/PazePC results in a distinguishable stiffening of the membrane.

Table 6.1. Partition coefficient P of CRP to lipid membranes coated on Si-beads in the absence and presence of 1 mM Ca^{2+}.

	POPC	POPC/PazePC
No Ca^{2+}	− 0.29	− 0.39
1 mM Ca^{2+}	0.45	1.02

6.4 Discussion

The non-enzymatic oxidation of unsaturated fatty acids is induced by reactive oxygen species (ROS), resulting in the formation of radicals leading to a sequential radical chain reaction.[178] Oxidized lipids are associated with several diseases including atherosclerosis[179], cancer[180], diabetes[181] and Alzheimer's disease.[182] The main organelles producing ROS *in vivo* are mitochondria, which harbor membranes containing polyunsaturated fatty acyl chains.[183] Even though the polyunsaturated chains are essential for mitochondrial functions, they are also prone to be attacked by ROS. In the vicinity of the mitochondrial membrane there is cytochrome c, which is on the one hand tightly bound to the membrane, inhibiting the formation of ROS, on the other hand there is cyt c loosely bound via electrostatic interactions associated with the generation of ROS proliferating cell apoptosis.[184] The peroxidation of the mitochondrial lipids leads to an increased permeability[185] and thus the tightly bound cyt c is released into the cytosol and can no longer inhibit the generation of ROS resulting in proliferation of apoptosis. In recent studies various oxidized end products could have been identified via electrospray mass spectroscopy coupled to reverse phase HPLC.[186] Several studies have demonstrated that oxidative stress can cause cell death.[187,188]Each cell is separated from other cells via the cell membrane where the lipids can get oxidized via lipid peroxidation influencing their biological activities via biophysical and biochemical activities of signalling molecules.[189] Previously it was reported that CRP on the one hand interacts with PC moieties, on the other hand Chang *et al.* showed that CRP binds to oxidized LDL and oxidized PC, but does not bind to non-oxidized LDL and PC.[42] During the last 20-30 years it was of significant interest to shed light on how the binding of CRP to membranes depends on the biophysical properties of the membranes. Borst *et al.* reported that lipid oxidation caused a decrease in membrane fluidity.[190] Other studies revealed via electron paramagnetic resonance (EPR) measurements and fluorescence microscopy imaging at the air/water interface that there is phase separation between oxidized PC and saturated matrix lipids like 1,2-dipalmitoyl-sn-glycero-3-phosphocholine (DPPC).[191][192] Pressure-area isotherms of oxidized lipids in DPPC as a matrix lipid indicate that at a critical pressure the oxidized lipids undergo a reordering process resulting in an extension of the alkyl chains into the bulk.[191] This so called "flipping" was proposed by molecular dynamic simulations and experimentally proven via fluorescence solvent relaxation experiments resulting in exposed negatively charged carboxy gropus to the outer surface.[175,193] These findings agree well with the results obtained from zeta potential measurements where the zeta potential for POPC/PazePC was negative in the absence of CRP supporting that the carboxy groups were flipped towards the outer surface resulting in an exposure of negative charges to the surface (see section 6.1). Makky *et al.*[44] further characterized

the structure of oxidized lipids via X-ray reflectivity (XRR) and Grazing incidence X-ray fluorescence (GIXF) measurements at the air/water interface while keeping the surface pressure constant at π = 20 mN/m. The area per molecule was successively increasing from non oxidized POPC (65 Å^2), PoxnoPC (95 Å^2) and PazePC (110 Å^2) indicating that the lateral packing is perturbed by the progression of chain oxidation. This leads to the plausible conclusion that the disturbance of the lipid membrane due to oxidized lipids plays a key role in the interaction between CRP and membranes. Korytowski[46] showed that the interaction between SUVs from oxidized PoxnoPC and PazePC leads to aggregate formation. Zeta potential data do not show a clear evidence that the interaction is modulated via electrostatic interactions as the aggregate formation occurs similar for PoxnoPC and PazePC while the zeta potential only shows a shift for PazePC. This shift therefore might be attributed due to the electrostatic screening of the negative charges by CRP. Makky *et al.*[44] proposed that the bending stiffness κ for membranes containing PazePC might decrease due to the reduced lateral packing. Indeed Flicker spectroscopy measurements (see section 6.2) could confirm a significantly lower κ for POPC/PazePC compared to pure POPC. Additionally, the binding which is mediated via Ca^{2+} stiffens the membranes containing oxidized PazePC, indicating that the oxidation of the alkyl chains and CRP binding influence the mechanical properties of apoptotic cell membranes.

7 Conclusions

In this thesis the modulation of wetting and mechanical properties of model cell membranes caused by the changes on the molecular levels was investigated by various physicochemical techniques.

In section 4 wetting of the substrates coated with bio-inspired, stimulus responsive polymer brushes by giant unilamellar vesicles was studied. In this study, pAA-Cys5 brushes inspired by the naturally occurring phytochelatin were used as the stimulus-responsive polymer material that changed the conformation by the selective capture of Cd^{2+} ions. Supported lipid membranes were used to achieve a well-defined, high surface density for the grafting of polymer brushes by using biotin-neutravidin crosslinks (Fig.4.8c)). In the first step, the structures of pAA-Cys5 brushes grafted onto supported lipid membranes were investigated by high energy specular X-ray reflectivity (XRR) measurements. The brushes were characterized in buffered saline solution (10 mM Tris, 100 mM Nacl, pH 7.4) in the absence and presence of $[Cd^{2+}]$ = 1.0 mM. The use of high energy X-ray (17 keV) enables the sufficiently high transmission of the X-ray beam through bulk water. The best fit results of the obtained XRR data demonstrated that the distinct switching of the polymer chain conformation was caused by the additional Cd^{2+} ions (Fig. 4.8e)). Compared to the brushes with no Cd^{2+} ions, the thickness of pAA-Cys5 brushes decreased from 13.9 ± 0.8 nm to 9.9 ± 1.2 nm ($\triangle d$ = 4.0 nm), accompanied by a decrease in the brush/buffer roughness from 2.1 ± 0.1 nm to 1.2 ± 0.1 nm and a slight increase in the scattering length density from $9.7 \pm 0.1 \times 10^{-6}$ $Å^{-2}$ to $9.9 \pm 0.1 \times 10^{-6}$ $Å^{-2}$, indicating a marked chain compaction. In the next step, the zwitterionic giant lipid vesicles (diameter $\approx$ 10 µm) were allowed to adhere onto the pAA-Cys5 brushes at different $[Cd^{2+}]$. The global shape of vesicle was reconstructed from the confocal fluorescence microscopy images (Fig. 4.10f-h)). The shape in the proximity of the adhesion contact was calculated from the microinterferometry images, because the shape near the membrane-water-substrate contact is dominated by the membrane elasticity (Fig.4.14). This enables to identify the onset of adhesion/wetting at $[Cd^{2+}]$ = 0.25 mM, which could not be detected otherwise. By taking the contribution of the membrane elasticity to the vesicle shape into account, the adhesion free energy was calculated: $\triangle \gamma_{W,0.25 \text{ mM}} \approx$ 24 $k_B T/µm^2$ at $[Cd^{2+}]$ = 0.25 mM , and $\triangle \gamma_{W,1.0 \text{ mM}} \approx$ 40 $k_B T/µm^2$ at $[Cd^{2+}]$ = 1.0 mM. As the microinterferometry techniques can precisely monitor the height fluctuation of the membranes with nm accuracy, the histogram of the membrane height fluctuations was recorded for 12 s ($\triangle t$ = 30 ms per frame). As the shape of the potential near the minimum can be approximated as a parabolic function, the potential curvature $V"$ was calculated by taking correlated membrane fluctuations into account. Remarkably, the difference of $V"$ for $[Cd^{2+}]$ = 0.25 mM and

86

$[Cd^{2+}]$ = 1.0 mM was significantly different yielding $V''_{0.25\,mM}$ = $(2.5 \pm 1.8) \times 10^{-6}$ $k_B T/nm^4$ and $V''_{1.0\,mM}$ = $(3.9 \pm 0.9) \times 10^{-6}$ $k_B T/nm^4$. The combination of experimental data and simulations enabled the quantitative calculation of effective interfacial potentials presented in (7.1).

$$V(\delta z) = -\Delta\gamma_\mathsf{W} + \frac{1}{2}V''\delta z^2 \qquad\qquad (7.1)$$

In section 5 the "dynamic switching" of the vesicle-brush interaction was investigated, where the transition from *non-wetting* to *wetting* was observed in real time with a time resolution of 30 ms. When the buffer was exchanged from Cd^{2+}-free buffer to Cd^{2+}-loaded buffer, the height fluctuation of the membrane near the center of the adhesion contact showed a distinct decay over time, indicating an increase in the potential confinement (Fig.5.1). To gain more insights into the dynamics of wetting transition, two laminar flows (one contains 1.0 mM Cd^{2+} and the other contains 10 mM EDTA) were mixed in a microfluidic channel. As shown in Fig. 5.3 the change in the vesicle contour during transition from "stop" (no movement) and "go" could be visualized by moving the boundary between two flows. In section 6 the influence of subtle changes in the molecular structures on the mechanical properties of giant vesicles was investigated. Here, the oxidation of phospholipids was selected as the change in molecular structures, because the lipid oxidation is one of the key steps in apoptosis and the following inflammatory response. As the binding of acute phase inflammatory C-reactive protein (CRP) to phosphatidylcholine lipids strongly depends on the degree of oxidation, the binding of CRP to the membranes containing lipids with different levels of chain oxidation (aldehyde and carboxylate) was monitored. The Fourier analysis of the membrane fluctuations, called flicker spectroscopy technique, revealed that the binding of CRP to the membrane containing PazePC (carboxylated lipid) caused an 1.5 fold increase in the bending ridigity κ (Fig. 6.2). In contrast, CRP hardly interacts with the vesicles with no oxidized lipids or alter the membrane elasticity, indicating that the decrease in the lateral packing caused by the lipid oxidation facilitates the binding of protein, resulting in the significant change in the bending rigidity.

To conclude, the obtained results demonstrate that the combination of various physico-chemical techniques can unravel how the subtle changes of the molecular structures, either the switching of the polymer chain conformation by a small amount of additives or the chemical oxidation of the hydrocarbon chain of a phospholipid, could modulate the macroscopic behaviors (wetting and adhesion) and mechanical properties of the cell membrane models.

8 Appendix

8.1 Influence of Benzalkonium chloride on corona virus model membranes probed by grazing incidence X-ray fluorescence

In section 8.1.1 a introduction is given, while in section 8.1.2 the basic principle of Grazing incidence X-ray fluorescence (GIXF) is explained and the experimental realization is shown in section 8.1.3}. The data analysis is explained in more detail in section 8.1.4 and the final results are presented in section 8.1.5.

8.1.1 Introduction

In February 2020 the world health organization announced a rapidly spreading corona virus disease (COVID-19) causing substantial morbidity and mortality worldwide.[194][195] On the molecular level lipid membranes play a key role for the spreading of the virus as the infection of a host cell by a corona virus occurs on the interface between the virus and the host cell membrane. The spike protein located on the virus membrane binds to the angiotensin converting enzyme 2 (ACE2) receptor on the host cell membrane.[196][197]Notably, to escape the human immune system the spike proteins are concealed by glycans.[198] After binding the spike protein is proteolytically cut by the transmembrane serine protease 2 (TMPRSS2), which is found in high amounts in respiratory cells.[199] The hydrophobic amino acid sequence of the cutted spike protein can enter the host cell membrane. Due to the spike protein folding back, the host cell membrane ruptures and the viral RNA is released into the cell.[200] This shows the importance of the viral membrane in order to infect a host cell. One strategy to destroy the viral membrane is due to contact with sanitizers. Previously it was reported that Benzalkonium chloride (BAC) might inactivate different types of viruses, e.g. the titer of the murine norovirus (MNV-1) could have been reduced below detectable levels.[201][202] During this study the influence of BAC on a corona virus model membrane was investigated. Therefore a corona virus model membrane containing POPC, POPE, POPS (70:15:15 mol%) was spread onto the air/water interface and incubated with various BAC concentrations reaching from 0.1 to 10 mM. After that the membrane structural parameters were characterized by conducting X-ray reflectivity (XRR) and Grazing incidence X-ray fluorescence (GIXF) measurements, where the layer parameters thickness d, scattering length density SLD and roughness σ for each layer can be obtained from XRR measurements, while the vertical concentration profile of ions can be extracted from GIXF measurements.[203][204]

8.1.2 Grazing incidence X-ray fluorescence measurements to determine ion concentration profile next to the interface

Grazing incidence X-ray fluorescence (GIXF) is a technique that enables to obtain element specific concentration profiles perpendicular to the interface by measuring the fluorescence signals at different angles of incidence.[205][206][207]
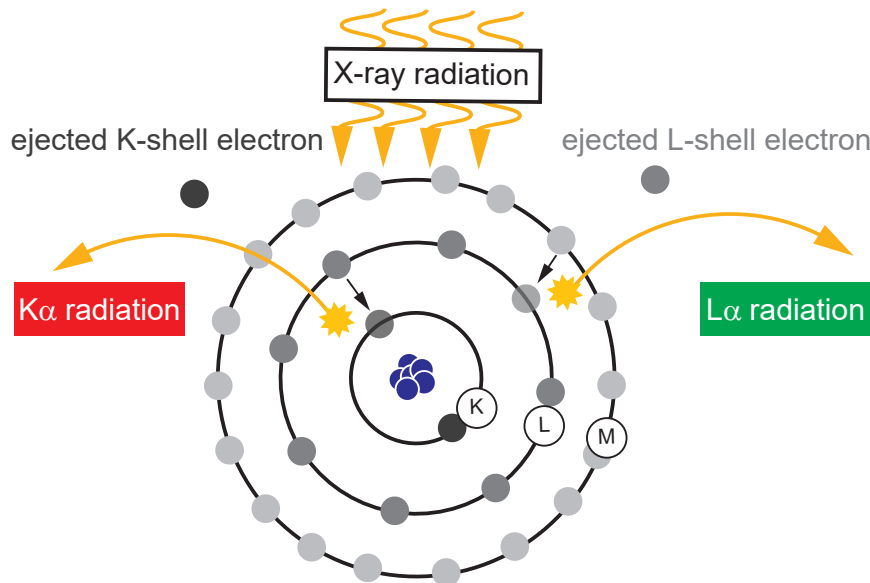
Figure 8.1. Interaction of X-ray radiation with matter.

Following Bohr's classical model for atoms an atom consists of a core and electrons located around it in different valence shells.[208] The inner shell is called K-shell followed by the L- and M-shell as depicted in figure 8.1. For this concept and the discovery of characteristic X-ray radiation for each element, Charles Barkla was honored with the Nobel prize in physics in 1917.[209] When a sample is radiated by X-rays the evanescent field is interacting with the valence electrons[210]. If the X-ray energy exceeds the binding energy of one of the inner shells (K,L) an electron gets released and filled by an electron of one of the higher shells. If the fill up of the K-shell occurs from the L-shell the radiation is called K_α radiation while if the L-shell shell is filled up by an electron from the M-shell the radiation is called L_α radiation. A transition from the M-shell to the K-shell is called K_β radiation. The β transition has higher energy but occurs much rarer compared to the α transitions.[211] That is why for the analysis in most cases the α transition is more feasible for the analysis. To get highly resolved information in about the interface in z-direction, X-rays need to penetrate it. The penetration depth of X-rays under grazing incidence can be calculated in dependence on the angle of incidence α_i as given in equation (8.1).[212]:

$$\Lambda(\alpha_i) = \frac{\lambda}{\sqrt{8}\pi} \left[\sqrt{(\alpha_i^2 - \alpha_c^2)^2 + 4\beta^2} - (\alpha_i^2 - \alpha_c^2) \right]^{-\frac{1}{2}} \tag{8.1}$$

β denotes the imaginary part of the refractive index (see equation (3.40)) and the wavelength of the X-ray radiation λ.

The fluorescence intensity $I_i^f(\alpha_i)$ of an element i at a distance z from the air-water interface can be described in dependence of the angle of incidence α_i resulting in equation (8.2).

$$I_i^f(\alpha) = S \int_0^\infty I^{ill}(z, \alpha) c_i(z) \exp(-\frac{z}{L_i}) dz \tag{8.2}$$

The attenuation length is denoted by L_i, which is 68.14 µm for potassium K_α radiation. S is a scaling constant which gets scaled out due to the normalization of the signal to the blank buffer. I^{ill} denotes the illumination profile and $c_i(z)$ the vertical concentration profile. The illumination profile is defined as the quadratic sum of the absolute value of the amplitudes of the incident- and reflected electric field waves, which are presented in equation (8.3).

$$I^{ill} = |E^+(z) + E^-(z)|^2 \tag{8.3}$$

$E^+(z)$ is the incident electric field wave yielding equation (8.4) and $E^-(z)$ is the reflected electric field wave given in equation (8.5).

$$E^+(z) = E_j^+ \exp(ik_{z,j})(z - \sum_{i=1}^{j-1} d_i) \tag{8.4}$$

$$E^-(z) = E_j^- \exp(ik_{z,j})(z - \sum_{i=1}^{j-1} d_i) \tag{8.5}$$

The thickness of the layer j is denoted by d_j, E_j^+ and E_j^- are the electric field amplitudes in layer j, with $k_j^z = \frac{2\pi}{\lambda} \sqrt{(\frac{q_z \lambda}{4\pi})^2 + n_j^2 - 1}$ and the refractive index of layer j is n_j. Thus the illumination profile can be obtained from fitting the corresponding X-ray reflectivity data which yield the thickness d_j and the scattering length density which is needed to calculate the complex refractive index according to equation (3.40).

The concentration profile $c_i(z)$ can be described by an asymmetric gaussian distribution yielding equation (8.6).[205]

$$c_i(z) = c_0 + c_{max} \frac{\sqrt{e}(z - z_0)}{z_{max}} \exp(\frac{(z - z_0)^2}{2z_{max}^2}) \tag{8.6}$$

where c_0 is the concentration in the bulk, z_0 is denoted as the alkyl chain - lipid head-

group interface and z_{max} is the position of the maximum concentration c_{max}. Accordingly, c_{max} and z_{max} are the only two fitting parameters to obtain an ion specific concentration profile along the z-axis orthogonal to the interface.

8.1.3 Experimental realization
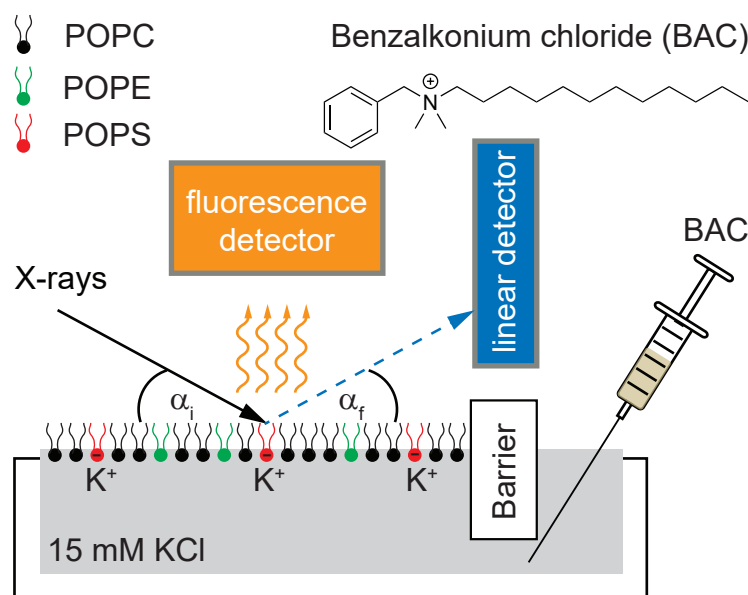
Figure 8.2. Experimental setup for simultaneous XRR and grazing incidence GIXF measurements. A monolayer consisting of 15 mol% negatively charged lipids representing a corona virus model membrane is used to monitor the influence of BAC, a commercial sanitizer, on the monolayer.

60 μl lipid stock solution with a final concentration of c = 1 mg/ml were spread drop wise to form a monolayer on the [KCl] = 15 mM subphase on a Langmuir filmbalance trough. Prior to each measurement the monolayer was compressed to a surface pressure of 25 mN/m. BAC was injected under the barrier to reach the desired final BAC concentrations in the bulk (0.1, 1, 5, 10 mM). A schematic illustration of the experimental set up is shown in figure 8.2. GIXF measurements were carried out at the European Synchrotron Radiation Facility (Grenoble, France) at the beamline ID10. The sample was irradiated with a monochromatic synchrotron beam with an energy of 13 keV ($\lambda \approx$ 0.95 Å). The Langmuir trough was held under He gas during all measurements to minimize scattering between fluorescence emission and air molecules. X-ray reflectivity signals were recorded with a linear Mythen 1K detector (Dectris, Switzerland) and were analyzed by using the MOTOFIT software package applying the Parratt formalism.[96] GIXF signals were collected with a Vortex detector (SII Nano Technology, USA). The element-specific fluorescence intensity spectra were normalized by the elastically scattered beam intensity to avoid systematic differences within experiments.

8.1.4 Data analysis

In figure 8.3a) typical GIXF spectra of the investigated lipids deposited onto the air/water interface below the critical angle at $\alpha = 0.03°$ (black) and above the critical angle at $\alpha = 0.2°$ (red) are shown. Both spectra show prominent peaks at 3.3 keV, which are attributed to the potassium K-K_α peaks, while below the critical angle the chloride Cl-K_α peak is less pronounced compared to the data above the critical angle, which correspond to the bulk. At an energy of 2.0 keV a new peak appeared which can be attributed to the phosphorous P-K_α line indicating phospholipids in the vicinity of the surface. In figure 8.3b) a zoom in on the K-K_α peak with the multiple Gaussian fitting is shown.
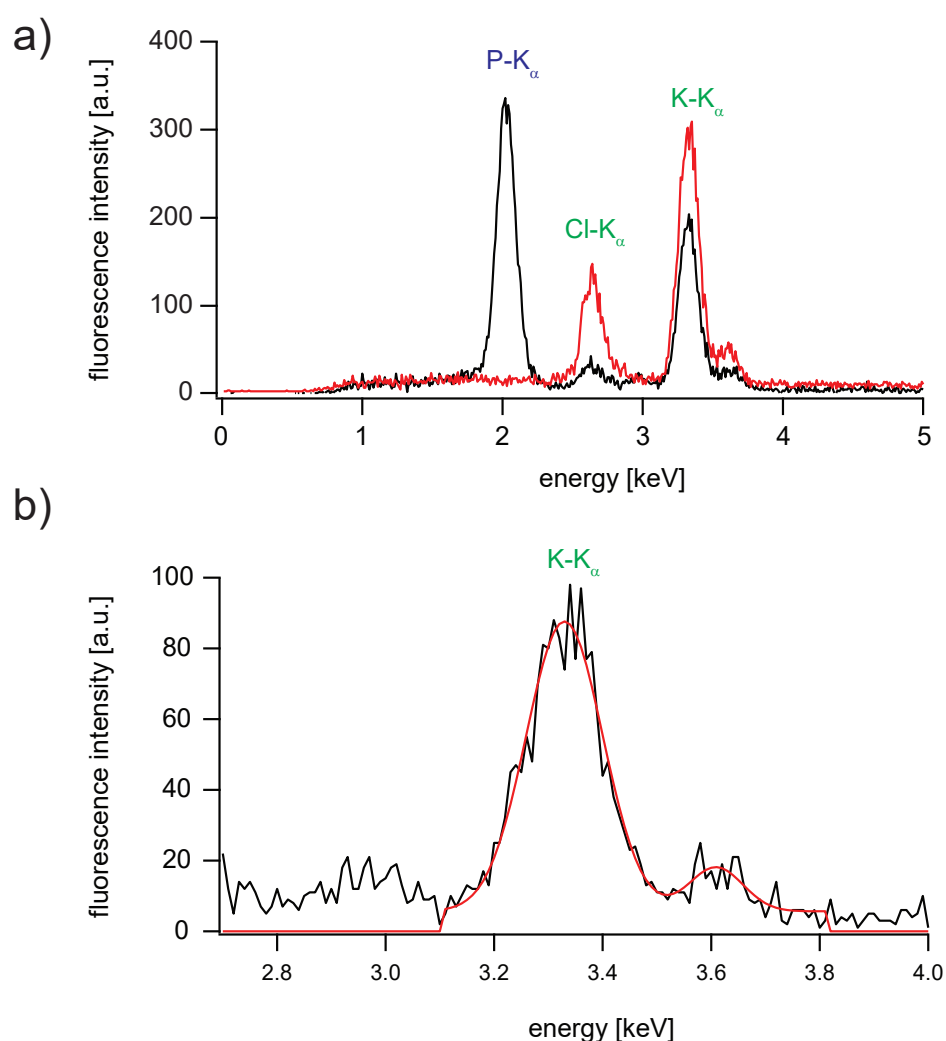
Figure 8.3. a) GIXF spectra below the critical angle at $\alpha = 0.05°$ (black line) and above at $\alpha = 0.20°$. b) Zoom in of characteristic K-K_α peak and multiple gaussian fitting (red) corresponding to a distinctive angle α.

In the next step the characteristic fluorescence intensity peaks are fitted for all angles from 0 to 0.3° and integrated over them yielding the intensity versus the angle α. In figure 8.4a) the corresponding intensities versus angle are plotted for the sample while

in figure 8.4b) the data for the pure 15 mM KCl buffer are shown. Normalization yields to the normalized GIXF spectra which were used for the analysis as presented in figure 8.4 (see section 8.1.5).
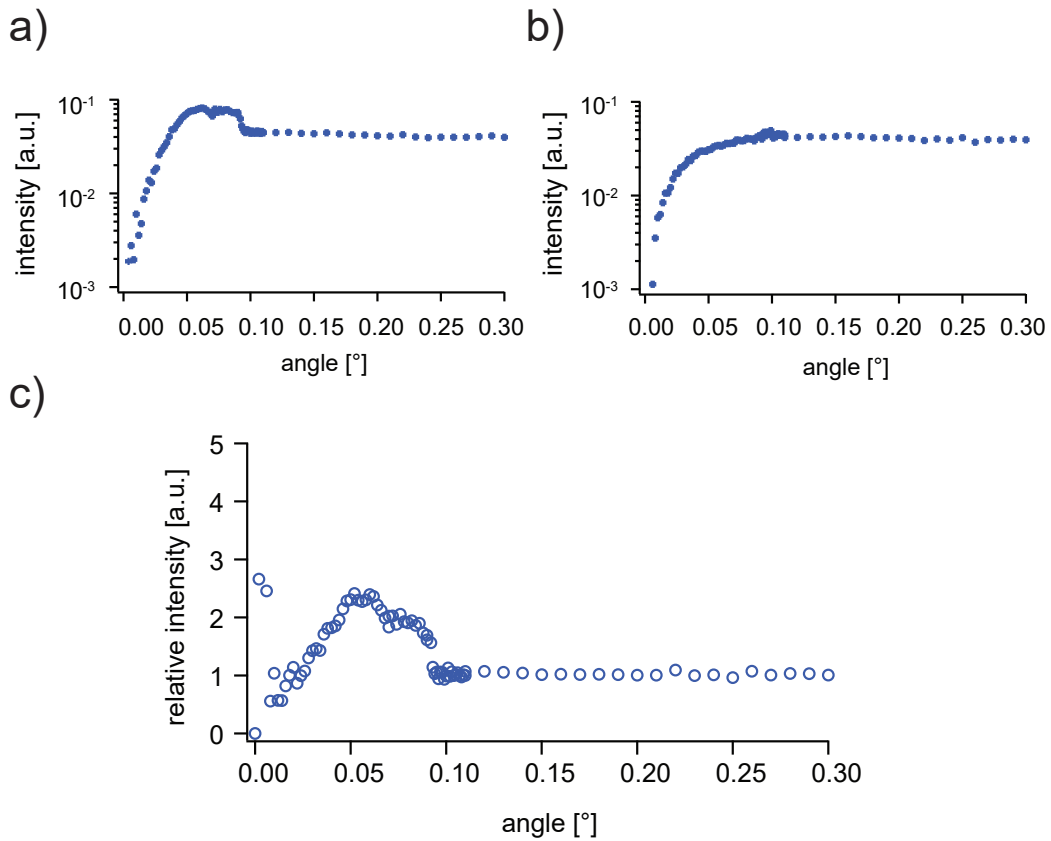
Figure 8.4. Fluorescence intensity of the sample (a) and the corresponding buffer (b). c) Normalized relative intensity versus angle obtained from a) and b)

8.1.5 Influence of cationic surfactants to corona viurs model membranes by screening different BAC concentrations

The influence of successively increasing BAC concentrations [BAC] = 0.1, 1, 5 and 10 mM on a corona virus model membrane (POPC, POPE, POPS = 70:15:15 mol %) are investigated. Figure 8.5a) shows the XRR curve of the corona virus model monolayer at the air/water interface before BAC injection. BAC was injected in the Langmuir trough having a final concentration of 0.1 mM and monitored at Δt = 30 and 90 min after BAC injection. The corresponding XRR data are presented in figure 8.5b) and 8.5c), respectively. Compared to the data before BAC injection, the global shapes of the XRR curves look similar indicating an unspoiled membrane showing one minimum below 0.3 q. The black solid lines correspond to the best fit results applying a two layer slab model at the air/water interface consisting of alkyl chains and headgroups as the two individual layers. The data were well fitted and the resulting layer parameters (thickness d, SLD and roughness σ) are presented in table 8.1. The average thickness of the monolayer is $\approx$ 22 Å which is in good agreement with previous XRR and neutron reflectivity (NR) measurements.[44][213] The corresponding reconstructed SLD profiles are shown in figure 8.5d). To investigate the influence of BAC on the potassium ion distribution perpendicular to the interface the potassium Kα line was measured by GIXF and plotted versus q (see figure 8.5e-f). The signals below the critical angle q_c = 0.022 Å^{-1} represent the potassium ions K$^+$ in the vicinity of the interface while the signal above the critical angle displays K$^+$ in the bulk. Before BAC injection a clear increase regarding the relative intensity below the critical angle indicating accumulation of K$^+$ near the interface (figure 8.5e). For the data at Δt = 30 min after BAC injection the same trend as for the data before BAC can be observed, but the relative intensity below the critical angle is much lower suggesting less accumulation of K$^+$ in the vicinity of the interface (figure 8.5f). The black lines represent the best fit results. 90 min after BAC injection the data can not be fitted indicating that BAC replaces K$^+$ next to the interface (figure 8.5g). In figure 8.5h) the corresponding K$^+$ distribution profiles obtained from the best fit results are presented. Before BAC injection the average number of K$^+$ per lipid is around 0.19. This experimental result is in good agreement considering theoretically 15 mol% of charged lipids (1-palmitoyl-2-oleoyl-sn-glycero-3-phospho-L-serine (POPS)) in the monolayer. At Δt = 30 min after BAC injection the fit yields only 0.07 K$^+$ per lipid and at Δt = 90 min after BAC injection the data cannot be fitted, indicating a successive depletion of [K$^+$]. The position of maximum concentration Z_{max} with respect to the interface decreases from 25.3 Å before BAC to 16.4 Å at Δt = 30 min after BAC injection. This shows a stepwise depletion of K$^+$ from the monolayer suggesting that BAC adsorbs to the interface.

Next, the BAC concentration was increased to a final concentration of [BAC] = 1 mM in

Figure 8.5. Influence of [BAC] = 0.1 mM on the stability of the monolayer. XRR data before BAC injection (a) and after Δt = 30 min (b) and 90 min (c). The black line represents the best fit, resulting parameters are presented in table 8.1. Reconstructed SLD profiles (d) of the monolayers corresponding to all three conditions. GIXF data before BAC injection (e) and after Δt = 30 min (f) and 90 min (g). Data presented only in symbols (g) could not be fitted, due to the depletion of ions from the interface, bulk intensity indicated by broken line. Corresponding ion density profiles (h) in the vicinity of the monolayer calculated with equation (8.6).

the subphase. Figure 8.6a-c) show the corresponding XRR data for the monolayer before BAC injection and for Δt = 30 min and 90 min after BAC injection, where the global shapes of the curves and positions of the minima look similar to [BAC] = 0.1 mM shown in figure 8.5a-c). The black line represents the best fit results applying a two layer slab model, where the respective layer parameters are presented in table 8.2. In figure

Table 8.1. Thickness d, scattering length density SLD and roughness σ corresponding to the best fit results of XRR data (blackk solid lines in figure 8.5 a-c) of a corona virus model monolayer in the absence and presence of [BAC] = 0.1 mM at different time points after BAC injection ($\triangle$t = 30 min and 90 min).

	d (Å)	SLD (10^{-6}Å^{-2})	σ (Å)
before BAC			
alkyl chain	11.31 ± 0.12	6.76 ± 0.42	3.71 ± 0.10
headgroup	10.21 ± 0.14	12.06 ± 0.42	3.24 ± 0.13
buffer	∞	9.45	3.23 ± 0.15
$\triangle$ t = 30 min			
alkyl chain	12.63 ± 0.27	7.09 ± 0.79	4.42 ± 0.26
headgroup	10.11 ± 0.74	12.20 ± 0.64	4.19 ± 0.50
buffer	∞	9.45	3.48 ± 0.35
$\triangle$ t = 90 min			
alkyl chain	12.63 ± 0.42	7.21 ± 0.80	4.45 ± 0.33
headgroup	9.48 ± 0.65	12.31 ± 0.46	4.36 ± 0.36
buffer	∞	9.45	3.72 ± 0.36

8.6d) an overlay of the obtained SLD profiles from the best fits are presented. The GIXF data before BAC injection presented in figure 8.6e) show a similar global shape compared to the data in the presence of 0.1 mM BAC shown in figure 8.5e-f). The black line corresponds to the best fit result which yields 0.14 BAC molecules per lipid and a maximum concentration at Z_{max} = 21.6 Å before BAC injection. The parameters are in good agreement with the data before BAC injection at [BAC] = 0.1 mM (8.5e). From $\Delta t \geq 30$ min the data can not be fitted anymore (see figure 8.6f-g) indicating a faster depletion of [K$^+$] due to a higher BAC concentration.

The XRR curves before and after BAC injection for [BAC] = 5 mM are shown in 8.7a-c). Their global shape looks similar to the curves for [BAC] = 0.1 and 1 mM giving a distinctive minimum below 0.3 q. The black line corresponds to the best fit results. The resulting layer parameters are presented in table 8.3. Figure 8.7d) depicts the SLD profiles reconstructed from the layer parameters. At Δt = 90 min after BAC injection the SLD of the headgroup/chain interface decreases which indicates a decrease in the packing density of the headgroups. Also Thoma *et al.*[214] found that in case of negatively charged saccharide head groups BAC also leads to an decrease in SLD of the headgroup/chain interface due to binding of positively charged BAC. In figure
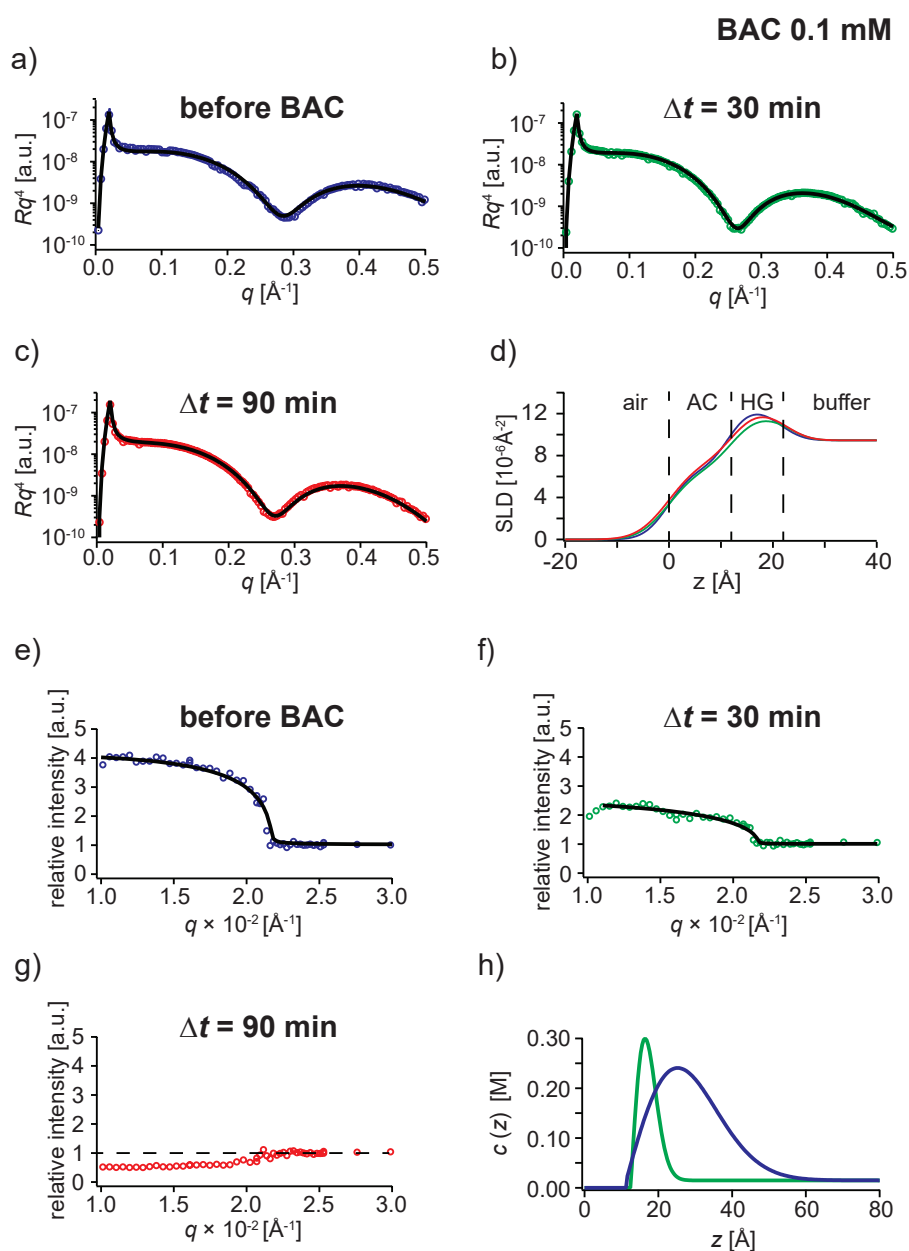
Figure 8.6. Influence of [BAC] = 1 mM on the stability of the monolayer. XRR data before BAC injection (a) and after Δt = 30 min (b) and 90 min (c). The black line represents the best fit, resulting parameters are presented in table 8.2. Reconstructed SLD profiles (d) of the monolayers corresponding to all three conditions. GIXF data before BAC injection (e) and after Δt = 30 min (f) and 90 min (g). Data presented only in symbols (g) could not be fitted, due to the depletion of ions from the interface, bulk intensity indicated by broken line. Corresponding ion density profiles (h) in the vicinity of the monolayer calculated with equation (8.6).

8.7e-g) the respective GIXF data are presented, which show a similar trend such as the GIXF data for [BAC] = 1 mM. The black line represents the best fit result before BAC injection yielding the average number of K^+ per lipid as 0.18 which is in good agreement to a monolayer containing 15 mol% negatively charged lipids (POPS). In figure 8.7h) the position of maximum concentration Z_{max} and the concentration profile

Table 8.2. Thickness d, scattering length density SLD and roughness σ corresponding to the best fit results of XRR data (black solid lines in figure 8.6 a)-c) of a corona virus model monolayer in the absence and presence of [BAC] = 1 mM at different time points after BAC injection ($\triangle$t = 30 min and 90 min).

	d (Å)	SLD (10^{-6}Å^{-2})	σ (Å)
before BAC			
alkyl chain	11.77 ± 0.13	6.25 ± 0.78	3.47 ± 0.32
headgroup	9.56 ± 0.46	12.23 ± 0.42	3.92 ± 0.41
buffer	∞	9.45	3.18 ± 0.14
$\triangle$ t = 30 min			
alkyl chain	11.79 ± 0.17	6.21 ± 0.74	3.99 ± 0.31
headgroup	9.10 ± 0.46	12.51 ± 0.38	4.17 ± 0.35
buffer	∞	9.45	3.97 ± 0.26
$\triangle$ t = 90 min			
alkyl chain	11.22 ± 0.28	7.56 ± 0.63	4.12 ± 0.38
headgroup	9.39 ± 0.57	12.34 ± 0.51	4.08 ± 0.58
buffer	∞	9.45	3.62 ± 0.30

$c(z)$ are shown. Z_{max} = 26.9 Å before BAC injection results in similar positions of the maximum concentration compared to [BAC] = 0.1 and 1 mM.

The BAC concentration was increased to [BAC] = 10 mM. The global shapes of XRR curves are presented in figure 8.8a-c) and are consistent with the previous XRR data showing a minimum below 0.3 q before BAC injection and at Δt = 30 min after BAC injection.

The data at Δt = 90 min after BAC injection in contrast show a minimum shifted to higher q values and a less pronounced minimum indicating a decrease in layer thickness d and a disturbance of the monolayer due to [BAC] = 10 mM. Indeed, the analysis of the best fit results (black solid lines) reveals a decrease of the monolayer thickness d at Δt = 90 min after BAC injection of approximately 2 Å. In figure 8.8d) an overlay of the respective SLD profiles is presented. Table 8.4 gives an overview over the layer parameters obtained from the best fit results (solid black lines).

The respective GIXF data before BAC injection show an increase in intensity (figure 8.8e) while the K$^+$ signal for the data at Δt = 30 and 90 min after BAC injection is depleted (figure 8.8f-g). Under the assumption of 15 mol% negatively charged POPS lipids fitting the data revealed an average of 0.07 K$^+$ per lipid, which is a factor of two
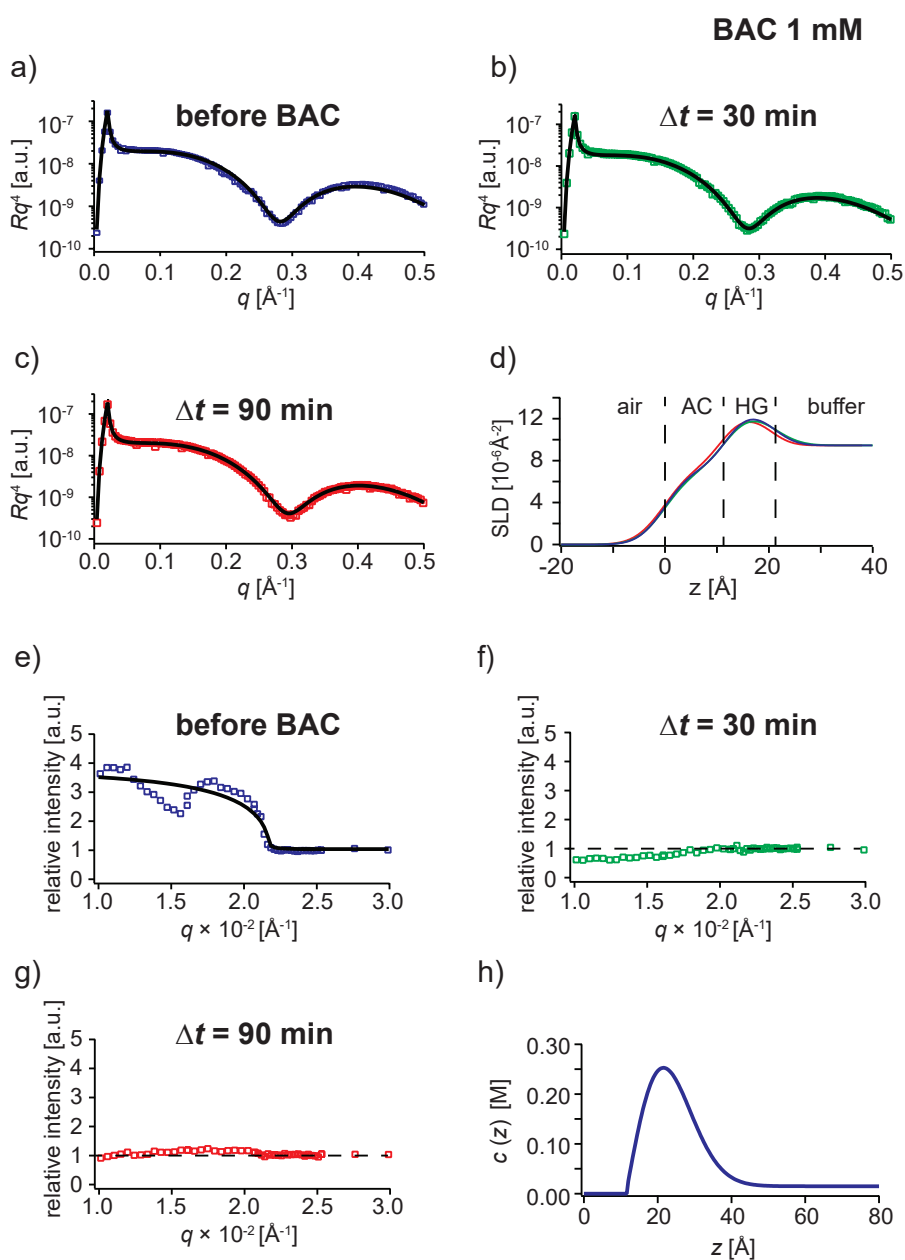
Figure 8.7. Influence of [BAC] = 5 mM on the stability of the monolayer. XRR data before BAC injection (a) and after Δt = 30 min (b) and 90 min (c). The black line represents the best fit, resulting parameters are presented in table 8.3. Reconstructed SLD profiles (d) of the monolayers corresponding to all three conditions. GIXF data before BAC injection (e) and after Δt = 30 min (f) and 90 min (g). Data presented only in symbols (g) could not be fitted, due to the depletion of ions from the interface, bulk intensity indicated by broken line. Corresponding ion density profiles (h) in the vicinity of the monolayer calculated with equation (8.6).

lower than expected. The position of maximum concentration before BAC injection can be obtained from the maximum of the fit in figure 8.8h (Z_{max} = 17.2 Å). These data provide an initial indication that [BAC] = 10 mM is able to disrupt the corona virus model membrane

The intensity of the GIXF phosphorous K_α peak is directly correlated to the amount of

Table 8.3. Thickness d, scattering length density SLD and roughness σ corresponding to the best fit results of XRR data (blackk solid lines in figure 8.7 a)-c) of a corona virus model monolayer in the absence and presence of [BAC] = 5 mM at different time points after BAC injection ($\triangle$t = 30 min and 90 min).

	d	SLD	σ
	(Å)	(10^{-6}Å^{-2})	(Å)
		before BAC	
alkyl chain	11.60 ± 0.10	6.29 ± 0.22	3.55 ± 0.10
headgroup	9.20 ± 0.10	12.57 ± 0.18	3.87 ± 0.10
buffer	∞	9.45	3.10 ± 0.09
		$\triangle$ t = 30 min	
	d	SLD	σ
	(Å)	(10^{-6}Å^{-2})	(Å)
alkyl chain	11.02 ± 0.34	6.08 ± 0.44	3.96 ± 0.18
headgroup	9.57 ± 0.70	13.20 ± 0.43	4.64 ± 0.38
buffer	∞	9.45	3.42 ± 0.23
		$\triangle$ t = 90 min	
	d	SLD	σ
	(Å)	(10^{-6}Å^{-2})	(Å)
alkyl chain	11.52 ± 0.23	7.08 ± 0.65	4.26 ± 0.33
headgroup	9.85 ± 0.47	11.86 ± 0.55	3.98 ± 0.39
buffer	∞	9.45	3.43 ± 0.34

lipids on the surface due to the fact that each lipid head group contains one phosphate moiety as can be seen from their molecular structures in figure 2.1. According to the GIXF spectra below the critical angle α = 0.03° (black solid line) and above the critical angle α = 0.2° (red solid line) presented in figure 8.3a) a peak at 2.0 keV occurs, which can be attributed to the P-K$_\alpha$ peak.
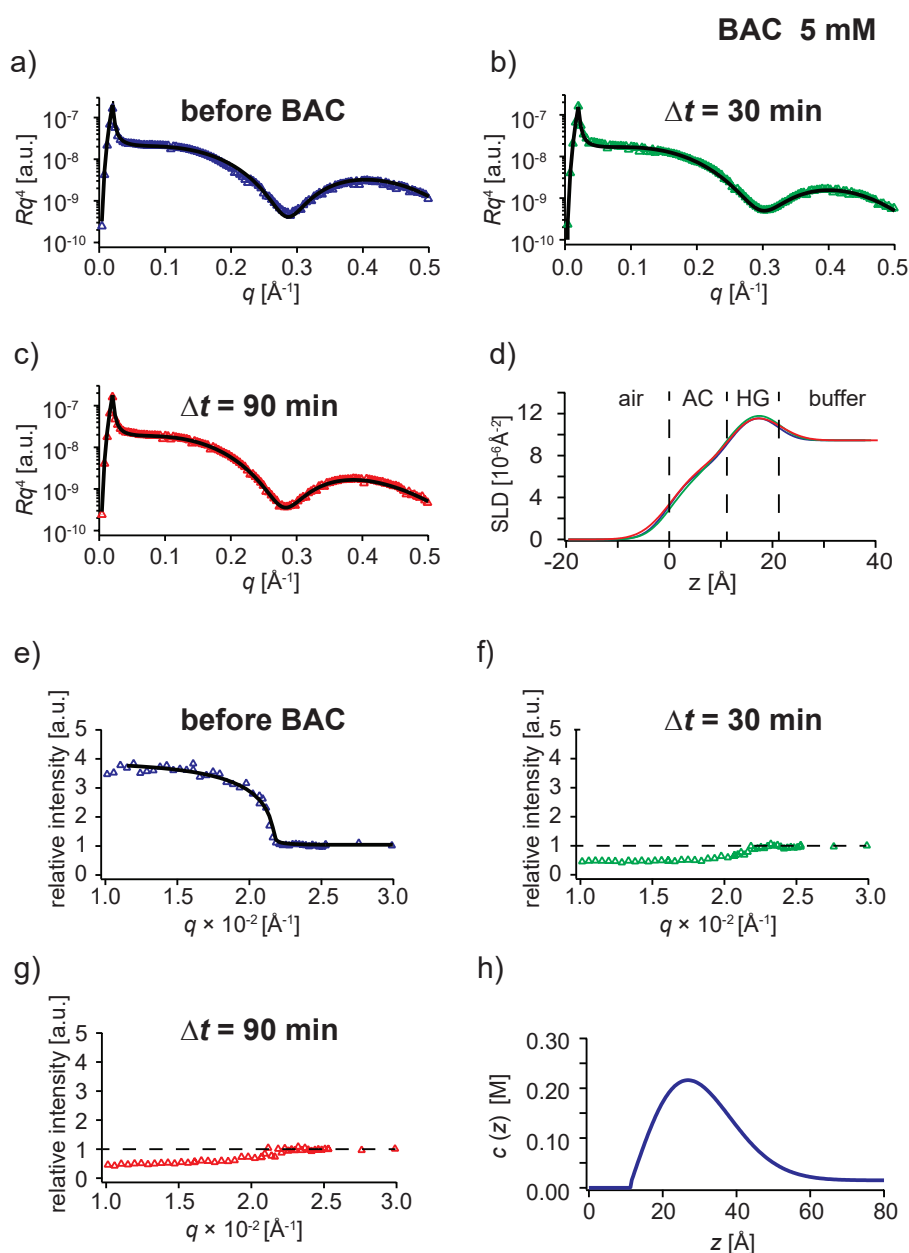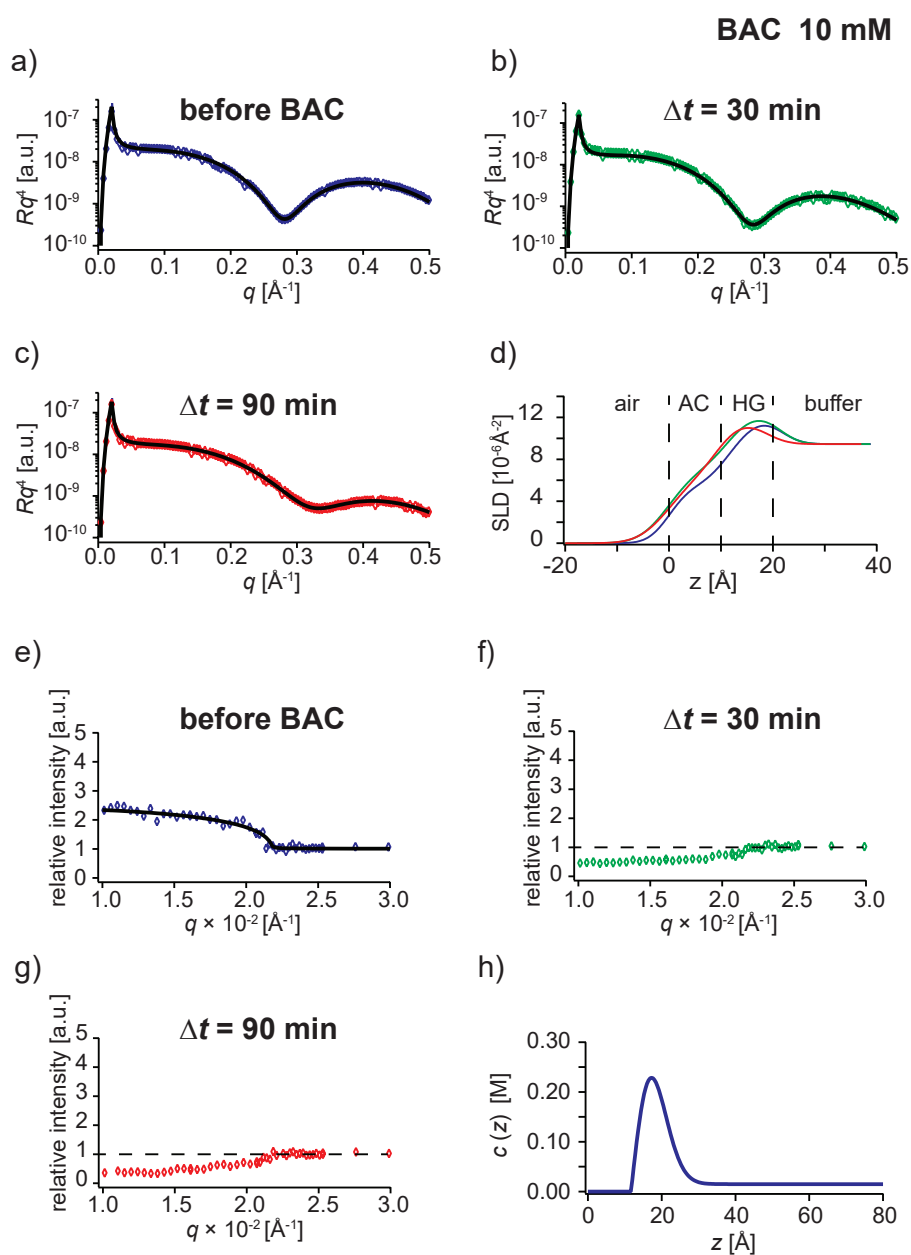
Figure 8.8. Influence of [BAC] = 10 mM on the stability of the monolayer. XRR data before BAC injection (a) and after Δt = 30 min (b) and 90 min (c). The black line represents the best fit, resulting parameters are presented in table 8.4. Reconstructed SLD profiles (d) of the monolayers corresponding to all three conditions. GIXF data before BAC injection (e) and after Δt = 30 min (f) and 90 min (g). Data presented only in symbols (g) could not be fitted, due to the depletion of ions from the interface, bulk intensity indicated by broken line. Corresponding ion density profiles (h) in the vicinity of the monolayer calculated with equation (8.6).

This supports the XRR data presented above, which show the formation of a lipid monolayer at the air/water interface. In figure 8.9 the relative fluorescence intensity of the phosphorous K_α peak is monitored for [BAC] = 0.1, 1, 5 and 10 mM before and 90 min after BAC injection. In figure 8.9a) the relative fluorescence intensity at [BAC] = 0.1 mM is plotted versus q. The data before BAC injection (left panel) and

Table 8.4. Thickness d, scattering length density SLD and roughness σ corresponding to the best fit results of XRR data (blackk solid lines in figure 8.8 a)-c) of a corona virus model monolayer in the absence and presence of [BAC] = 10 mM at different time points after BAC injection ($\triangle$t = 30 min and 90 min).

	d (Å)	SLD (10^{-6}Å^{-2})	σ (Å)
before BAC			
alkyl chain	11.88 ± 0.10	6.05 ± 0.70	3.43 ± 0.32
headgroup	9.56 ± 0.21	12.44 ± 0.27	3.95 ± 0.38
buffer	∞	9.45	3.19 ± 0.13
$\triangle$ t = 30 min			
alkyl chain	11.57 ± 0.21	6.74 ± 0.64	4.02 ± 0.28
headgroup	9.86 ± 0.54	12.36 ± 0.38	4.24 ± 0.38
buffer	∞	9.45	3.64 ± 0.32
$\triangle$ t = 90 min			
alkyl chain	9.64 ± 0.31	6.77 ± 1.05	3.92 ± 0.35
headgroup	9.78 ± 0.98	11.38 ± 0.61	4.08 ± 0.58
buffer	∞	9.45	4.06 ± 0.42

90 min after it (right panel) look similar indicating no significant change in the phosphorous concentration [P] in the vicinity of the surface. The same tendency can be observed for [BAC] = 1 mM and [BAC] = 5 mM as shwon in figures 8.9b) and 8.9c). For [BAC] = 10 mM the relative fluorescence intensity before BAC injection is similar to the intensities obtained for [BAC] = 0.1, 1 and 5 mM, while the fluorescence intensity after 90 min decreased significantly showing that [P] in the vicinity of the surface decreased, which is in good agreement with XRR data from figure 8.8c).
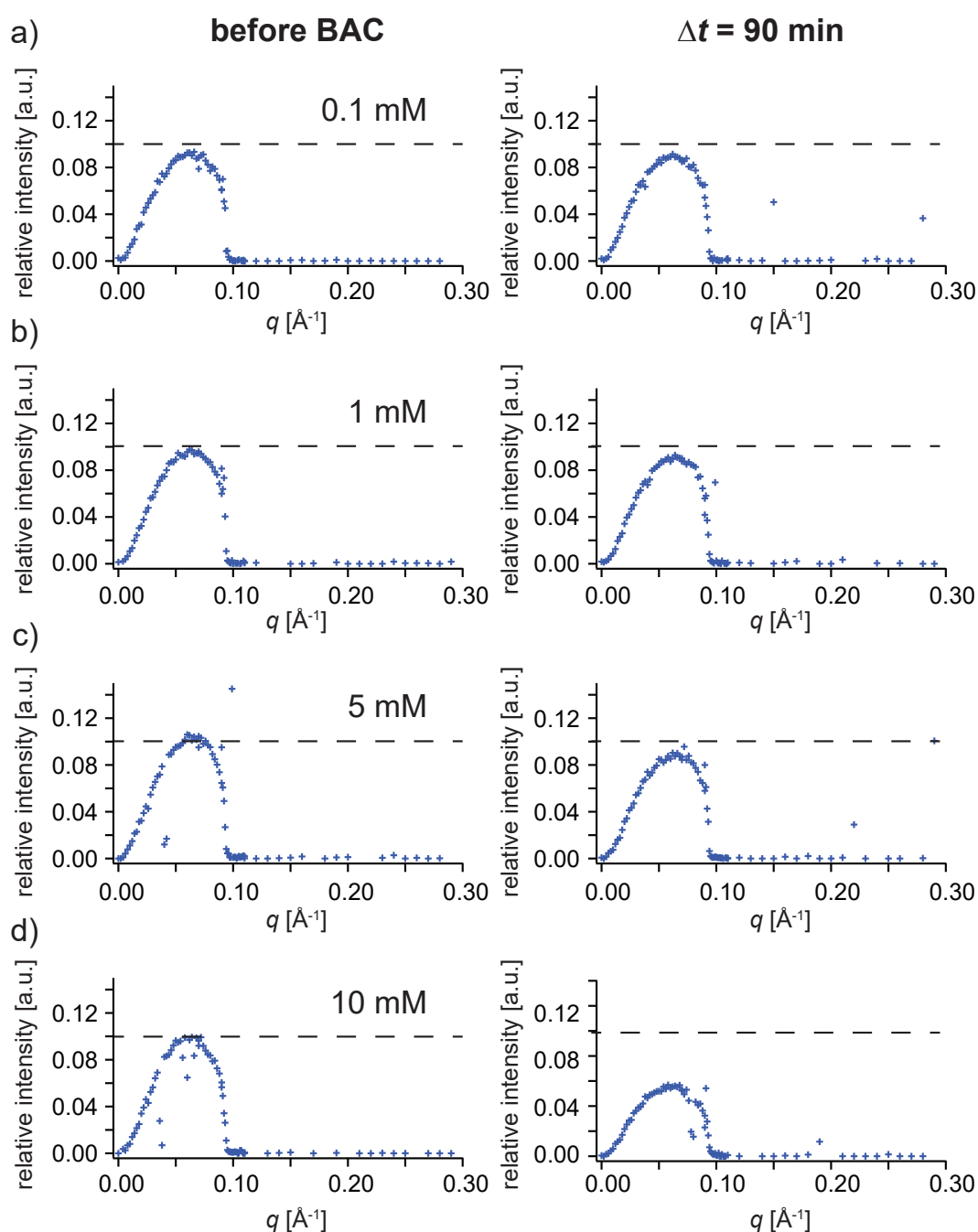
Figure 8.9. Relative intensity of phosphorous K_{α} peak versus q obtained from GIXF measurements. a) data at [BAC] = 0.1 mM before BAC injection (lef panel) and after Δt = 90 min after BAC injection. b) data at [BAC] = 1 mM before BAC injection (lef panel) and after Δt = 90 min after BAC injection. c) data at [BAC] = 5 mM before BAC injection (lef panel) and after Δt = 90 min after BAC injection. d) data at [BAC] = 10 mM before BAC injection (lef panel) and after Δt = 90 min after BAC injection. The black dashed line functions as a guidance for the eyes.

8.2 Discussion

Since the outbreak of the corona virus pandemic there was an high demand on COVID-19 research leading to more than 16.000 publications during the first few months.[215] There are several viable strategies to minimize the spreading of the infection such as wearing face masks, reducing social contact, regularly hand washing with soap and using sanitizers.[216] BAC is a well established sanitizer known to be effective against bacteria including S. aureus, a common skin contaminant.[217] Hirose *et al.* probed the effectiveness of BAC against COVID-19 on a skin model showing that relatively low [BAC] of 0.2 % might be effective against COVID-19, while expecting a longer disinfectant duration.[218] However, the skin model used within the study might overestimate the effectiveness showing that further investigations are needed. In previous accounts the influence of BAC on the structure of Gram-negative bacteria models was investigated by simultaneously XRR and GIXF measurements on the air/water interface, as antimicrobial resistance becomes a major thread in public health.[214] The combination of these both techniques is the only method to determine the vertical ion distribution perpendicular to the interface.[205][206] Interestingly, surface potential measurements of lipid monolayers revealed a change in the surface potential when poly(ethylene glycole) was added to the bulk, suggesting that it is surface active.[219] In this study the combination of XRR and GIXF shed light on the potassium ion distribution in the vicinity of the corona virus model membrane under different [BAC] monitored over a time of 90 min. Although GIXF data show depletion of $[K^+]$ for [BAC] $\geq$ 1 mM, indicating that BAC adsorbed to the interface, XRR data show that the monolayer only is disturbed at [BAC] = 10 mM, which is supported by the data of the phosphorous P-K_α peak showing a decrease in relative intensity of GIXF data at [BAC] = 10 mM. The average thickness for the alkyl chain and head group $\langle d_{chain} \rangle$ = 11.6 Å respectively $\langle d_{head\ group} \rangle$ = 9.6 Å is in good agreement with previous neutron reflectivity studies at the air/water interface and XRR measurements of a POPC bilayer where a total thickness of 21.0 Å respectively 22.1 Å was found, suggesting a reliable fit of XRR data.[213][44]

8.3 Determination of distortion factor for confocal side view images

Probing samples via confocal microscopy on oil immerison objectives with an refractive index in the sample chamber n_{sample} and an refractive index of the immersion oil n_{oil} leads to artificially distorted images. The distortion factor can be calculated following equation (8.7).[220]

$$\frac{d'}{d} = \frac{tan(sin^{-1}\frac{0.5NA}{n_{\text{sample}}})}{tan(sin^{-1}\frac{0.5NA}{n_{\text{oil}}})} \tag{8.7}$$

The expected focal position is denoted as d while the actual focal position is denoted as d'. Implementing the refractive indices of the sample solution n_{sample} = 1.34 and immersion oil n_{oil} = 1.52 into account and the numerical aperture of 1.40 of the used microscope NA yields a theoretical distortion factor of 0.52 according to equation (8.7). The distortion factor used during this study was determined by probing fluorescently labeled latex beads. In figure 8.10a) the confocal bottom view of the beads is shown with the indicated line profile (dashed white line), while the corresponding intensity profile is presented in figure 8.10b). In figure 8.10c) the binarized confocal side view is shown. Fitting the side view as an ellipse, while knowing that the spheres are round, enables to calculate the distortion factor via minor axis x over the major axis y resulting in a circle as presented in 8.10d) yielding within this study a correction factor of 0.64 $\pm$ 0.02 (n = 6).
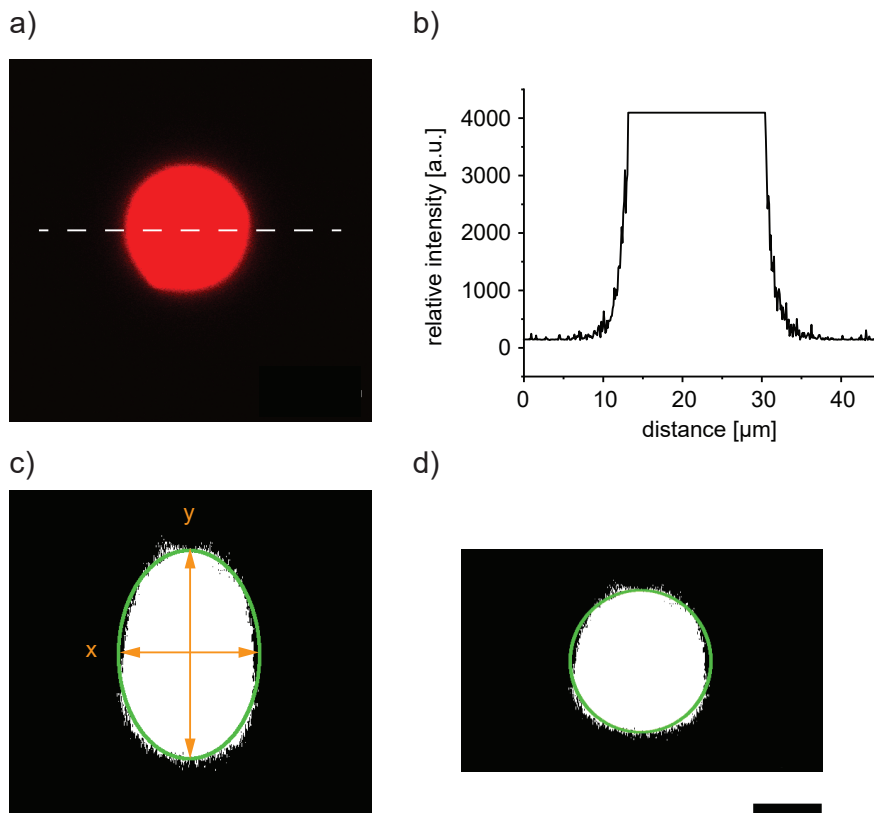
Figure 8.10. Determination of distortion factor of confocal side view images. a) confocal bottom view; b) corresponding line profile; c) binarized confocal side view; d) corrected bead; scale bar is 10 μm.

References

[1] Sackmann, E.; Tanaka, M. Critical role of lipid membranes in polarization and migration of cells: a biophysical view. *Biophysical Reviews* **2021**, *13*, 123–138.

[2] Molnar, C.; Gair, J. *Concepts of biology*; BCcampus, 2015.

[3] Singer, S. J.; Nicolson, G. L. The Fluid Mosaic Model of the Structure of Cell Membranes: Cell membranes are viewed as two-dimensional solutions of oriented globular proteins and lipids. *Science* **1972**, *175*, 720–731.

[4] Israelachvili, J. The science and applications of emulsions—an overview. *Colloids and Surfaces A: Physicochemical and Engineering Aspects* **1994**, *91*, 1–8.

[5] Tadros, T. F. Encyclopedia of colloid and interface science. *(No Title)* **2013**,

[6] Rosen, M. J. The relationship of structure to properties in surfactants. IV. Effectiveness in surface or interfacial tension reduction. *Journal of Colloid and Interface Science* **1976**, *56*, 320–327.

[7] Israelachvili, J. N.; Mitchell, D. J.; Ninham, B. W. Theory of self-assembly of hydrocarbon amphiphiles into micelles and bilayers. *Journal of the Chemical Society, Faraday Transactions 2: Molecular and Chemical Physics* **1976**, *72*, 1525–1568.

[8] Damodaran, K.; Merz Jr, K. M. Head group-water interactions in lipid bilayers: a comparison between DMPC-and DLPE-based lipid bilayers. *Langmuir* **1993**, *9*, 1179–1183.

[9] Sackmann, E.; Merkel, R. *Lehrbuch der Biophysik*; Wiley-VCH Weinheim, 2010.

[10] Wolfenden, R. Waterlogged molecules. *Science* **1983**, *222*, 1087–1093.

[11] Siegel, D. Inverted micellar intermediates and the transitions between lamellar, cubic, and inverted hexagonal lipid phases. I. Mechanism of the L alpha—-HII phase transitions. *Biophysical journal* **1986**, *49*, 1155–1170.

[12] Gulik-Krzywicki, T.; Tardieu, A.; Luzzati, V. The smectic phase of lipid-water systems: properties related to the nature of the lipid and to the presence of net electrical charges. *Molecular Crystals* **1969**, *8*, 285–291.

[13] Moser, M.; Marsh, D.; Meier, P.; Wassmer, K.; Kothe, G. Chain configuration and flexibility gradient in phospholipid membranes. Comparison between spin-label electron spin resonance and deuteron nuclear magnetic resonance, and identification of new conformations. *Biophysical Journal* **1989**, *55*, 111–123.

[14] Kaasgaard, T.; Leidy, C.; Crowe, J. H.; Mouritsen, O. G.; Jørgensen, K. Temperature-controlled structure and kinetics of ripple phases in one-and two-component supported lipid bilayers. *Biophysical journal* **2003**, *85*, 350–360.

[15] Leadbetter, A.; Frost, J.; Mazid, M. Interlayer correlations in smectic B phases. *Journal de Physique Lettres* **1979**, *40*, 325–329.

[16] Sackmann, E. Physical basis of self-organization and function of membranes: physics of vesicles. *Handbook of biological physics* **1995**, *1*, 213–304.

[17] Helfrich, W. Elastic properties of lipid bilayers: theory and possible experiments. *Zeitschrift für Naturforschung c* **1973**, *28*, 693–703.

[18] Seifert, U.; Lipowsky, R. Adhesion of vesicles. *Physical Review A* **1990**, *42*, 4768.

[19] Elosegui-Artola, A.; Oria, R.; Chen, Y.; Kosmalska, A.; Pérez-González, C.; Castro, N.; Zhu, C.; Trepat, X.; Roca-Cusachs, P. Mechanical regulation of a molecular clutch defines force transmission and transduction in response to matrix rigidity. *Nature cell biology* **2016**, *18*, 540–548.

[20] Kanai, F.; Marignani, P. A.; Sarbassova, D.; Yagi, R.; Hall, R. A.; Donowitz, M.; Hisaminato, A.; Fujiwara, T.; Ito, Y.; Cantley, L. C.; others TAZ: a novel transcriptional co-activator regulated by interactions with 14-3-3 and PDZ domain proteins. *The EMBO journal* **2000**,

[21] Heisenberg, C.-P.; Bellaïche, Y. Forces in tissue morphogenesis and patterning. *Cell* **2013**, *153*, 948–962.

[22] Bell, G. I.; Dembo, M.; Bongrand, P. Cell adhesion. Competition between nonspecific repulsion and specific bonding. *Biophysical journal* **1984**, *45*, 1051–1064.

[23] Yoshikawa, H. Y.; Kawano, T.; Matsuda, T.; Kidoaki, S.; Tanaka, M. Morphology and adhesion strength of myoblast cells on photocurable gelatin under native and non-native micromechanical environments. *The Journal of Physical Chemistry B* **2013**, *117*, 4081–4088.

[24] Purrucker, O.; Gönnenwein, S.; Förtig, A.; Jordan, R.; Rusp, M.; Bärmann, M.; Moroder, L.; Sackmann, E.; Tanaka, M. Polymer-tethered membranes as quantitative models for the study of integrin-mediated cell adhesion. *Soft Matter* **2007**, *3*, 333–336.

[25] Goennenwein, S.; Tanaka, M.; Hu, B.; Moroder, L.; Sackmann, E. Functional incorporation of integrins into solid supported membranes on ultrathin films of cellulose: impact on adhesion. *Biophysical journal* **2003**, *85*, 646–655.

[26] Cuvelier, D.; Nassoy, P. Hidden dynamics of vesicle adhesion induced by specific stickers. *Physical Review Letters* **2004**, *93*, 228101.

[27] Steinkühler, J.; Agudo-Canalejo, J.; Lipowsky, R.; Dimova, R. Modulating vesicle adhesion by electric fields. *Biophysical journal* **2016**, *111*, 1454–1464.

[28] Young, T. III. An essay on the cohesion of fluids. *Philosophical transactions of the royal society of London* **1805**, 65–87.

[29] Lasky, L. A. A 'roll'in acute inflammation. *Current Biology* **1993**, *3*, 680–682.

[30] Sun, T.; Wang, G.; Feng, L.; Liu, B.; Ma, Y.; Jiang, L.; Zhu, D. Reversible switching between superhydrophilicity and superhydrophobicity. *Angewandte Chemie International Edition* **2004**, *43*, 357–360.

[31] Rehfeldt, F.; Steitz, R.; Armes, S. P.; von Klitzing, R.; Gast, A. P.; Tanaka, M. Reversible activation of diblock copolymer monolayers at the interface by pH modulation, 1: Lateral chain density and conformation. *The Journal of Physical Chemistry B* **2006**, *110*, 9171–9176.

[32] Kontturi, K.; Mafe, S.; Manzanares, J.; Svarfvar, B.; Viinikka, P. Modeling of the salt and pH effects on the permeability of grafted porous membranes. *Macromolecules* **1996**, *29*, 5740–5746.

[33] Brown, T. E.; Anseth, K. S. Spatiotemporal hydrogel biomaterials for regenerative medicine. *Chemical Society Reviews* **2017**, *46*, 6532–6552.

[34] Tanaka, M.; Nakahata, M.; Sumiya, A.; Ikemoto, Y.; Nakamura, T.; Dudin, A.; Schwieger, J.; Kaufmann, S.; Yamamoto, A.; Sakai, S. Hyperconfined Bio-Inspired Polymers in Integrative Flow-Through Systems for Highly Selective Removal of Heavy Metal Ions (Preprint). 2023; `https://doi.org/10.21203/rs.3.rs-3422705/v1f,note=`.

[35] Yamamoto, A.; Hayashi, K.; Sumiya, A.; Weissenfeld, F.; Hinatsu, S.; Abuillan, W.; Nakahata, M.; Tanaka, M. Modulation of viscoelasticity and interfacial potential of polyelectrolyte brush by Ion-specific interactions. *Frontiers in Soft Matter* **2022**, *2*, 959542.

[36] Körner, A.; Coroiu, A.; Copeland, L.; Gomez-Garibello, C.; Albani, C.; Zenger, M.; Brähler, E. The role of self-compassion in buffering symptoms of depression in the general population. *PloS one* **2015**, *10*, e0136598.

[37] Burk, A. S.; Monzel, C.; Yoshikawa, H. Y.; Wuchter, P.; Saffrich, R.; Eckstein, V.; Tanaka, M.; Ho, A. D. Quantifying adhesion mechanisms and dynamics of human hematopoietic stem and progenitor cells. *Scientific reports* **2015**, *5*, 9370.

[38] Bruinsma, R.; Sackmann, E. Bioadhesion and the dewetting transition. *Comptes Rendus de l'Académie des Sciences-Series IV-Physics-Astrophysics* **2001**, *2*, 803–815.

[39] Tillett, W. S.; Francis Jr, T. Serological reactions in pneumonia with a non-protein somatic fraction of pneumococcus. *The Journal of experimental medicine* **1930**, *52*, 561.

[40] Sproston, N. R.; Ashworth, J. J. Role of C-reactive protein at sites of inflammation and infection. *Frontiers in immunology* **2018**, *9*, 754.

[41] Thompson, D.; Pepys, M. B.; Wood, S. P. The physiological structure of human C-reactive protein and its complex with phosphocholine. *Structure* **1999**, *7*, 169–177.

[42] Chang, M.-K.; Binder, C. J.; Torzewski, M.; Witztum, J. L. C-reactive protein binds to both oxidized LDL and apoptotic cells through recognition of a common ligand: phosphorylcholine of oxidized phospholipids. *Proceedings of the National Academy of Sciences* **2002**, *99*, 13043–13048.

[43] Kushner, I.; Kaplan, M. H. Studies of acute phase protein: I. An Immunohisto- chemical method for the localization of cx-reactive protein in rabbits. Association with necrosis in local inflammatory lesions. *The Journal of experimental medicine* **1961**, *114*, 961–974.

[44] Makky, A.; Tanaka, M. Impact of lipid oxidization on biophysical properties of model cell membranes. *The Journal of Physical Chemistry B* **2015**, *119*, 5857–5863.

[45] Korytowski, A.; Abuillan, W.; Makky, A.; Konovalov, O.; Tanaka, M. Impact of lipid oxidization on vertical structures and electrostatics of phospholipid monolayers revealed by combination of specular X-ray reflectivity and grazing-incidence X- ray fluorescence. *The Journal of Physical Chemistry B* **2015**, *119*, 9787–9794.

[46] Korytowski, A. A. Influence of Lipid Oxidization on Structures and Functions of Biological Membranes. dissertation, Universität Heidelberg, 2016.

[47] Duwe, H. d.; Sackmann, E. Bending elasticity and thermal excitations of lipid bilayer vesicles: modulation by solutes. *Physica A: Statistical Mechanics and its Applications* **1990**, *163*, 410–428.

[48] Fröhlich, B.; Jäger, J.; Lansche, C.; Sanchez, C. P.; Cyrklaff, M.; Buchholz, B.; Soubeiga, S. T.; Simpore, J.; Ito, H.; Schwarz, U. S.; others Hemoglobin S and C affect biomechanical membrane properties of P. falciparum-infected erythrocytes. *Communications Biology* **2019**, *2*, 311.

[49] Matsuzaki, T.; Ito, H.; Chevyreva, V.; Makky, A.; Kaufmann, S.; Okano, K.; Kobayashi, N.; Suganuma, M.; Nakabayashi, S.; Yoshikawa, H. Y.; others Adsorption of galloyl catechin aggregates significantly modulates membrane mechanics in the absence of biochemical cues. *Physical Chemistry Chemical Physics* **2017**, *19*, 19937–19947.

[50] Gov, N.; Zilman, A.; Safran, S. Cytoskeleton confinement and tension of red blood cell membranes. *Physical review letters* **2003**, *90*, 228101.

[51] Weissenfeld, F.; Wesenberg, L.; Nakahata, M.; Müller, M.; Tanaka, M. Modulation of wetting of stimulus responsive polymer brushes by lipid vesicles: experiments and simulations. *Soft Matter* **2023**, *19*, 2491–2504.

[52] Helm, C. A.; Knoll, W.; Israelachvili, J. N. Measurement of ligand-receptor interactions. *Proceedings of the National Academy of Sciences* **1991**, *88*, 8169–8173.

[53] Angelova, M.; Dimitrov, D. S. A mechanism of liposome electroformation. *Trends in colloid and interface science II* **1988**, 59–67.

[54] Mathivet, L.; Cribier, S.; Devaux, P. F. Shape change and physical properties of giant phospholipid vesicles prepared in the presence of an AC electric field. *Biophysical journal* **1996**, *70*, 1112–1121.

[55] Thévenaz, P.; Blu, T.; Unser, M. Interpolation revisited [medical images application]. *IEEE Transactions on medical imaging* **2000**, *19*, 739–758.

[56] Reeves, J. P.; Dowben, R. M. Formation and properties of thin-walled phospholipid vesicles. *Journal of cellular physiology* **1969**, *73*, 49–60.

[57] Browicz, T. Further observation of motion phenomena on red blood cells in pathological states. *Zbl. med. Wissen* **1890**, *28*, 625–627.

[58] Auth, T.; Safran, S.; Gov, N. S. Fluctuations of coupled fluid and solid membranes with application to red blood cells. *Physical Review E* **2007**, *76*, 051910.

[59] Milner, S. T.; Safran, S. Dynamical fluctuations of droplet microemulsions and vesicles. *Physical Review A* **1987**, *36*, 4371.

[60] Betz, T.; Sykes, C. Time resolved membrane fluctuation spectroscopy. *Soft Matter* **2012**, *8*, 5317–5326.

[61] Evans, E. A. Bending elastic modulus of red blood cell membrane derived from buckling instability in micropipet aspiration tests. *Biophysical journal* **1983**, *43*, 27–30.

[62] Dao, M.; Lim, C.; Suresh, S. Mechanics of the human red blood cell deformed by optical tweezers [Journal of the Mechanics and Physics of Solids, 51 (2003) 2259-2280]. *Journal of the Mechanics and Physics of Solids* **2005**, *2*, 493–494.

[63] Butt, H.-J.; Wolff, E.; Gould, S.; Northern, B. D.; Peterson, C.; Hansma, P. Imaging cells with the atomic force microscope. *Journal of structural biology* **1990**, *105*, 54–61.

[64] Brochard, F.; Lennon, J. Frequency spectrum of the flicker phenomenon in erythrocytes. *Journal de Physique* **1975**, *36*, 1035–1047.

[65] Dimova, R.; Marques, C. *The giant vesicle book*; CRC Press, 2019.

[66] Gorb, E.; Gorb, S. Physicochemical properties of functional surfaces in pitchers of the carnivorous plant Nepenthes alata Blanco (Nepenthaceae). *Plant Biology* **2006**, 841–848.

[67] Kreder, M. J.; Daniel, D.; Tetreault, A.; Cao, Z.; Lemaire, B.; Timonen, J. V.; Aizenberg, J. Film dynamics and lubricant depletion by droplets moving on lubricated surfaces. *Physical Review X* **2018**, *8*, 031053.

[68] Ma, S.; Wu, Y.; Zhou, F. Bioinspired synthetic wet adhesives: from permanent bonding to reversible regulation. *Current Opinion in Colloid & Interface Science* **2020**, *47*, 84–98.

[69] Barthlott, W.; Neinbuis, C. Lotus-Effekt und Autolack: Die Selbstreinigungsfähigkeit mikrostrukturierter Oberflächen. *Biologie in unserer Zeit* **1998**, *28*, 314–321.

[70] Jenkins, J. T. Static equilibrium configurations of a model red blood cell. *Journal of mathematical biology* **1977**, *4*, 149–169.

[71] Ma, S.; Zhang, X.; Yu, B.; Zhou, F. Brushing up functional materials. *NPG Asia Materials* **2019**, *11*, 24.

[72] Santer, S.; Rühe, J. Motion of nano-objects on polymer brushes. *Polymer* **2004**, *45*, 8279–8297.

[73] Sundaram, H. S.; Ella-Menye, J.-R.; Brault, N. D.; Shao, Q.; Jiang, S. Reversibly switchable polymer with cationic/zwitterionic/anionic behavior through synergistic protonation and deprotonation. *Chemical Science* **2014**, *5*, 200–205.

[74] Hafner, D.; Ziegler, L.; Ichwan, M.; Zhang, T.; Schneider, M.; Schiffmann, M.; Thomas, C.; Hinrichs, K.; Jordan, R.; Amin, I. Mussel-inspired polymer carpets: Direct photografting of polymer brushes on polydopamine nanosheets for controlled cell adhesion. *Advanced Materials* **2016**, *28*, 1489–1494.

[75] Costerton, J. W.; Stewart, P. S.; Greenberg, E. P. Bacterial biofilms: a common cause of persistent infections. *science* **1999**, *284*, 1318–1322.

[76] Jones, R. A. *Soft condensed matter*; Oxford University Press, 2002; Vol. 6.

[77] Edwards, S.; Doi, M. Thetheory of polymer dynamics. 1986.

[78] Kuhn, W.; Grün, F. Beziehungen zwischen elastischen Konstanten und Dehnungsdoppelbrechung hochelastischer Stoffe. *Kolloid-Zeitschrift* **1942**, *101*, 248–271.

[79] Flory, P.-J. Statistical thermodynamics of semi-flexible chain molecules. *Proceedings of the Royal Society of London. Series A. Mathematical and Physical Sciences* **1956**, *234*, 60–73.

[80] Isaacson, J.; Lubensky, T. Flory exponents for generalized polymer problems. *Journal de Physique Lettres* **1980**, *41*, 469–471.

[81] Fixman, M. Radius of gyration of polymer chains. *The Journal of Chemical Physics* **1962**, *36*, 306–310.

[82] Fredrickson, G. H.; Frank, C. W. Interpretation of electronic energy transport experiments in polymeric systems. *Macromolecules* **1983**, *16*, 1198–1206.

[83] Backmann, N.; Kappeler, N.; Braun, T.; Huber, F.; Lang, H.-P.; Gerber, C.; Lim, R. Y. Sensing surface PEGylation with microcantilevers. *Beilstein journal of nanotechnology* **2010**, *1*, 3–13.

[84] Semwogerere, D.; Weeks, E. R. Confocal microscopy. *Encyclopedia of biomaterials and biomedical engineering* **2005**, *23*, 1–10.

[85] Elliott, A. D. Confocal microscopy: principles and modern practices. *Current protocols in cytometry* **2020**, *92*, e68.

[86] McNally, J. G.; Karpova, T.; Cooper, J.; Conchello, J. A. Three-dimensional imaging by deconvolution microscopy. *Methods* **1999**, *19*, 373–385.

[87] Cole, R. W.; Jinadasa, T.; Brown, C. M. Measuring and interpreting point spread functions to determine confocal microscope resolution and ensure quality control. *Nature protocols* **2011**, *6*, 1929–1941.

[88] Hirschman, I. I.; Widder, D. V. *The convolution transform*; Courier Corporation, 2012.

[89] Röntgen, W. C. Uber eine neue Art von Strahlen. *Annalen der Physik* **1898**, *300*, 1–11.

[90] Compton, A. H. A quantum theory of the scattering of X-rays by light elements. *Physical review* **1923**, *21*, 483.

[91] Daillant, J.; Gibaud, A. *X-ray and neutron reflectivity: principles and applications*; Springer, 2008; Vol. 770.

[92] Tolan, M.; Tolan, M. *X-ray scattering from soft-matter thin films: materials science and basic research*; Springer, 1999; Vol. 148.

[93] Toney, M. F.; Brennan, S. Observation of the effect of refraction on x rays diffracted in a grazing-incidence asymmetric Bragg geometry. *Physical Review B* **1989**, *39*, 7963.

[94] Schuppar, B. *Elementare numerische Mathematik: eine problemorientierte Einführung für Lehrer und Studierende*; Springer-Verlag, 2013.

[95] Dupertuis, M.; Proctor, M.; Acklin, B. Generalization of complex Snell–Descartes and Fresnel laws. *JOSA A* **1994**, *11*, 1159–1166.

[96] Parratt, L. G. Surface studies of solids by total reflection of X-rays. *Physical review* **1954**, *95*, 359.

[97] Als-Nielsen, J.; McMorrow, D. *Elements of modern X-ray physics*; John Wiley & Sons, 2011.

[98] Braslau, A.; Deutsch, M.; Pershan, P. S.; Weiss, A.; Als-Nielsen, J.; Bohr, J. Surface roughness of water measured by x-ray reflectivity. *Physical review letters* **1985**, *54*, 114.

[99] Nevot, L.; Croce, P. Caractérisation des surfaces par réflexion rasante de rayons X. Application à l'étude du polissage de quelques verres silicates. *Revue de Physique appliquée* **1980**, *15*, 761–779.

[100] Atkins, P. W.; De Paula, J. *Physical chemistry*; John Wiley & Sons, 2008.

[101] Blum, L. Structure of the electric double layer. *Advances in chemical physics* **1990**, *78*, 171–222.

[102] Ludwig Pohlmann Skript PC3 - Elektrochemie. 2005; `http://userpage.fu-berlin.de/~lap/PCIII_EC_4.pdf`, [Online; accessed 17-january-2024].

[103] von Helmholtz, H.; Hittorf, J. W.; Waals, J. D. *Physical Memoirs Selected and Translated from Foreign Sources*; Taylor & Francis, 1888; Vol. 1.

[104] Chapman, D. L. LI. A contribution to the theory of electrocapillarity. *The London, Edinburgh, and Dublin philosophical magazine and journal of science* **1913**, *25*, 475–481.

[105] Stern, O. Zur theorie der elektrolytischen doppelschicht. *Zeitschrift für Elektrochemie und angewandte physikalische Chemie* **1924**, *30*, 508–516.

[106] Henry, D. The cataphoresis of suspended particles. Part I.—The equation of cataphoresis. *Proceedings of the Royal Society of London. Series A, Containing Papers of a Mathematical and Physical Character* **1931**, *133*, 106–129.

[107] Bhattacharjee, S. DLS and zeta potential–what they are and what they are not? *Journal of controlled release* **2016**, *235*, 337–351.

[108] Zilker, A.; Engelhardt, H.; Sackmann, E. Dynamic reflection interference contrast (RIC-) microscopy: a new method to study surface excitations of cells and to measure membrane bending elastic moduli. *Journal De Physique* **1987**, *48*, 2139–2151.

[109] Rädler, J.; Sackmann, E. Imaging optical thicknesses and separation distances of phospholipid vesicles at solid surfaces. *Journal de Physique II* **1993**, *3*, 727–748.

[110] Elender, G.; Kühner, M.; Sackmann, E. Functionalisation of Si/SiO2 and glass surfaces with ultrathin dextran films and deposition of lipid bilayers. *Biosensors & bioelectronics* **1996**, *11*, 565–577.

[111] Tanaka, M.; Rehfeldt, F.; Schneider, M. F.; Mathe, G.; Albersdörfer, A.; Neumaier, K. R.; Purrucker, O.; Sackmann, E. Wetting and dewetting of extracellular matrix and glycocalix models. *Journal of Physics: Condensed Matter* **2005**, *17*, S649.

[112] Ploem, J. Reflection-contrast microscopy as a tool for investigation of the attachment of living cells to a glass surface. *Mononuclear phagocytes in immunity, infection and pathology* **1975**, 405–421.

[113] Limozin, L.; Sengupta, K. Quantitative reflection interference contrast micro-scopy (RICM) in soft matter and cell adhesion. *ChemPhysChem* **2009**, *10*, 2752–2768.

[114] Wiegand, G.; Neumaier, K. R.; Sackmann, E. Microinterferometry: three-dimensional reconstruction of surface microtopography for thin-film and wetting studies by reflection interference contrast microscopy (RICM). *Applied optics* **1998**, *37*, 6892–6905.

[115] Simson, R.; Albersdörfer, A.; Sackmann, E. Adhesion of soft biological shells controlled by bending elasticity and macromolecular networks. *MRS Online Pro-ceedings Library (OPL)* **1996**, *463*, 3.

[116] Albersdörfer, A.; Feder, T.; Sackmann, E. Adhesion-induced domain formation by interplay of long-range repulsion and short-range attraction force: a model membrane study. *Biophysical journal* **1997**, *73*, 245–257.

[117] Higaki, Y.; Fröhlich, B.; Yamamoto, A.; Murakami, R.; Kaneko, M.; Taka-hara, A.; Tanaka, M. Ion-specific modulation of interfacial interaction poten-tials between solid substrates and cell-sized particles mediated via zwitterionic, super-hydrophilic poly (sulfobetaine) brushes. *The Journal of Physical Chemistry B* **2017**, *121*, 1396–1404.

[118] Spatz, J. P.; Geiger, B. Molecular engineering of cellular environments: cell ad-hesion to nano-digital surfaces. *Methods in cell biology* **2007**, *83*, 89–111.

[119] Parsons, J. T.; Horwitz, A. R.; Schwartz, M. A. Cell adhesion: integrating cyto-skeletal dynamics and cellular tension. *Nature reviews Molecular cell biology* **2010**, *11*, 633–643.

[120] Shah, K.; Dubey, R. Effect of cadmium on RNA level as well as activity and mo-lecular forms of ribonuclease in growing rice seedlings. *PLANT PHYSIOLOGY AND BIOCHEMISTRY-PARIS-* **1995**, *33*, 577–577.

[121] Woolhouse, H. *Physiological plant ecology III: Responses to the chemical and biological environment*; Springer, 1983; pp 245–300.

[122] Grill, E.; Winnacker, E.-L.; Zenk, M. H. Phytochelatins, a class of heavy-metal-binding peptides from plants, are functionally analogous to metallothioneins. *Pro-ceedings of the National Academy of Sciences* **1987**, *84*, 439–443.

[123] Jalilehvand, F.; Amini, Z.; Parmar, K.; Kang, E. Y. Cadmium (II) N-acetylcysteine complex formation in aqueous solution. *Dalton Transactions* **2011**, *40*, 12771–12778.

[124] Hamer, D. H. Metallothionein. *Annual review of biochemistry* **1986**, *55*, 913–951.

[125] Cobbett, C. S. Phytochelatin biosynthesis and function in heavy-metal detoxification. *Current opinion in plant biology* **2000**, *3*, 211–216.

[126] Lipowsky, R.; Sackmann, E. *Structure and dynamics of membranes: I. from cells to vesicles/II. generic and specific interactions*; Elsevier, 1995.

[127] Miller, C. E.; Majewski, J.; Gog, T.; Kuhl, T. L. Characterization of biological thin films at the solid-liquid interface by X-ray reflectivity. *Physical review letters* **2005**, *94*, 238104.

[128] Generosi, J.; Castellano, C.; Pozzi, D.; Castellano, A. C.; Felici, R.; Natali, F.; Fragneto, G. X-ray and neutron reflectivity study of solid-supported lipid membranes prepared by spin coating. *Journal of applied physics* **2004**, *96*, 6839–6844.

[129] Nováková, E.; Giewekemeyer, K.; Salditt, T. Structure of two-component lipid membranes on solid support: An x-ray reflectivity study. *Physical Review E* **2006**, *74*, 051911.

[130] Wang, S.; Fukuto, M.; Yang, L. In situ x-ray reflectivity studies on the formation of substrate-supported phospholipid bilayers and monolayers. *Physical Review E* **2008**, *77*, 031909.

[131] Abuillan, W. Fine-Structures, Lateral Correlation and Diffusion of Membrane-Associated Proteins on Biological Membrane Surfaces. Ph.D. thesis, 2013.

[132] Burk, A. S. Quantifying Adhesion and Morphological Dynamics of Human Hematopoietic Stem and Progenitor Cells on Novel In Vitro Models of Bone Marrow Niche. dissertation, Universität Heidelberg, 2015.

[133] Hetzer, M.; Heinz, S.; Grage, S.; Bayerl, T. Asymmetric molecular friction in supported phospholipid bilayers revealed by NMR measurements of lipid diffusion. *Langmuir* **1998**, *14*, 982–984.

[134] Rosano, C.; Arosio, P.; Bolognesi, M. The X-ray three-dimensional structure of avidin. *Biomolecular Engineering* **1999**, *16*, 5–12.

[135] Abuillan, W.; Vorobiev, A.; Hartel, A.; Jones, N. G.; Engstler, M.; Tanaka, M. Quantitative determination of the lateral density and intermolecular correlation between proteins anchored on the membrane surfaces using grazing incidence small-angle X-ray scattering and grazing incidence X-ray fluorescence. *The Journal of chemical physics* **2012**, *137*.

[136] Nardi, J.; Bruinsma, R.; Sackmann, E. Adhesion-induced reorganization of charged fluid membranes. *Physical Review E* **1998**, *58*, 6340.

[137] Heskins, M.; Guillet, J. E. Solution properties of poly (N-isopropylacrylamide). *Journal of Macromolecular Science—Chemistry* **1968**, *2*, 1441–1455.

[138] Okahata, Y.; Noguchi, H.; Seki, T. Thermoselective permeation from a polymer-grafted capsule membrane. *Macromolecules* **1986**, *19*, 493–494.

[139] Guttenberg, Z.; Bausch, A.; Hu, B.; Bruinsma, R.; Moroder, L.; Sackmann, E. Measuring ligand- receptor unbinding forces with magnetic beads: molecular leverage. *Langmuir* **2000**, *16*, 8984–8993.

[140] Bruinsma, R. *Physics of Biomaterials: Fluctuations, Selfassembly and Evolution*; Springer, 1996; pp 61–101.

[141] Ivanov, A. E.; Eccles, J.; Panahi, H. A.; Kumar, A.; Kuzimenkova, M. V.; Nilsson, L.; Bergenståhl, B.; Long, N.; Phillips, G. J.; Mikhalovsky, S. V.; others Boronate-containing polymer brushes: Characterization, interaction with saccharides and mammalian cancer cells. *Journal of Biomedical Materials Research Part A: An Official Journal of The Society for Biomaterials, The Japanese Society for Biomaterials, and The Australian Society for Biomaterials and the Korean Society for Biomaterials* **2009**, *88*, 213–225.

[142] Tugulu, S.; Klok, H.-A. Stability and nonfouling properties of poly (poly (ethylene glycol) methacrylate) brushes under cell culture conditions. *Biomacromolecules* **2008**, *9*, 906–912.

[143] Leckband, D.; Sheth, S.; Halperin, A. Grafted poly (ethylene oxide) brushes as nonfouling surface coatings. *Journal of Biomaterials Science, Polymer Edition* **1999**, *10*, 1125–1147.

[144] Czajor, J.; Abuillan, W.; Nguyen, D. V.; Heidebrecht, C.; Mondarte, E. A.; Konovalov, O. V.; Hayashi, T.; Felder-Flesch, D.; Kaufmann, S.; Tanaka, M. Dendronized oligoethylene glycols with phosphonate tweezers for cell-repellent coating of oxide surfaces: coarse-scale and nanoscopic interfacial forces. *RSC advances* **2021**, *11*, 17727–17733.

[145] Ahrens, H.; Förster, S.; Helm, C. A. Charged polymer brushes: counterion incorporation and scaling relations. *Physical review letters* **1998**, *81*, 4172.

[146] DiTizio, V.; Ferguson, G. W.; Mittelman, M. W.; Khoury, A. E.; Bruce, A. W.; DiCosmo, F. A liposomal hydrogel for the prevention of bacterial adhesion to catheters. *Biomaterials* **1998**, *19*, 1877–1884.

[147] Thet, N.; Hong, S.; Marshall, S.; Laabei, M.; Toby, A.; Jenkins, A. Visible, colorimetric dissemination between pathogenic strains of Staphylococcus aureus and Pseudomonas aeruginosa using fluorescent dye containing lipid vesicles. *Biosensors and Bioelectronics* **2013**, *41*, 538–543.

[148] Wang, X.; Yan, F.; Liu, X.; Wang, P.; Shao, S.; Sun, Y.; Sheng, Z.; Liu, Q.; Lovell, J. F.; Zheng, H. Enhanced drug delivery using sonoactivatable liposomes with membrane-embedded porphyrins. *Journal of controlled release* **2018**, *286*, 358–368.

[149] Casas-Ferrer, L.; Brisson, A.; Massiera, G.; Casanellas, L. Design of vesicle prototissues as a model for cellular tissues. *Soft Matter* **2021**, *17*, 5061–5072.

[150] Oberholzer, T.; Luisi, P. The use of liposomes for constructing cell models. *Journal of Biological Physics* **2002**, *28*, 733–744.

[151] Hamada, T.; Yoshikawa, K. Cell-sized liposomes and droplets: Real-world modeling of living cells. *Materials* **2012**, *5*, 2292–2305.

[152] Boulbitch, A.; Guttenberg, Z.; Sackmann, E. Kinetics of membrane adhesion mediated by ligand–receptor interaction studied with a biomimetic system. *Biophysical Journal* **2001**, *81*, 2743–2751.

[153] Papahadjopoulos, D.; Allen, T.; Gabizon, A.; Mayhew, E.; Matthay, K.; Huang, S.; Lee, K.; Woodle, M.; Lasic, D.; Redemann, C. Sterically stabilized liposomes: improvements in pharmacokinetics and antitumor therapeutic efficacy. *Proceedings of the National Academy of Sciences* **1991**, *88*, 11460–11464.

[154] Tardi, P.; Boman, N.; Cullis, P. Liposomal doxorubicin. *Journal of drug targeting* **1996**, *4*, 129–140.

[155] Ngassam, V. N.; Su, W.-C.; Gettel, D. L.; Deng, Y.; Yang, Z.; Wang-Tomic, N.; Sharma, V. P.; Purushothaman, S.; Parikh, A. N. Recurrent dynamics of rupture transitions of giant lipid vesicles at solid surfaces. *Biophysical journal* **2021**, *120*, 586–597.

[156] Borghi, N.; Alias, K.; De Gennes, P.-G.; Brochard-Wyart, F. Wetting fibers with liposomes. *Journal of colloid and interface science* **2005**, *285*, 61–66.

[157] Murrell, M. P.; Voituriez, R.; Joanny, J.-F.; Nassoy, P.; Sykes, C.; Gardel, M. L. Liposome adhesion generates traction stress. *Nature Physics* **2014**, *10*, 163–169.

[158] Tian, D.; Song, Y.; Jiang, L. Patterning of controllable surface wettability for printing techniques. *Chemical society reviews* **2013**, *42*, 5184–5209.

[159] Dong, H.; Zheng, Y.; Wang, N.; Bai, H.; Wang, L.; Wu, J.; Zhao, Y.; Jiang, L. Highly efficient fog collection unit by integrating artificial spider silks. *Advanced Materials Interfaces* **2016**, *3*, 1500831.

[160] Wang, Q.; Yao, X.; Liu, H.; Quéré, D.; Jiang, L. Self-removal of condensed water on the legs of water striders. *Proceedings of the National Academy of Sciences* **2015**, *112*, 9247–9252.

[161] Bayer, I. S.; Megaridis, C. M. Contact angle dynamics in droplets impacting on flat surfaces with different wetting characteristics. *Journal of Fluid Mechanics* **2006**, *558*, 415–449.

[162] Puech, P.-H.; Askovic, V.; De Gennes, P.-G.; Brochard-Wyart, F. Dynamics of vesicle adhesion: spreading versus dewetting coupled to binder diffusion. *Biophysical Reviews and Letters* **2006**, *1*, 85–95.

[163] Pant, R.; Singha, S.; Bandyopadhyay, A.; Khare, K. Investigation of static and dynamic wetting transitions of UV responsive tunable wetting surfaces. *Applied Surface Science* **2014**, *292*, 777–781.

[164] He, B.; Lee, J. Dynamic wettability switching by surface roughness effect. The Sixteenth Annual International Conference on Micro Electro Mechanical Systems, 2003. MEMS-03 Kyoto. IEEE. 2003; pp 120–123.

[165] Davydovich, O.; Chu, E.; Friar, Z.; Smilgies, D.-M.; Moore, P.; Sidorenko, A. Co-ordinated Responsive Arrays of Surface-Linked Polymer Islands–CORALs. *ACS applied materials & interfaces* **2018**, *10*, 7459–7468.

[166] Hörning, M.; Nakahata, M.; Linke, P.; Yamamoto, A.; Veschgini, M.; Kaufmann, S.; Takashima, Y.; Harada, A.; Tanaka, M. Dynamic mechano-regulation of myoblast cells on supramolecular hydrogels cross-linked by reversible host-guest interactions. *Scientific Reports* **2017**, *7*, 7660.

[167] Fu, M.; Burkart, T.; Maryshev, I.; Franquelim, H. G.; Merino-Salomón, A.; Reverte-López, M.; Frey, E.; Schwille, P. Mechanochemical feedback loop drives persistent motion of liposomes. *Nature Physics* **2023**, 1–8.

[168] Bartelt, S. M.; Steinkühler, J.; Dimova, R.; Wegner, S. V. Light-guided motility of a minimal synthetic cell. *Nano Letters* **2018**, *18*, 7268–7274.

[169] Blake, D. A.; Chakrabarti, P.; Khosraviani, M.; Hatcher, F. M.; Westhoff, C. M.; Goebel, P.; Wylie, D. E.; Blake, R. C. Metal binding properties of a monoclonal antibody directed toward metal-chelate complexes. *Journal of Biological Chemistry* **1996**, *271*, 27677–27685.

[170] Frank, V.; Kaufmann, S.; Wright, R.; Horn, P.; Yoshikawa, H. Y.; Wuchter, P.; Madsen, J.; Lewis, A. L.; Armes, S. P.; Ho, A. D.; others Frequent mechanical stress suppresses proliferation of mesenchymal stem cells from human bone marrow without loss of multipotency. *Scientific reports* **2016**, *6*, 24264.

[171] Pierce, E.; Carmona, F.; Amirfazli, A. Understanding of sliding and contact angle results in tilted plate experiments. *Colloids and Surfaces A: Physicochemical and Engineering Aspects* **2008**, *323*, 73–82.

[172] Lam, C. N.; Wu, R.; Li, D.; Hair, M.; Neumann, A. Study of the advancing and receding contact angles: liquid sorption as a cause of contact angle hysteresis. *Advances in colloid and interface science* **2002**, *96*, 169–191.

[173] Pepys, M. B.; Hirschfield, G. M.; others C-reactive protein: a critical update. *The Journal of clinical investigation* **2003**, *111*, 1805–1812.

[174] Volanakis, J. E. Human C-reactive protein: expression, structure, and function. *Molecular immunology* **2001**, *38*, 189–197.

[175] Khandelia, H.; Mouritsen, O. G. Lipid gymnastics: evidence of complete acyl chain reversal in oxidized phospholipids from molecular simulations. *Biophysical journal* **2009**, *96*, 2734–2743.

[176] Wang, H.-W.; Wu, Y.; Chen, Y.; Sui, S.-F. Polymorphism of structural forms of C-reactive protein. *International journal of molecular medicine* **2002**, *9*, 665–671.

[177] Shrive, A. K.; Gheetham, G. M.; Holden, D.; Myles, D. A.; Turnell, W. G.; Volanakis, J. E.; Pepys, M. B.; Bloomer, A. C.; Greenhough, T. J. Three dimensional structure of human C-reactive protein. *Nature structural biology* **1996**, *3*, 346–354.

[178] Yin, H.; Xu, L.; Porter, N. A. Free radical lipid peroxidation: mechanisms and analysis. *Chemical reviews* **2011**, *111*, 5944–5972.

[179] Berliner, J. A.; Navab, M.; Fogelman, A. M.; Frank, J. S.; Demer, L. L.; Edwards, P. A.; Watson, A. D.; Lusis, A. J. Atherosclerosis: basic mechanisms: oxidation, inflammation, and genetics. *Circulation* **1995**, *91*, 2488–2496.

[180] Hammad, L. A.; Wu, G.; Saleh, M. M.; Klouckova, I.; Dobrolecki, L. E.; Hickey, R. J.; Schnaper, L.; Novotny, M. V.; Mechref, Y. Elevated levels of hydroxylated phosphocholine lipids in the blood serum of breast cancer patients. *Rapid Communications in Mass Spectrometry: An International Journal Devoted to the Rapid Dissemination of Up-to-the-Minute Research in Mass Spectrometry* **2009**, *23*, 863–876.

[181] Arora, R.; Vig, A.; Arora, S. Lipid peroxidation: a possible marker for diabetes. *J Diabetes Metab S* **2013**, *11*, 1–6.

[182] Montine, T. J.; Montine, K. S.; McMahan, W.; Markesbery, W. R.; Quinn, J. F.; Morrow, J. D. F2-isoprostanes in Alzheimer and other neurodegenerative diseases. *Antioxidants & Redox Signaling* **2005**, *7*, 269–275.

[183] Boveris, A.; Chance, B. The mitochondrial generation of hydrogen peroxide. General properties and effect of hyperbaric oxygen. *Biochemical Journal* **1973**, *134*, 707–716.

[184] Sinibaldi, F.; Howes, B. D.; Piro, M. C.; Polticelli, F.; Bombelli, C.; Ferri, T.; Coletta, M.; Smulevich, G.; Santucci, R. Extended cardiolipin anchorage to cytochrome c: a model for protein–mitochondrial membrane binding. *JBIC Journal of Biological Inorganic Chemistry* **2010**, *15*, 689–700.

[185] Megli, F. M.; Sabatini, K. Respiration state IV-generated ROS destroy the mitochondrial bilayer packing order in vitro. An EPR study. *FEBS letters* **2003**, *550*, 185–189.

[186] Spickett, C. M.; Reis, A.; Pitt, A. R. Identification of oxidized phospholipids by electrospray ionization mass spectrometry and LC–MS using a QQLIT instrument. *Free Radical Biology and Medicine* **2011**, *51*, 2133–2149.

[187] Chen, Y.; McMillan-Ward, E.; Kong, J.; Israels, S.; Gibson, S. Oxidative stress induces autophagic cell death independent of apoptosis in transformed and cancer cells. *Cell Death & Differentiation* **2008**, *15*, 171–182.

[188] Dalleau, S.; Baradat, M.; Guéraud, F.; Huc, L. Cell death and diseases related to oxidative stress: 4-hydroxynonenal (HNE) in the balance. *Cell Death & Differentiation* **2013**, *20*, 1615–1630.

[189] Fruhwirth, G. O.; Loidl, A.; Hermetter, A. Oxidized phospholipids: from molecular properties to disease. *Biochimica et Biophysica Acta (BBA)-Molecular Basis of Disease* **2007**, *1772*, 718–736.

[190] Borst, J. W.; Visser, N. V.; Kouptsova, O.; Visser, A. J. Oxidation of unsaturated phospholipids in membrane bilayer mixtures is accompanied by membrane fluidity changes. *Biochimica et Biophysica Acta (BBA)-Molecular and Cell Biology of Lipids* **2000**, *1487*, 61–73.

[191] Megli, F. M.; Russo, L.; Sabatini, K. Oxidized phospholipids induce phase separation in lipid vesicles. *FEBS letters* **2005**, *579*, 4577–4584.

[192] Sabatini, K.; Mattila, J.-P.; Megli, F. M.; Kinnunen, P. K. Characterization of two oxidatively modified phospholipids in mixed monolayers with DPPC. *Biophysical journal* **2006**, *90*, 4488–4499.

[193] Beranova, L.; Cwiklik, L.; Jurkiewicz, P.; Hof, M.; Jungwirth, P. Oxidation changes physical properties of phospholipid bilayers: fluorescence spectroscopy and molecular simulations. *Langmuir* **2010**, *26*, 6140–6144.

[194] Lu, R.; Zhao, X.; Li, J.; Niu, P.; Yang, B.; Wu, H.; Wang, W.; Song, H.; Huang, B.; Zhu, N.; others Genomic characterisation and epidemiology of 2019 novel coronavirus: implications for virus origins and receptor binding. *The lancet* **2020**, *395*, 565–574.

[195] Chan, J. F.-W.; Yuan, S.; Kok, K.-H.; To, K. K.-W.; Chu, H.; Yang, J.; Xing, F.; Liu, J.; Yip, C. C.-Y.; Poon, R. W.-S.; others A familial cluster of pneumonia associated with the 2019 novel coronavirus indicating person-to-person transmission: a study of a family cluster. *The lancet* **2020**, *395*, 514–523.

[196] Scudellari, M. How the coronavirus infects cells—and why Delta is so dangerous. 2021.

[197] Shang, J.; Ye, G.; Shi, K.; Wan, Y.; Luo, C.; Aihara, H.; Geng, Q.; Auerbach, A.; Li, F. Structural basis of receptor recognition by SARS-CoV-2. *Nature* **2020**, *581*, 221–224.

[198] Sztain, T.; Ahn, S.-H.; Bogetti, A. T.; Casalino, L.; Goldsmith, J. A.; Seitz, E.; McCool, R. S.; Kearns, F. L.; Acosta-Reyes, F.; Maji, S.; others A glycan gate controls opening of the SARS-CoV-2 spike protein. *Nature chemistry* **2021**, *13*, 963–968.

[199] Hoffmann, M.; Kleine-Weber, H.; Schroeder, S.; Krüger, N.; Herrler, T.; Erichsen, S.; Schiergens, T. S.; Herrler, G.; Wu, N.-H.; Nitsche, A.; others SARS-CoV-2 cell entry depends on ACE2 and TMPRSS2 and is blocked by a clinically proven protease inhibitor. *cell* **2020**, *181*, 271–280.

[200] Peacock, T. P.; Goldhill, D. H.; Zhou, J.; Baillon, L.; Frise, R.; Swann, O. C.; Kugathasan, R.; Penn, R.; Brown, J. C.; Sanchez-David, R. Y.; others The furin cleavage site in the SARS-CoV-2 spike protein is required for transmission in ferrets. *Nature microbiology* **2021**, *6*, 899–909.

[201] Armstrong, J.; Froelich, E. Inactivation of viruses by benzalkonium chloride. *Applied Microbiology* **1964**, *12*, 132–137.

[202] Su, X.; D'Souza, D. H. Inactivation of human norovirus surrogates by benzalkonium chloride, potassium peroxymonosulfate, tannic acid, and gallic acid. *Foodborne Pathogens and Disease* **2012**, *9*, 829–834.

[203] Schneck, E.; Schubert, T.; Konovalov, O. V.; Quinn, B. E.; Gutsmann, T.; Brandenburg, K.; Oliveira, R. G.; Pink, D. A.; Tanaka, M. Quantitative determination of ion distributions in bacterial lipopolysaccharide membranes by grazing-incidence X-ray fluorescence. *Proceedings of the National Academy of Sciences* **2010**, *107*, 9147–9151.

[204] Abuillan, W.; Schneck, E.; Körner, A.; Brandenburg, K.; Gutsmann, T.; Gill, T.; Vorobiev, A.; Konovalov, O.; Tanaka, M. Physical interactions of fish protamine and antisepsis peptide drugs with bacterial membranes revealed by combination of specular x-ray reflectivity and grazing-incidence x-ray fluorescence. *Physical Review E* **2013**, *88*, 012705.

[205] Schneck, E.; Schubert, T.; Konovalov, O. V.; Quinn, B. E.; Gutsmann, T.; Brandenburg, K.; Oliveira, R. G.; Pink, D. A.; Tanaka, M. Quantitative determination of ion distributions in bacterial lipopolysaccharide membranes by grazing-incidence X-ray fluorescence. *Proceedings of the National Academy of Sciences* **2010**, *107*, 9147–9151.

[206] Abuillan, W.; Schneck, E.; Körner, A.; Brandenburg, K.; Gutsmann, T.; Gill, T.; Vorobiev, A.; Konovalov, O.; Tanaka, M. Physical interactions of fish protamine and antisepsis peptide drugs with bacterial membranes revealed by combination of specular x-ray reflectivity and grazing-incidence x-ray fluorescence. *Physical Review E* **2013**, *88*, 012705.

[207] Körner, A.; Abuillan, W.; Deichmann, C.; Rossetti, F. F.; Köhler, A.; Konovalov, O. V.; Wedlich, D.; Tanaka, M. Quantitative determination of lateral concentration and depth profile of histidine-tagged recombinant proteins probed by grazing incidence X-ray fluorescence. *The Journal of Physical Chemistry B* **2013**, *117*, 5002–5008.

[208] Bohr, N. I. On the constitution of atoms and molecules. *The London, Edinburgh, and Dublin Philosophical Magazine and Journal of Science* **1913**, *26*, 1–25.

[209] Barkla, C. G. XXXIX. The spectra of the fluorescent Röntgen radiations. *The London, Edinburgh, and Dublin Philosophical Magazine and Journal of Science* **1911**, *22*, 396–412.

[210] Becker, R.; Golovchenko, J. A.; Patel, J. X-ray evanescent-wave absorption and emission. *Physical review letters* **1983**, *50*, 153.

[211] Jopson, R.; Mark, H.; Swift, C. Production of characteristic X rays by low-energy protons. *Physical review* **1962**, *127*, 1612.

[212] Vineyard, G. H. Grazing-incidence diffraction and the distorted-wave approximation for the study of surfaces. *Physical Review B* **1982**, *26*, 4146.

[213] Foglia, F.; Rogers, S.; Webster, J.; Akeroyd, F.; Gascoyne, K.; Lawrence, M.; Barlow, D. Neutron scattering studies of the effects of formulating amphotericin B with cholesteryl sulfate on the drug's interactions with phospholipid and phospholipid–sterol membranes. *Langmuir* **2015**, *31*, 8042–8051.

[214] Thoma, J.; Abuillan, W.; Furikado, I.; Habe, T.; Yamamoto, A.; Gierlich, S.; Kaufmann, S.; Brandenburg, K.; Gutsmann, T.; Konovalov, O.; others Specific localisation of ions in bacterial membranes unravels physical mechanism of effective bacteria killing by sanitiser. *Scientific Reports* **2020**, *10*, 12302.

[215] Älgå, A.; Eriksson, O.; Nordberg, M. Analysis of scientific publications during the early phase of the COVID-19 pandemic: topic modeling study. *Journal of medical Internet research* **2020**, *22*, e21559.

[216] Wimalawansa, S. J. Global epidemic of coronavirus—Covid-19: what can we do to minimize risks. *Eur J Biomed* **2020**, *7*, 432–8.

[217] Bondurant, S. W.; Duley, C. M.; Harbell, J. W. Demonstrating the persistent antibacterial efficacy of a hand sanitizer containing benzalkonium chloride on human skin at 1, 2, and 4 hours after application. *American journal of infection control* **2019**, *47*, 928–932.

[218] Hirose, R.; Bandou, R.; Ikegaya, H.; Watanabe, N.; Yoshida, T.; Daidoji, T.; Naito, Y.; Itoh, Y.; Nakaya, T. Disinfectant effectiveness against SARS-CoV-2 and influenza viruses present on human skin: model-based evaluation. *Clinical Microbiology and Infection* **2021**, *27*, 1042–e1.

[219] Winterhalter, M.; Bürner, H.; Marzinka, S.; Benz, R.; Kasianowicz, J. . Interaction of poly (ethylene-glycols) with air-water interfaces and lipid monolayers: investigations on surface pressure and surface potential. *Biophysical journal* **1995**, *69*, 1372–1381.

[220] Diel, E. E.; Lichtman, J. W.; Richardson, D. S. Tutorial: avoiding and correcting sample-induced spherical aberration artifacts in 3D fluorescence microscopy. *Nature protocols* **2020**, *15*, 2773–2784.

NATURWISSENSCHAFTLICH-MATHEMATISCHE
GESAMTFAKULTÄT

COMBINED FACULTY OF NATURAL SCIENCES AND
MATHEMATICS

RUPRECHT-KARLS-
UNIVERSITÄT
HEIDELBERG

Eidesstattliche Versicherung gemäß § 8 der Promotionsordnung für die Naturwissenschaftlich-Mathematische Gesamtfakultät der Universität Heidelberg / Sworn Affidavit according to § 8 of the doctoral degree regulations of the Combined Faculty of Natural Sciences and Mathematics

1. Bei der eingereichten Dissertation zu dem Thema / The thesis I have submitted entitled

   Modulation of Wetting and Mechanical Properties of Model Cell Membranes Caused by Changes on Molecular Levels

   handelt es sich um meine eigenständig erbrachte Leistung / is my own work.

2. Ich habe nur die angegebenen Quellen und Hilfsmittel benutzt und mich keiner unzulässigen Hilfe Dritter bedient. Insbesondere habe ich wörtlich oder sinngemäß aus anderen Werken übernommene Inhalte als solche kenntlich gemacht. / I have only used the sources indicated and have not made unauthorised use of services of a third party. Where the work of others has been quoted or reproduced, the source is always given.

3. Die Arbeit oder Teile davon habe ich wie folgt/bislang nicht[1] an einer Hochschule des In- oder Auslands als Bestandteil einer Prüfungs- oder Qualifikationsleistung vorgelegt. / I have not yet/have already[1] presented this thesis or parts thereof to a university as part of an examination or degree.

   Titel der Arbeit / Title of the thesis: ⸺⸺⸺⸺⸺⸺

   Hochschule und Jahr / University and year: ⸺⸺⸺⸺⸺⸺

   Art der Prüfungs- oder Qualifikationsleistung / Type of examination or degree: ⸺⸺⸺

4. Die Richtigkeit der vorstehenden Erklärungen bestätige ich. / I confirm that the declarations made above are correct.

5. Die Bedeutung der eidesstattlichen Versicherung und die strafrechtlichen Folgen einer unrichtigen oder unvollständigen eidesstattlichen Versicherung sind mir bekannt. / I am aware of the importance of a sworn affidavit and the criminal prosecution in case of a false or incomplete affidavit

Ich versichere an Eides statt, dass ich nach bestem Wissen die reine Wahrheit erklärt und nichts verschwiegen habe. / I affirm that the above is the absolute truth to the best of my knowledge and that I have not concealed anything.

Heidelberg, den 22.03.2024
Ort und Datum / Place and date

....
Unterschrift / Signature

[1] Nicht Zutreffendes streichen. Bei Bejahung sind anzugeben: der Titel der andernorts vorgelegten Arbeit, die Hochschule, das Jahr der Vorlage und die Art der Prüfungs- oder Qualifikationsleistung. / Please cross out what is not applicable. If applicable, please provide: the title of the thesis that was presented elsewhere, the name of the university, the year of presentation and the type of examination or degree.

The German text is legally binding.